

Ph.D. Thesis

**Template Assisted Fabrication of 1-D Nanostructures of
Nickel, Cobalt, Iron Oxide and Carbon nanotubes and a
Study on Their Structural, Magnetic and Nonlinear
Optical Properties for Applications**

**To be submitted in partial fulfilment of the requirements
for the award of the degree of**

Doctor of Philosophy

T. N. Narayanan

**Department of Physics
Cochin University of Science & Technology
Cochin - 682 022
India**

December 2009

Author:

T. N. Narayanan

Magnetics Laboratory
Department of Physics
Cochin University of Science and Technology
Kochi-682 022
Kerala, India.

E-Mail: tn_narayanan@yahoo.com

Residence:

Tharangattu mana
Punchapadam
Palakkad-678 634
Kerala-India.

Supervising Guide:

Prof. (Dr.) M. R. Anantharaman

Head of the Department
Department of Physics
Cochin University of Science and Technology
Kochi-682 022
Kerala, India.

Cover Page:

Front: FESEM image (lateral view) of MWCNTs.

Back: FESEM image of hybrid multiferroic nanostructure.

December 2009.

Declaration

I hereby declare that the present work in this thesis entitled **“Template assisted fabrication of 1-D nanostructures of Nickel, Cobalt, Iron Oxide and Carbon nanotubes and a study on their structural, magnetic and nonlinear optical properties for applications”** is based on the original research work carried out by me under the guidance and supervision of Prof. M. R. Anantharaman, Professor and Head, Department of Physics, Cochin University of Science and Technology, Cochin – 22, Kerala, India and has never been included in any other thesis submitted previously for the award of any degree.

Cochin -22

14-12-2009


T. N. Narayanan



Prof. M. R. Anantharaman
Professor & Head
Department of Physics
Cochin University of Science and
Technology
Cochin – 682 022 India

Certificate

Certified that the present work in this thesis entitled “**Template assisted fabrication of 1-D nanostructures of Nickel, Cobalt, Iron Oxide and Carbon nanotubes and a study on their structural, magnetic and nonlinear optical properties for applications**” is based on the bonafide research work carried out by **Mr. T. N. Narayanan** under my guidance at the Department of Physics, Cochin University of Science and Technology, Cochin – 22, Kerala, India and has not been included in any other thesis submitted previously for the award of any degree.

Cochin -22
14-12-2009

Prof. M. R. Anantharaman
(Supervising Guide)

Ph.No: +91484-2577404 Extn. 30 (Off)
E mail: mra@cusat.ac.in mraiyaer@yahoo.com

Acknowledgements

At an age when most young men have entered in to the world to make their future, I struggled with mathematics, science and mysterious of the natural world. Those were difficult days, but days that I look back upon with fond memories. There are many people, too many to mention in these few paragraphs, who helped me to get this point. I use this occasion to thank and remember all of my school and college teachers for molding me in this shape.

I am obliged to Prof. Anantharaman, my research guide and teacher for his valuable helps, advices, constant encouragements and support whole during my work. I thankfully acknowledge the immense support received from him and his family whole during my research work.

I am indebted to Prof. Pulickel M. Ajayan, Benjamin M. and Mary Greenwood Anderson Professor of Engineering, Rice University, Texas, USA for his valuable support and giving me a chance to carry out a major part of my Ph D with him at Rensselaer Polytechnic Institute, New York, USA.

I gratefully acknowledge the helps received from the former heads of the department, department of Physics, CUSAT. I am thankful to all of my teachers at the department of Physics for their valuable advices and caring. I also wish to thank Prof. Jacob Philip, Director, STIC, CUSAT (my doctoral committee member) for his valuable helps.

I express my sincere gratitude to Prof. Reji Philip, Raman Research Institute, Bangalore for his timely helps and allowing me to carry out nonlinear optical studies with his group. I also wish to remember the valuable scientific advices received from Dr. P A Joy and Dr. Vijayamohan K. Pillai at National Chemical Laboratory, Pune during my research work and also wish to thank them for allowing me to conduct some experiments with them.

I use this occasion to thank Prof. Manfred Albrecht, Dr. Denys Makarov and Dr. Ildico Guhr, University of Chemnitz, Germany for their helps for magnetisation measurement.

I may not able to complete this thesis if the following persons are not there to support me during various stages of my research. I thankfully remember their names at this occasion- Dr. M. M. Shaijumon (Shaijueetan), University of Paul Sabatier, Toulouse, France (formerly at Rice University, TX, USA), Mr. C. S. Suchand Sandeep, RRI, Bangalore, Dr. Lijie Ci, Rice University, USA., Dr. Victor Pushparaj, Rensselaer Polytechnic Institute, Troy, New York, Dr. Mahima, NCL, Pune, Dr. Sakthi Kumar, Toyo University, Japan and Dr. Salim Al-Harhi, Sultan Quaboos University, Oman, Muscat.

I am thankful to all ex- and present nonteaching and technical staffs of the department of Physics and administrative staffs at the Cochin University for their valuable support.

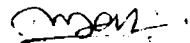
During the Ph. D studies I was supported by Kerala State Council for Science, Technology and Environment, Kerala through KSCSTE-05 research fellowship (2005-2009) and Council of Scientific and Industrial Research (CSIR) through CSIR-SRF (2009). I thankfully acknowledge their financial support rendered during my research work. I am grateful to the Interconnect Focus Centre, Rensselaer Polytechnic Institute, Troy, New York, USA for their financial support which enabled me to conduct a part of my work at Rensselaer Polytechnic Institute with Prof. Ajayan.

I may not be able to complete the present work if the following persons, my friends, are not there to mentally support me from all sides. The valuable advices of Miss Reena Mary (Reena Cheechi) and Mrs. Veena Gopalan (Veena Cheechi) guided me whole during my research work and will follow me in the rest of my life. I wish to express my gratitude to them and to their family during this occasion. I also wish to acknowledge the support I received from my dear friends Miss Vijutha Sunny, Miss Geetha Pookat, Mr. Vasudevan Namboodiri (Babu Sir), Mr. Rankumar, Mr. Senoy Thomas, Dr. Sajeev U S, Dr. Swapna S Nair, Mr. Sanoj M A, Dr. Mohammed Abdul Jamal, Mr. Sagar S, Mr. Hysen Thomas, Mr. Tom Thomas, Dr. Malini Jayaram, Dr. Asha, Mr. Syam Kishore, Mr. Kannan, Miss Meera V., Miss Soumya Jose, Miss Vinayasree, Mr. Sreeraj, Mr. Shinoj, Miss Saritha, Mr. Jaleel, Miss Nimisha, Miss Anjali, Mr. Anas and all ex-members of magnetics lab. I thank all of my friends at CUSAT, Victoria college and PUNCHAPADAM for their immense support and caring.

I am thankful to Dr. Saji K. J., who was my roommate and friend for last six years, for his helps and support. I am thankful to my classmates Mr. Loji, Mr. Aneesh, Mr. Vivek, Mr. Sasankan, Mr. Arun, Mr. Sandeep, Mr. Sujith Raman, Mrs. Prijitha, Mrs. Vincetha, and Miss Sona.

My family, they were always there with me at each stage of my research work, to support and encourage. I use this occasion to express my gratitude towards my parents, sister and family, Grandparents and my other beloved relatives and dedicating this thesis to my parents.

“ഈതരലാകൃസ്ഥാൻ സമസ്താൻ സകലപരിവ്രതാൻ സർവഭൂത്തേത്യ നമോമി”



T. N. Narayanan

Preface

Nanotechnology is all poised to become the technology of the future and is bound have a profound influence on other interdisciplinary fields of science, which will eventually lead to several applications. It is thus destined to play a seminal role in the day to day life of human beings and will usher in brand new derivatives of this technology. It is already proven that nanoscience and nanotechnology can find answers for many unanswered questions in atomic and molecular physics and can solve many of the problems that the humanity is going to face in the near future. It is envisaged that the influence of nanoscience is going to be substantial and the development in nanoscience will have a profound bearing on new interdisciplinary sciences involving MaterialsScience/Physics/Chemistry/Biotechnology/ChemicalEngineering/Mechanical Engineering. The epoch making statement of Sir Richard P. Feynman made in the late 50s' that 'there is plenty of room in to the bottom' has been vindicated and now scientists and engineers are delving at the 'bottom' for understanding the various phenomena attributed to the properties of the materials at the nanodimensions and also for finding newer applications based on nanotechnology.

The fact that materials properties can be engineered by altering the size, shape and dimension, while keeping the chemical composition intact has entirely transformed the mindset of the materials scientists. Materials when their particle size or grain size is reduced below a certain value are found to be exhibiting superlative chemical as well as physical properties. The prefix "Nano" indicates 10^{-9} and so nanoscience and technology deal with the materials having at least one of their dimensions in nanometers. The de Broglie wavelength of electron is also of the order of nanometers and so these dimensions influence the confinement of electron, which will in turn

determine their various properties. Thus their physical and chemical properties are dictated by the properties of electrons and electron bindings. There are many ways to classify systems according to their reduced dimensionalities, and one such classification is based on the transport properties of the electrons/phonons. A system is said to be in a reduced dimensionality if the intrinsic mean free path (λ_{int}) of electron is greater than the size of the materials ($L_{x,y,z}$). Hence, according to their dimensionality, nanostructures are classified as one dimensional (1-D) if $L_{x,y} < \lambda_{\text{int}}$, two dimensional (2-D) if $L_x < \lambda_{\text{int}}$ and zero dimensional (0-D) if $L_{x,y,z} < \lambda_{\text{int}}$.

Nanostructured materials by virtue of their distinctive physical properties can find tremendous application in realizing various devices. Different kinds of nanosized systems such as nanowires, nanotubes, nano dots and nano wells are devised based on their dimensionality. These engineered structures are identified as ideal templates for technology developments in fields like energy storage, data storage, energy transfer and medical diagnosis. Moreover, manipulation and control of matter at nano and atomic level are crucial for the development of different micro-sized and flexible devices like sensors, actuators and energy storage devices.

Magnetic nanostructures became the cynosure of all eyes with the discovery of exciting phenomena like Giant Magneto Resistance (GMR), Tunneling Magneto Resistance (TMR), Colossal Magneto Resistance (CMR), Magneto Caloric Effect (MCE) and Spin Polarized Tunneling. Studies on ultrafine magnetic multilayers were started in the 1970s, immediately after the invention of sophisticated thin film fabrication techniques like Molecular Beam Epitaxy and Atomic Layer Deposition. These studies later paved the way to a new and upcoming branch, Spintronics. It is envisaged that magnetic nanostructures are likely to replace today's unstructured magnetic media in the future. Structured magnetic

materials have an additional advantage in tuning the magnetic properties namely magnetic anisotropy and coercivity and hence data storage manipulation. Another growing demand is for novel, low dimensional, high conductance and low power electrical interconnects for future ultra high performance networking chips.

In the class of structured magnetic materials two dimensionally confined or quasi one dimensional objects like nanowire, tubes and rods have an important role. Nano hole and rod arrays with uniformity in shape and size have attracted growing attention due to their potential applications in various types of functional nano devices. Besides nanoelectronics, their applications extend to catalysis, energy storage devices, high density storage disks, medical diagnosis, therapy and drug delivery as well. Many of these proposed applications require membranes to be consisting of monodispersed aligned nanostructures.

Among various strategies for synthesizing nanoscopic materials reported in the literature, being a versatile and inexpensive technique, template assisted synthesis has attracted the attention of scientists. In this class, template assisted electrodeposition is a unique technique for the synthesis of well controlled nanostructures of both metal and metal oxides. The size, shape and structural properties of electrodeposited nano objects are controlled by the template chosen and a number of electrodeposition parameters. These electrodeposited multi layered magnetic nanowires have become a subject of intensive study, largely because they make it possible to measure the magnetoresistance of multilayers when the electric current is perpendicular to the layer interfaces.

Magnetic properties are usually dictated by size, dimension, shape, structure, morphology of the constituent phases, along with the type and strength of magnetic coupling between them. Fundamentally, the surface effects associated with the magnetic nanoparticles often show complicated

properties; especially under the interaction with surrounding particles. Structured magnetic materials provide a unique model system for the fundamental investigations on magnetism associated with the surface spin states of nanoparticles along with the shape anisotropy from the 1D structures. There is rich physics in this regime and investigations from a theoretical point of view will unravel the mysterious surrounding magnetism at the surfaces.

Nanofabrication offers the technical ability to fabricate magnetic objects with nanometric scale precision having unique magnetic properties, which may be tailored by manipulating the size, the shape, or the composition of nanostructures. Many of these properties come about by imposing a geometrical restriction on magnetization. As the size of the nanomagnet becomes comparable to key magnetic length scales such as exchange length (in the nanometer range) or domain wall width (nm- μm range), the magnetization configuration may be strongly affected. The finite lateral size may affect the magnetic behavior of nanostructures and is of primary importance from practical and theoretical points of view. The necessary criteria to achieve ultra high density in magnetic storage is that the lateral size of the information bits should be as small as possible, keeping the bit volume above the superparamagnetic limit, beyond which the energy needed to switch the magnetization of a bit becomes less than thermal energy. The transition region between two neighbouring bits should be as narrow as possible, which is difficult to achieve in continuous thin film media by the finite width of domain walls. A promising way to achieve small lateral size with comparatively large volume and hence high magnetic anisotropy of the bits is to realize arrays of nanometric magnetic pillars with strong shape anisotropy. This removes the limitations listed before as each bit then consisting of a single domain element, not experiencing exchange interactions with neighbors however close they are, and having two well

defined magnetization states of equal magnitude and opposite direction determined by the strong shape anisotropy of the element. Crystalline anisotropy will either compete with or collaborate with the shape anisotropy depending on the diameter of nanowires and tubes. These fundamental properties can be fine tuned by different templates of varying dimensions. One can synthesize not only metallic nanowires but also their alloys. Thin metallic interconnects with favorable properties is a bottleneck for ultra large scale integrated circuits and the fabrication of suitable metallic wires is a milestone towards its realisation.

Understanding the growth mechanism plays an important role in designing and fabricating various nanostructures. A general growth mechanism for the growth of 1-D nanostructures during template assisted electrodeposition is seldom seen in the literature. The lack of proper understanding of the growth mechanism impedes the further use of this technique for the synthesis of various multisegmented nanostructures for applications. In order to put forward a generalized growth mechanism, different precursors are needed to be tested with different templates under identical physical conditions.

Carbon nanotubes belong to one among the most extensively investigated materials in today's materials science research. The promising physico-mechanical properties make them unique for many applications. Composite materials of carbon nanotubes are ingenious materials due to their high performance and multiple functionalities. Different methodologies have been adopted by different research groups towards the realization of carbon nanotube based composite materials. Decorating the carbon nanotubes with other nanoparticles and filling of carbon nanotube are the two important methods among them. Though the filling of carbon nanotubes was widely accepted right from the beginning of the carbon nanotube research, successful and complete filling of carbon nanotubes is not yet attained.

Absence of any type of magnetic ordering in carbon nanotubes hinders them from magnetic applications. This motivated the scientists to make hybrid materials of carbon nanotubes with magnetic materials. Moreover, these types of hybrid materials have tremendous applications in various fields such as energy storage, radar absorbers, various sensors, NEMS, bio-medicine and catalysis. An exhaustive literature survey reveals that studies on these multisegmented carbon nanotube structures with magnetic materials are not very abundant. The confined existence of magnetic materials inside carbon nanotubes can exhibit unusual magnetic properties which are not seen in bare magnetic nanostructures or in their bulk material. The passivation of magnetic materials with carbon nanotubes further makes these hybrid materials very unique with long stability as they are protected from the near surroundings.

The field of nonlinear optics is another area which flourished with the advent of nanoscience and nanotechnology. Design and fabrication of photonic devices demands the availability of versatile nonlinear optical materials. Nonlinear optical properties of various nanostructures and materials were studied during the recent past. A detailed literature survey reveals that not many efforts have gone in to the studies of nonlinear optical properties of magnetic nanostructures. Nanostructures having multiple functionalities are sought after for future technological revolution and magnetic nanostructures with optical activities can find tremendous application in various optoelectronic devices, sensors and biological imaging and detection. Though carbon nanotubes are benchmarked for their nonlinear optical properties, their heterostructures with other metals are not much explored. Studies on these hybrid structures will help to understand more about the different mechanisms associated with nonlinear optics with equal importance to their applications.

So it is imperative that such magnetic nanostructures with multifunctional properties are synthesized using novel template assisted technique. Elucidation of mechanism of growth will help in tailoring the properties of such multifunctional hybrid nanostructures. This will provide a platform for studying the magnetism at the nanolevel. So the specific objectives of the present thesis are;

- ✚ Synthesis of magnetic nanowires and nanotubes of Ni and Co using various precursors using template assisted potentiostatic electrodeposition.
- ✚ Studies on the structural, morphological and magnetic properties of these nanowires and nanotubes.
- ✚ Formulation of a general growth mechanism for 1-D nanostructures during potentiostatic electrodeposition.
- ✚ Fabrication of hybrid 1-D structures of Ni and Co and verify the generalised growth mechanism.
- ✚ Synthesis of MWCNTs using template assisted Chemical Vapour Deposition and studies on their structure and morphology.
- ✚ Fabrication of carbon nanotube based magnetic heterostructures of Ni and Co using potentiostatic electrodeposition and their structural and magnetic characterisations.
- ✚ Evaluation of microwave absorbing properties of metal filled multiwall carbon nanotubes.
- ✚ Synthesis of MWCNT-superparamagnetic Iron Oxide composites using ferrofluids using nanocapillarity.

- ✦ Evaluation of nonlinear optical properties of nanowires and nanotubes of Ni and Co and their hybrid structures with MWCNTs.
- ✦ Synthesis of acicular Iron Oxide nanoparticles using complexing media and studies on their structural, magnetic and optical properties.
- ✦ Correlation of results.

This proposed thesis is entitled as “**Template assisted fabrication of 1-D nanostructures of Nickel, Cobalt, Iron Oxide and Carbon nanotubes and a study on their structural, magnetic and nonlinear optical properties for applications**” and is divided in to seven chapters.

Chapter 1 is the Introduction to the world of nanostructured materials with a brief peep in to the physics at nanodimensions. An overview of 1-D nanostructures and carbon nanotubes are provided here in a nutshell. Various methods for the synthesis of 1-D magnetic nanostructures are also dealt with in this chapter with special reference to their potential applications in various fields. Finally the motivation and the objectives of the work are outlined.

Chapter 2 discusses the various fabrication methods adopted for the synthesis of nanowires and nanotubes and the various analytical tools employed for their analysis. The principle behind these state of the art analytical tools is also briefly discussed in this chapter.

Details of template assisted synthesis of magnetic nanowires and nanotubes of Ni and Co are provided in **Chapter 3**. A growth mechanism has been proposed for the fabrication of these nanowires and nanotubes during potentiostatic electrodeposition. Finally, the design and fabrication of

a novel multisegmented magnetic nanostructure called Ni @ Co nanorods is discussed.

Chapter 4 deals with the synthesis and properties of Multiwalled Carbon Nanotube based magnetic heterostructures and their possible applications. This chapter discusses the synthesis of MWCNTs using chemical vapour deposition and their subsequent hybridization with magnetic materials. Filling of MWCNTs with aqueous ferrofluids by employing nanocapillarity are also described in this chapter. The microwave absorption properties of Ni filled MWCNTs are also investigated.

Evaluation of Non-linear Optical properties of magnetic nanowires of Ni, Co, Ni @ Co nanorods and their heterostructures with MWCNT is discussed in **Chapter 5**. A review on non-linear optics is provided at the beginning of the chapter for ensuring continuity. The theoretical fitting of experimental data is carried out by discussing various theories and mechanisms.

Chapter 6 presents the synthesis and properties of nanostructures of magnetic iron oxide. Acicular Iron oxide nanoparticles are synthesized using a novel technique by employing a complexing media and their optical and magnetic properties are discussed in this chapter.

A bird's eye view of the inferences drawn out of this investigation is provided in **Chapter 7**. The scope for further studies is also highlighted in this chapter.

Contents

Chapter 1	<i>Magnetic Nanostructures: An Overview</i>	1
1.1	Introduction	3
1.2	Classification of Nanostructures	4
1.3	Synthesis of Nanostructures: A brief Review	8
1.4	1-D Magnetic nanostructures	14
1.5	Carbon nanotubes	19
1.6	Magnetism -- An over view	24
1.6.1	Magnetic Domains	28
1.6.2	Magnetic anisotropy	29
1.6.2.1	Magnetocrystalline Anisotropy	29
1.6.2.2	Shape Anisotropy	30
1.6.2.3	Induced Magnetic Anisotropy	31
1.7	Fine particle magnetism	31
1.7.1	Single Domain Particles	32
1.7.2	Variation of coercivity with particle size	32
1.7.3	Superparamagnetism	34
1.7.4	Surface Anisotropy	35
1.8	Motivation of the thesis	36
1.9	Objectives of the thesis	41
	References	42
Chapter 2	<i>Experimental Techniques</i>	51
2.1	Fabrication techniques and tools	53
2.1.1	Electrodeposition	53
2.1.2	Potentiostat	55
2.2	Analysis tools and techniques	58
2.2.1	X-ray diffraction studies (XRD)	58
2.2.2	Scanning Electron Microscope (SEM)	60
2.2.3	Transmission Electron Microscopy (TEM)	62

2.2.4	High-Resolution TEM	64
2.2.5	Selected Area Electron Diffraction Pattern (SAED)	65
2.2.6	Energy Dispersive X-ray Spectroscopy (EDS)	66
2.2.7	Atomic Force Microscopy	66
2.2.8	Magnetic Force Microscopy (MFM)	69
2.2.9	Raman Spectroscopy	69
2.2.10	Fourier Transform Infrared Spectroscopy(FTIR)	70
2.2.11	UV-Visible Spectroscopy	72
2.2.12	Thermo-Gravimetric Analysis (TGA)	74
2.2.13	Magnetisation studies	75
2.2.13.1	Vibrating Sample Magnetometer (VSM)	75
2.2.13.2	SQUID Magnetometer	77
2.2.13.3	Field Cooled and Zero Field Cooled Measurements	78
	References	80

Chapter 3	<i>Fabrication of Magnetic Nanostructures of Nickel and Cobalt and Elucidation of Mechanism of Growth</i>	83
3.1	Introduction	85
3.2	Experimental	89
3.3	Results and Discussion	91
3.3.1	Nickel Nanowires and Tubes	91
3.3.2.1	Magnetisation studies on Ni Nanowires	95
3.3.2	Cobalt Nanowires and Tubes	100
3.3.2.2	Magnetisation studies on Co nanotubes	104
3.3.2.3	Magnetisation studies on Co nanowires	107
3.3.2.4	Thick-walled Co nanotubes	108
3.3.3	Mobility assisted Growth mechanism	109
3.3.4	Ni @ Co core-shell nanostructures	113
3.3.4.1	Fabrication of Ni @ Co nanorods	113
3.3.4.2	Magnetisation studies on Ni @ Co nanorods	116
	Conclusion	118

Chapter 4	<i>Synthesis and Properties of MWCNT Based Magnetic Heterostructures and Their Possible Applications</i>	125
4.1	Introduction	127
4.2	Experimental	132
4.2.1	Synthesis of MWCNTs	132
4.2.2	Metal filling inside MWCNTs	133
4.3	Results and discussion	133
4.3.1	Ni filled MWCNTs	135
4.3.2	Co filled MWCNTs	138
4.4	Microwave absorption studies using cavity perturbation method	142
4.5	MWCNT-SPION nanocomposites	149
4.5.1	Synthesis of Aqueous FF (AFF)	149
4.5.2	Synthesis of MWCNT-SPION composite	149
4.5.3	Magnetisation Studies	153
	Conclusion	159
	References	161
Chapter 5	<i>Evaluation of Nonlinear Optical Properties of Magnetic Nanostructures and Carbon Nanotube Based Hybrid Structures</i>	165
5.1	Introduction	167
5.2	Third order nonlinearity	169
5.3	Measurement of optical nonlinearity	170
5.4	Optical nonlinearity in nanostructured materials	171
5.4.1	Mechanisms	172
5.4.1.1	Nonlinear scattering	173
5.4.1.2	Multiphoton absorption	174
5.4.1.3	Free-carrier absorption	174
5.4.1.4	Reverse saturable absorption	175
5.5	Experiment	175

5.6	Result and discussion	177
5.6.1	z-scan studies on MWCNTs, Co NTs and cobalt-in-carbon nanotube hybrid structures	177
5.6.1.2	Theory of log-log plot	187
5.6.2	z-scan studies other magnetic nanostructures	189
	Conclusion	192
	References	193
<i>Chapter 6</i>	<i>Synthesis and Characterisation of Magnetic Iron Oxide Nanostructures</i>	<i>195</i>
6.1	Introduction	197
6.2	Experimental	198
6.2.1	Preparation of spherical $\gamma\text{Fe}_2\text{O}_3$ nanoparticles	198
6.2.2	Preparation of ellipsoidal iron oxide	199
6.2.3	Characterization	199
6.3	Results and Discussion	200
6.3.1	Structural and Morphological Studies using XRD and TEM	200
6.3.2	Magnetization studies using VSM	204
6.3.3	TG-DTG Studies	206
6.3.4	FT- IR Studies	207
6.3.5	Energy band gap calculation	208
	Conclusion	211
	References	212
<i>Chapter 7</i>	<i>Conclusion</i>	<i>215</i>
<i>Publications</i>		<i>225</i>

Chapter 1

Magnetic Nanostructures: An Overview

This chapter provides a comprehensive review on magnetic nanostructures which include wires, rods, tubes, thin films and particles. The crucial role of these structures in nanotechnology is brought out by considering some of their unique aspect ratio dependent properties. A brief account of the recent developments with regard to the synthesis of various magnetic nanostructures through different routes is provided, simultaneously discussing some of the fundamental issues related to controlling their dimensionality, stability and surface passivation. Potential applications of these structures in various fields are also discussed with special emphasis on carbon nanotubes. An overview on fine particle magnetism has been provided. The existing gaps in the literature with regard to low dimensional nanostructures are also dealt within this chapter. Finally, after illustrating some of the major advantages of structured magnetic materials, the objectives of the present investigation are listed.

1.1 Introduction

The realm of materials science underwent a sea change during the late 90's with the advent of Nanoscience and Nanotechnology. Now the sphere of materials science encompasses Physics, Chemistry and biology with a common denominator of nanoscience and nanotechnology. The developments that have occurred in quantum physics and the emergence of new fields like soft condensed matter physics all gave a new dimension to the wide area of materials science. The earlier notion of change in material properties by change in composition or mixing of different materials remained no more isolated and a radically different approach emerged in which, materials properties are engineered by changing the size by keeping the chemical composition intact.^[1-5] The methodology of varying the material characteristics with size is feasible only in a specific size regime, namely 'nano' meter (10^{-9} meter), where a quantum swapping of classical phenomena can be observed. This gave birth to a new branch in science and technology called 'Nanoscience' and 'Nanotechnology'.

Nanotechnology is being identified as the 'Technology of 21st century' with a multitude of opportunities for both fundamental and applied research. In recent years, 'nanotechnology' has carved out a new direction for itself in the area of research with enormous social importance representing an exciting, intellectually challenging and rapidly expanding area that trespasses the seamless borders between many branches of physical/biological sciences and engineering.^[6-8] Thus nanotechnology can be defined as the technology to fabricate, characterize, and manipulate structures whose features are controlled at the nanometer level.^[5] The research in this direction is triggered by the aid of state of the art instruments and approaches that allow the investigation of material properties with subatomic resolution.

The pioneering efforts have recently revealed new physical and chemical insights of materials at a level intermediate between atomic/molecular and bulk, which are expected to make a significant technological revolutions in the near future.^[9] The emergence and growth of nanostructured materials has actually been at an unprecedented rate, principally due to their unique and outstanding physical and chemical properties which could be controlled remarkably by tuning their morphology (i.e., size, shape, and dimensionality).^[10-17] A large number of prospective applications spanning wide areas such as optoelectronics, data storage, sensors, catalysis, energy storage, nanoelectronics, therapy, diagnosis and photochemistry could be realized due to the development of many innovative hybrid materials using these advances.^[17-24] Moreover, interesting new phenomena are also associated with these nanostructures, some of the examples include quantized or ballistic conductance, coulomb blockade or single electron tunneling, and metal-insulator transition all depending on some critical length scale.^[25-28]

1.2 Classification of Nanostructures

Dimensionality has a profound influence on the resultant physical and chemical properties of nanostructures and thus nanostructures can be classified according to their dimensionality. The classification scheme is a macroscopic approach and is based on the size dependence of some of the physical behaviours of the system.^[29] This could involve, for example, transport, usually of electrons/phonons, in which case an important length scale is the mean free path, λ . A system is said to be in a reduced dimensionality if the size, L_i of a macroscopic material is reduced sufficiently in one or more orthogonal directions, $i = (x, y, \text{ or } z)$, so that in those directions the mean free path is determined by the boundary scattering and not by some other intrinsic mechanisms for electrons/phonons. Reduced

dimensionality occurs when $\lambda_{int} > L_i$, so that $\lambda_{tot} \approx L_i$ for transport in the i^{th} direction, since the total mean free path is given by a reciprocal sum of intrinsic and extrinsic (boundary scattering) mechanisms, $\lambda_{tot}^{-1} = \lambda_{int}^{-1} + \lambda_{ext}^{-1}$ [30].

The reduced length scales (L_i) can also be related to the size of electronic wave function ' L_0 '. In this case, size quantization sets in if $L_i < L_0$. Hence, a zero dimensional system (strictly speaking quasi-zero dimensional) is one in which all three orthogonal lengths of a sample are less than λ_{int} and a quantum dot results when the length is such that $L_{x,y,z} < L_0$. Similarly, one-dimensional system is one in which two spatial dimensions are smaller than λ_{int} ; transport is then allowed along the remaining one dimension, unencumbered by boundary scattering. For example, a quantum wire is a one-dimensional sample with size quantization in two dimensions ($L_{y,z} < L_0$). They constitute an ideal and interesting system to study the dependence of electrical and thermal transport or mechanical properties on dimensionality and size confinement. Finally, a two-dimensional system is that in which only one spatial dimension is less than λ_{int} and hence transport is allowed in two dimensions, limited only by intrinsic scattering mechanisms. A quantum well is a two-dimensional sample with size quantization in the third dimension ($L_z < L_0$). Different dimensional nanostructures and their associated type of confinement are summarized in Figure 1.1.

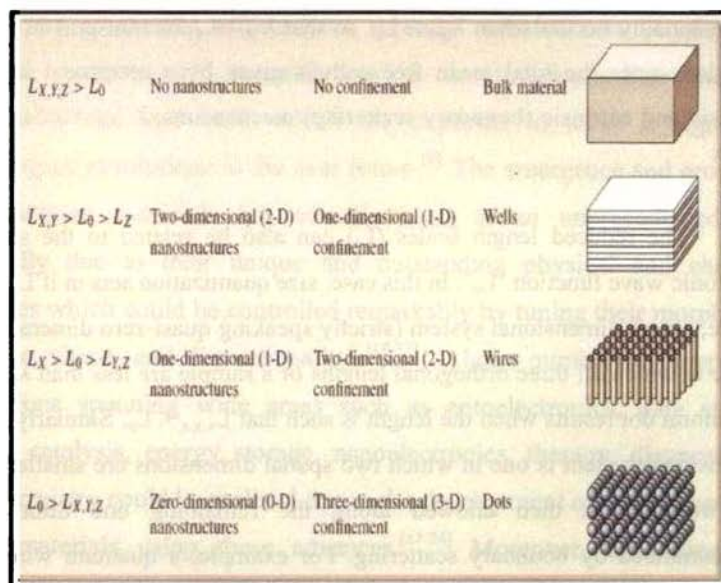


Figure 1.1 Schematic representations of reduced-dimensional material geometries (Reproduced from Ref.[30]).

The density of states (DOS) in nanostructures is strongly dependent on the dimensionality.^[5,31] The DOS for these nanostructures of different dimensionality is compared with that of a bulk solid as shown in figure 1.2.

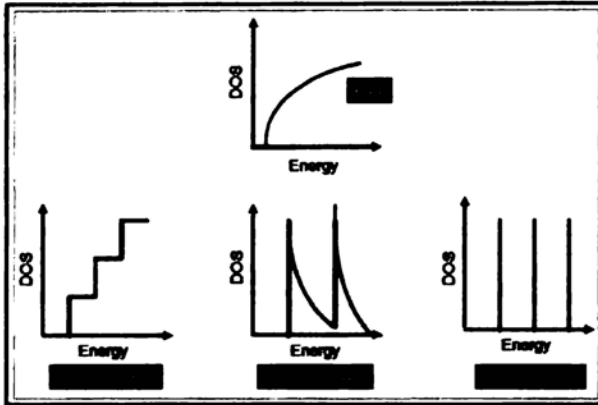


Figure 1.2 The electronic density of states of bulk material (3-D), quantum well (2-D), quantum wire (1-D) and quantum dot (0-D) (Reproduced from Ref.[5]).

It is clear that from figure 1.2 that, as the dimensionality is reduced from three to zero, DOS evolve from continuous levels to discrete states. Hence, it is obvious that DOS is strongly affected by the dimensionality reduction because of the corresponding reduction of degrees of freedom in wave vector space.

Exciting and unexpected results obtained from the past studies on low dimensional systems such as 2-D electron gas in semiconductor heterostructures and magnetic multilayers, and electron tunneling through 0-D quantum dots, have stimulated further research on nanostructured materials.^[7,32-34] Recently, 1-D nanostructures such as nanowires and nanotubes have also become the focus of intensive research owing to their unique applications in the fabrication of nanoscale devices.^[35-37] 1-D systems are the smallest dimensional structures that can be used for efficient transport of electrons/phonons and optical excitations, and are thus expected to be critical to the function and integration of nanoscale devices. However, little is known about the nature of carrier transport through a 1-D system.

Moreover, these systems should exhibit density of states singularities, for example Van Hove singularity in carbon nanotubes, can have energetically discrete molecule like states extending over large linear distances, which might show more exotic phenomena, such as the spin-charge separation predicted for a Luttinger liquid.^[38] There are also many other applications where 1-D nanostructures could be exploited, including nanoelectronics, superstrong and tough composites, functional nanostructured composites, and novel probe microscope tips.^[39-49]

The assembly of atoms or other building blocks logically into structures with nanometer size and desired (low) dimensionality is a key challenge before material scientists. A better insight and understanding of major factors which control the growth of the nanostructures is indispensable for assembling these nano-building blocks. There are two phenomenological approaches for the synthesis of systems of low dimensionality, top down and bottom up approaches. It has been quite clear in recent years that conventional “top-down” approaches are beset with many insurmountable experimental difficulties owing to various physical effects that are not easily scalable, and also because of the cost issues associated with nanoscale fabrication.^[49-53] This state of affairs has led to a great interest in the development of new methodologies based on bottom-up approaches. The following section briefly discusses some of the recent developments in the synthesis of nanostructures with a closer look at one-dimensional nanostructures.

1.3 Synthesis of Nanostructures: A brief Review

The manipulation of matter on the nanometer scale has become a central focus from both fundamental and technological perspectives. Unique, unpredictable, and highly intriguing physical, optical, electrical and

magnetic phenomena result from the confinement of matter into nanoscale features. Morphology control in nanostructures has become a key issue in the preparation of electronic or mechanical nano devices and functional materials.^[54]

As mentioned in the previous section, there are two general synthetic protocols for nanostructured materials; top-down approach and bottom-up approach. In the top-down approach, the bulk material is brought in to smaller dimension by various tools. These include mechanical alloying - mechanical attrition (High Energy Ball Milling) and radiation milling, various tools of patterning-chemical etching and optical lithography, and various methods to create ultra thin films of materials-thin film evaporation and sputtering. Bottom-up approach assures high monodispersity, possibility of further chemical derivatization, high degree of crystallinity and specificity, chemical integrity and lack of defects. Due to these reasons Bottom-up approach is thought to be more reliable than top-down approach.

There are two approaches in bottom-up method, gas phase approach and liquid state approach.^[55] In the gas phase approach, the material to be synthesized is mixed in the atomic state in the gas phase itself. The prepared material in the gas phase is condensed to get the bulk material. At the stage of condensation stabilizer materials can be added to control and preserve the shape and size of the formed particles. Various metal nanoparticles and oxides can be synthesized using this technique. The 'arrested precipitation' is the principal synthetic strategy used to make nanoparticles in solution.^[56] In this approach, at some stage of the particle growth, the surface is stabilized and further growth is arrested. The surface stabilization is commonly achieved by 'surfactants' which bind to the surface of the growing nanocrystal. Arresting the growth can also achieved by certain microcavities such as micelles, zeolites, porous membranes (such as polymer

membranes, alumina and silica). The sudden variation in temperature and pressure conditions during the growth of nanocrystals can lead to quenching and this will also lead to the arresting of the growth.

The most advanced chemical method for nanostructured materials processing is the deposition of colloid inorganic particles. Recent achievements in colloid chemistry have made a large variety of colloid compounds commercially available.^[57] The list of colloid nanoparticles with uniform (low-dispersed) dimensions in the range from 3 to 50 nm includes the noble metals (e.g., Au, Ag, Pt, Pd, and Cu), semiconductors (e.g., Si, Ge, III-V and II-VI, and metal oxides), insulators (e.g., mica, silica, different ceramic materials, polymers), and magnetic materials (e.g., Fe₂O₃, Ni, Co, and Fe). The growth of colloid particles is usually stabilized during synthesis by adding surfactants to the reagents. Therefore, the stable nanoparticles produced are coated with a thin shell of functionalized hydrocarbons, or some other compounds. Core-Shell nano systems represent a new class of hybrid materials and they can find immense applications in various engineering and biomedical fields. The deposition of colloid nanoparticles onto solid substrates can be accomplished by different methods, such as simple casting, electrostatic deposition, Self-assembly, Langmuir-Blodgett and spin coating techniques.^[57] In these techniques, self-assembly or chemical assembly is the simplest method of nanoparticle deposition and gives remarkable results.

Though there is no general strategy to make nanoparticles with narrow size distribution, tailored properties and desired morphologies that they could be universally applied to all materials, it is believed to follow Lamer mechanism for the formation of nanoparticles. Lamer mechanism^[58] suggests that a short burst of nucleation followed by slow diffusive growth, favour the formation of monodisperse crystalline nanoparticles. Also recent reports suggest that the synthesis is a multi-step process, which provide the

capability of producing controlled morphology, single and binary alloy nanoparticles, by separating the nucleation and particle growth during synthesis.

Solution based reduction technique is yet another commonly used chemical route for the synthesis of various nanoparticles such as Ag, Au, Pd, Pt, Co, Ni, Fe and Cu.^[59-61] Though some of the above metals need stabilizers, this method can employ nearly monodisperse nanoparticles. Sodium borohydrate, Sodium citrate, Potassium bitartrate, Dimethyl formamide, Ascorbic acid, and Alcohols are some of the reducing agents that have been successfully tested.^[62-70] Although significant progress has been attained in the synthesis of monodisperse noble metal nanoparticles, synthesis routes for magnetic Fe, Co and Ni nanoparticles are yet to be improved.^[71] Methods like inverse micelle and sonochemical decomposition of the metal carbonyls have been reported for the preparation of nanosized colloids of Co,^[72-73] Fe^[74-75] and Ni,^[76] and most of them yield polydisperse particles and are perhaps not suitable for scaling up because of the difficulty of reproducibility at high volumes and high concentration. Thermal decomposition of metal carbonyls is another novel approach for the synthesis of metal nanoparticles and it has an advantage over the reduction technique that it avoids the by-products like carbon monoxide.^[77-80] Moreover, bimetallic nanoparticles can also be prepared by this technique by the appropriate mixing of metal carbonyls.^[80-83]

Oxide nanoparticles particularly that of transition metals, constitute a very important class of materials offering a variety of functions. [84] Additionally, because of the high oxygen content of earth's atmosphere, oxides are some of the most stable materials formed and many transition metal oxides are biocompatible. Though different methods like hydrothermal and solvothermal preparation of oxide nanoparticles are reported,^[71,85] this

area considerably lags behind the state of art of metal or chalcogenide nanoparticles. Various methods like sol-gel,^[86] co-precipitation,^[87] and ceramic methods^[88] are in use to synthesize magnetic metal oxide nanoparticles. Decomposition of zero valent carbonyls, such as $\text{Fe}(\text{CO})_5$ in solvents and resultant oxidation of fine metal particles is another prevailing technique for the synthesis of metal oxide nanoparticles. Organic oxidants such as $(\text{CH}_2)_2\text{NO}$ can also be used for the synthesis of metal oxides from pure metals such as in the case of $\gamma\text{Fe}_2\text{O}_3$, where oxidation of bcc Fe leads to $\gamma\text{Fe}_2\text{O}_3$.^[89]

Studies on monolayer thin films started in the 1920s, initiated by Langmuir and Blodgett^[90] where they studied the formation of a monolayer of closely packed amphiphilic molecules on the surface of the aqueous subphase, followed by film transfer onto the solid substrate during its up-and-down movement through the water surface.^[57] The ideas of 'molecular systems' and 'molecular electronics' emerged in the beginning of 1970s and this paved way to the more sophisticated thin film fabrication tools such as molecular beam epitaxy. Two-dimensional nanostructures have been conveniently synthesized using techniques such as molecular beam epitaxy (MBE) and atomic layer deposition (ALD).^[91-94] These techniques offer precise control of deposition parameters possibly at the single atom level, along with the best film quality. The advent of highly precise thin film deposition systems in the later years of 1960s led to extensive research on magnetic multilayers and their spin dependent electronic transport. The pioneering works on these areas have been carried out by Albert Fert^[95] and Peter Grunberg^[96] independently and these works paved the way to the discovery of Giant Magneto Resistance (GMR) for which they were awarded Nobel Prize in the year 2007. From these it is to be concluded that significant progress has also been made with regard to the preparation and characterization of zero-dimensional (0-D) and two-dimensional (2-D)

nanostructures in the past two decades and several physical and chemical methods have already been developed for these nanostructures with well-controlled dimensions to prepare a broad range of materials.^[97-108]

However, in comparison with 0-D and 2-D nanostructures, the advancement in 1-D nanostructures (high aspect ratio nanostructures) have been rather slow until very recently, perhaps, due to difficulties associated with the synthesis of these nanostructures with well-controlled dimensions, morphology, phase purity, and chemical composition. Although high aspect ratio nanostructures can now be fabricated using a number of advanced nano-lithographic techniques, such as electron-beam or focused-ion-beam writing, proximal-probe patterning, and X-ray or extreme-UV lithography, further development of these techniques into practical routes for large quantities of structures, rapidly, and at reasonably low costs, still requires great ingenuity.^[109-114] In contrast, chemical as well as electrochemical routes might provide an alternate strategy for generating high aspect ratio structures in terms of material diversity, cost, and the potential for high-volume production.^[115-119] Moreover, since the catalytic reactivity of nanostructures depends on their morphology, it is important to design and prepare well-controlled shapes and sizes of these nanostructures for effective applications, especially in the field of catalysis and electrocatalysis.^[120]

1-D nanostructures got immediate attention soon after the landmark paper by Iijima^[121] on carbon nanotubes in 1991 and various types of organic-inorganic 1-D nanostructures were realised thereafter.^[122] As mentioned earlier, a generic method for the synthesis of 1-D nanostructures has not been available although a number of strategies have been persuaded.^[123] For example, multiwalled carbon nanotubes (MWCNTs) have been obtained from hot carbon plasmas.^[124-125] The growth mechanism producing MWCNTs under these conditions appears to be specific to the sp^2

bonded carbon and isostructural hexagonal boron nitride,^[126-127] although it is possible that other layered materials could form nanostructures.^[128-129] Moreover, for the synthesis of singlewalled carbon nanotubes (SWCNTs) presence of certain metals is found to be needed as catalysts^[130] and a sufficiently good understanding of the growth mechanism needed to control the diameter and helicity of SWCNTs is not available yet.

Template assisted synthesis is another versatile technique for the synthesis of 1-D nanostructures.^[8,131-133] The nanosized pores in membranes and zeolites have been used to confine the growth of wires/tubes. Alternatively, more sophisticated lithography and deposition techniques are available to create quantum wires on single crystal surfaces.^[134] Many other inorganic nanotubes and wires were also synthesized using the decomposition of precursor compounds containing the required elements.^[122] Hydrothermal method has been successfully used for the synthesis of nanotubes and related structures of a verity of inorganic materials such as SiO₂, V₂O₅, ZnO, dichalcogenide nanotubes etc.^[122] Template wetting and sol-gel chemistry are the other attempted routes for various inorganic nanotubes and wires such as Silica, TiO₂ and Barium titanate. Template assisted electrodeposition is a technique for the synthesis of various metallic as well as oxide nanotubes and nanowires. Electrodeposition over nanoporous membrane is a simple, low cost, and ingenious technique for 1-D nanostructures having high purity. Moreover, the ability to control the morphology during electrodeposition and large area of deposition make it unique among other nanoscale material fabrication techniques.

1.4 1-D Magnetic nanostructures

Recent progress on magnetism and magnetic materials have made magnetic nanostructures as a particularly interesting class of materials for both scientific and technological explorations.^[135] Studies on areas such as

interlayer coupling, giant magnetoresistance, colossal magnetoresistance, tunneling magnetoresistance, exchange bias, half-metallic ferromagnets, spin-injection, and current induced switching have led to exciting possibility of utilizing electron spin for information processing and this paved a way to a new branch known as 'spintronics'.^[136-137] Novel properties will start to emerge as the sample size becomes comparable to or smaller than certain characteristic length scales such as spin diffusion length, carrier mean free path, magnetic domain wall width, superconducting coherence length etc.

The effects of confinement, proximity, and degree of freedom govern the interplay between the relevant physical length scales and the sizes of the patterned magnetic materials.^[135] Ordered magnetic nanostructures are particularly interesting to study, as one can probe both the individual and collective behaviour of the elements in a well-defined and reproducible fashion. Moreover, ordered magnetic nanostructures are important technologically because of their application potential in magnetic random access memory, patterned recording media, biomedical applications and magnetic switches.^[138-139]

1-D magnetic nanostructures such as magnetic nanowires, nanotubes and hybrid magnetic nanostructures with carbon nanotubes, silica, and various polymers are receiving tremendous attention due to their importance in fundamental understandings of low dimensional physics, interwire/tube interactions and above all their tremendous application potential in high density storage media, energy storage devices, nanoelectronics, interconnects, radar absorbers and biomedical fields.^[140] The effect of lateral quantization (causing conductance quantization), weak and strong localization on electrical conductivity and magnetisation switching due to interwire interactions are well known to be important in magnetic nanowires

and their intensive study is still very popular, although there are no known practical applications for these interesting fundamental effects yet.

Most common method adopted to fabricate magnetic nanowires/tubes is the template assisted synthesis using carbon nanotubes or other nanopores as templates or cleaved edge of a molecular beam epitaxy-grown quantum well or DNA molecules as templates.^[141] Before this template assisted synthesis became popular, the established way to fabricate metallic magnetic nanowires was to shoot damage trails, and fill the damage trails with metals. After dissolving the plastic in a solvent, piles of short nanowires on the bottom of the beaker will be obtained. The template assisted synthesis has proved to be an elegant chemical approach for the fabrication of one dimensional nanostructures and an alternative to sophisticated methods such as molecular beam epitaxy and microlithography.^[142] Moreover, depending on the nature of material and on the other factors such as the chemistry of pore wall, the deposited cylinders can be solid (a nanowire) or hollow (a nanotube).

Studies on the metallic magnetic nanowires and nanotubes of Iron (Fe), Cobalt (Co) and Nickel (Ni) are highly promising and such studies are needed for the understanding of various magnetic interactions, anisotropy effects and transport properties. The understanding of magnetisation processes such as magnetic hysteresis of the wires and the time dependence of the magnetic reversal attained much scientific attention and immense works are in progress in the synthesis of nanowires and nanotubes of 3d transition metals. Moreover, ferromagnetic nanowires of Fe, Co and Ni are candidate materials for studying fundamental phenomena like micromagnetic reversal process quantum size effects.^[143-146] The modes of magnetisation reversal and other properties in a collective magnetic nanowire system are strongly influenced by the microstructure and the interwire separation.

A number of groups have been studied the magnetic properties of Fe nanowires^[147] and these studies concluded that the coercivity measured parallel to the nanowire ($H_c=2300$ Oe) is much higher than that perpendicular to the nanowire ($H_c=300$ Oe). This indicates that the wires possess uniaxial anisotropy with the easy axis along the wire axis. This is due to the high shape anisotropy of the wires and is often seen in magnets whose shapes can be approximated as thin cylinders or needles. Additionally, the coercivity also depend on the aspect ratio (wire length/wire diameter), and coercivity increase gradually with increasing aspect ratio, but increases very little with the aspect ratio larger than 10:1.^[147] Typical hysteresis loops of Co NWs in alumina template with aspect ratios greater than 20 resembles to that of Fe NWs. Co is an important ferromagnetic material with large coercivity and high curie temperature. Ni NWs were investigated by several groups mainly focusing on the correlation between the dimension of the wire and the hysteresis behaviour.^[148] Ni NWs possess their easy axis along the wire axis due to the high shape anisotropy. Magnetic interactions between nanowires play a seminal role in deciding the resultant magnetisation direction.

A complete understanding of the mechanism of magnetisation reversal in a tightly packed nanowire system remains elusive and it is persisting as a challenge for researchers. Tunable magnetic properties are essential for practical applications of nanowires. This can be achieved by many strategies.^[149] Changing the diameter will cause to the change in magnetic properties, but this will also alter the magnetic storage density and interaction between nanowires. The incorporation of nonmagnetic elements in to nanowires is another alternative for tuning the magnetic properties.^[150] Additionally this will affect the mechanical and thermal stabilities of nanowires. Synthesis of various alloys and heterostructures are other

strategies for tuning the magnetic properties with high thermal and mechanical stability.

Synthesis and studies on magnetic nanowires of alloys is another thrust area of research and different methodologies have been adopted for the synthesis of various alloys by different groups.^[151-152] Template assisted electrodeposition of mixed electrolytes in required molar ratio is a common method adopted for the synthesis of various alloys. Ferromagnetic alloys have potential applications in variety of fields such as wear-resistant, corrosion-resistant, heat -resistant materials, microelectronics, microsystem technology used for the manufacturing of sensors and actuators, micro relays and ultrahigh density storage media.^[153-154] Co-Ni, Cu-Ni, Fe-Ni alloy systems are some of the highly persuaded alloy systems. Systems containing Co are highly interesting due to the high possibility of tuning the magnetic properties by Co concentration.^[152]

Hybrid magnetic structures are another emerging trend in nanomagnetism with great interest in both applied and fundamental perspective. The combination of magnetic materials and Carbon nanotubes (CNTs) start to become promising research direction and substantial basic and engineering research is underway in this field.^[155] Recently, heterojunctions for interconnects are created between metal filled carbon nanotube using intense electron beam irradiation.^[156] Graphitic material interfaces with metal nanoparticles are highly promising for catalysis, hydrogen storage, radar absorbers, supercapacitors, and interconnects. Electrical, thermal, and mechanical properties of CNTs as well as magnetic properties of metals may get altered significantly with introduction of ferromagnetic metals in to CNTs.^[157] Different methods have been adopted by different groups to fill carbon nanotubes with metals and wet chemical method, capillary action, arc-discharge technique, catalysed hydrocarbon pyrolysis and condensed phase electrolysis some of them.^[158-160]

1.5 Carbon nanotubes

The synthesis of molecular carbon structures in the form of C_{60} and other fullerenes has stimulated intense interest in the structures accessible to graphitic carbon.^[121] As it follows from Louis Pater that 'Luck follows the prepared mind', Japanese scientist Sumio Iijima's mind was certainly well prepared for his amazing discovery in 1991. He could observe a new type of finite carbon structure consisting of needle like tubes, when an electrical spark between two closely spaced graphite rods is produced. These 'nanotubes' were hollow and layered like 'tubes inside tubes' and their ends sealed with conical caps and they are named multiwall carbon nanotubes (MWCNTs). By 1993, the many layered tubes had given way to single wall carbon nanotubes (SWCNTs) and whose properties are much easier to predict. Carbon nanotubes are curled cylinders of Graphite with both having a sp^2 hybridisation. Carbon nanotubes are one of the most important building blocks and materials in nanotechnology. Their unique combination of nano-sized diameter with macroscopic length scale has lead to many new phenomena and properties. Progress in large-scale synthesis, control of their structural properties, thin film transparent electrodes and nano-composites continues to widen their application in many new technologies.

Carbon nanotubes are one among the most extensively researched materials today.^[55] This is the most versatile material having the properties ranging from optical absorption and emission on one hand to the mechanical properties of bulk materials such as Young's modulus.

Among the two important allotropes of carbon, graphite and diamond, graphite is the thermodynamically stable bulk phase up to very high temperatures under normal ranges of pressure, but diamond is only kinetically stable.^[161] But, when the number of carbon atoms present becomes finite, the structure will energetically favour to close in cages or

rings for minimising the dangling bonds present. The cage structured carbon allotropes are called fullerenes,^[162] and the elongated ring shaped allotropes are called carbon nanotubes. The formation of curved structure from a planar hexagonal lattice demand certain topological defects included in the structure. To produce a convex structure, a positive curvature has to be introduced in to the planar hexagonal graphite structure and this is satisfied by creating pentagons along with the hexagonal structure. This is followed from Euler's principle that one needs exactly 12 pentagons to provide the topological curvature necessary to complete the hexagonal lattice. Hence in the case of Buckminster Fullerene (C_{60}) and all the other fullerenes there are many hexagons (C_{2n} has $(n-10)$ hexagons) but only 12 pentagons. This rule, so called pentagon rule is valid even for an elongated closed structure containing millions of hexagons, but there will be only 12 pentagons. A long cylinder made of hexagonal honeycomb lattice of carbon is named as carbon nanotubes.

A carbon nanotube can be thought to be formed from the graphite by the following way; a single layer of graphite called graphene can be fold in the form of a cylinder in such a manner that the open edges match perfectly to form a seamless structure. The resulting open ended tubes will be closed at some stage of the growth process by pentagons. The rolling up of graphene sheets in to cylinders can be carried out in many ways by satisfying the condition that dangling bonds present at both edges are matched. This introduces helicity to the tubular structure and helicity is the unique property of carbon nanotubes and it was the most revealing discovery that emerged out even in the first papers of Iijima.^[55,130] In the mapping of a graphene in to a cylinder, the boundary conditions around the cylinder can be satisfied only if one of the Bravais lattice vectors and a pair of integer indices (n, m) of the graphene sheet map to the whole circumference of the cylinder. This scheme is important in classifying the carbon nanotubes and depending on this index

the properties of the carbon nanotubes will differ. Nanotubes made from lattice translational indices of the form $(n, 0)$ and (n, n) have two helical symmetry operations whereas all other set of nanotubes, (n, m) have three equivalent helical operations. The $(n, 0)$ type of nanotubes are called zigzag nanotubes and (n, n) are called armchair nanotubes. All others (n, m) are named as helical. The indexing scheme that shows the folding procedure is shown in figure 1.3.

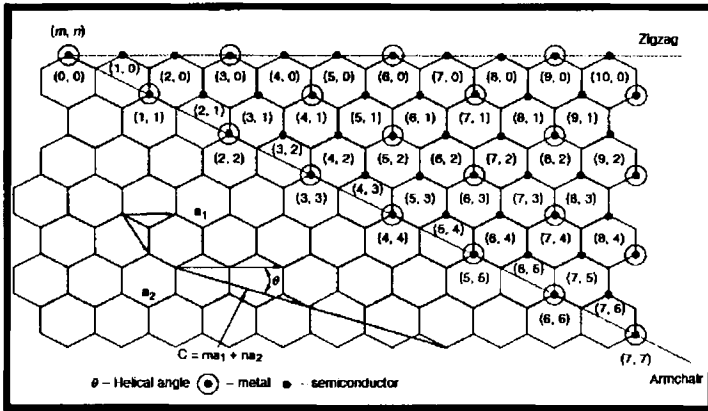


Figure 1.3: Schematic illustration of the folding procedure to create carbon nanotube cylinders (Reproduced from Ref.[161]).

The electronic conduction process in nanotubes is unique, since in the radial direction the electrons are confined in the singular plane of the graphene sheet. Calculations have predicted that all the armchair tubes are metallic whereas the zigzag and helical tubes can be either metallic or semiconducting.^[163-164] Generally it follows from the carbon nanotube indexing (n, m) that, if $(2n+m)/3$ is an integer, the corresponding nanotube will be metallic.

Carbon nanotubes in general can be categorized in to two categories, MWCNTs and SWCNTs. MWCNTs are made up of concentric graphene cylinders placed around a common central hollow with a spacing between the layers (0.34 nm) slightly greater than that in graphite (0.335 nm). The three dimensional structural correlation that prevails in single crystal graphite (ABAB stacking) is lost in MWCNTs and the layers are rotationally disordered with respect to each other. SWCNTs are similar to an ideal fullerene fiber with diameter close to the size of the fullerene (1-2 nm) and are single layered long cylinders. Normally MWCNTs are metallic in nature. Another major difference between MWCNTs and SWCNTs is the difference in their growth process. It required the presence of catalysts (transition metals Fe, Co, Ni, Au are some examples) for the synthesis, but no such catalyst is required for MWCNTs.^[161]

Arc discharge method has been employed by Iijima for the first time synthesis of CNTs (MWCNTs). Highly ordered nanotubular structures were created in the inter-electrode region, where the temperature is $\sim 3500^{\circ}\text{C}$ and these tubular structures are found to be self-assembled. Though the time scale for the formation of these nanostructures is extremely small, the amount of nanotubes obtained during arc deposition is limited. Moreover the deposit contains substantial amount of nanoparticles, hence the purification is a tedious task. There are other efficient techniques giving high quality nanotubes; they are catalytic vapour deposition, template assisted chemical vapour deposition, and laser ablation method. SWCNTs can be synthesized using a combination of catalyst and dense carbon vapour. Chemical vapour deposition with catalyst patterned surface is normally employed for the synthesis of SWCNTs. In a number of applications, such as field emission, aligned carbon nanotubes are required. Porous template assisted CVD and CVD over patterned substrate will often render aligned tubes.

The very high tensile strength of carbon nanotubes (for SWCNTs~45 GPa, which is 20 times that of steel; and that of MWCNTs is ~2-30 GPa) make them promising candidates for reinforcement applications.^[165] Moreover, they have applications in various fields such as nanotube based field emitters, as nanoprobe in meteorology, biological and chemical investigations, templates for the creation of various nanostructures, nanoelectronics and energy storage devices.^[166]

Multifunctional carbon nanostructures are currently under active investigation for producing innovative materials, composites, and optoelectronic devices, whose unique properties originate at the molecular level. The filling of carbon nanotubes with various metals and non-metals is thought as an ingenious idea right from the first report by Iijima et al.^[167] Carbon nanotube filled various composites have been fabricated for multifunctional applications.^[168] The application of functionalised CNT as a new method for drug delivery was immediately identified after the first demonstration of the capacity of this material to penetrate into cells.^[169]

Apart from the immense engineering and biomedical applications of filled carbon nanotubes, they are also unique candidates for studying the quantum mechanical effects such as confinement effects. Grobert et al. observed enhanced magnetic properties in magnetic metals filled MWCNTs.^[170] Similarly γ Fe (which is non-magnetic in bulk) is found to exhibit interesting magnetic properties when they encapsulated in carbon nanotubes.^[171] The combination of two classes of materials (CNTs and nanoparticles) may lead to a successful integration of the properties of the two components in the new hybrid materials that present important features for catalysis and nanotechnology.^[172] The focal theme of the present investigation is hybrid magnetic materials and a peep in to the exciting area of magnetism is provided in the ensuing sections.

1.6 Magnetism – An overview

Magnetic materials caught the attention of scientists even from the old days of civilisation and it continues to be a hot topic of research for both academic and applied fields.^[173] A pure magnetic system is a unique one to study the large scale collective behaviour of atoms and electrons. Different types of magnetic ordering are found to occur in nature and hence the response of different materials to the external magnetic field is also different.^[173-174] According to their behaviour in an external magnetic field, materials are broadly classified as diamagnetic, paramagnetic, ferromagnetic, antiferromagnetic and ferrimagnetic materials.

Diamagnetism is a fundamental property of all materials although it is usually very weak. It is due to the non-cooperative behaviour of orbiting electrons when exposed to an applied magnetic field. Diamagnetic substances are composed of atoms which have no net magnetic moments i.e. all orbital shells are filled and there are no unpaired electrons. However, when exposed to a field, a negative magnetisation is produced and thus the susceptibility is negative. Moreover, diamagnetic susceptibility is independent of temperature. Bismuth, Copper, Silver, and Gold are examples of diamagnetic materials.

In paramagnetism, some of the atoms or ions in the material have a non-zero magnetic moment due to unpaired electrons in partially filled orbitals. Then an applied field modifies the direction of the moments and an induced magnetisation parallel to the field appears. However the individual magnetic moments do not interact magnetically and like diamagnetism the magnetisation is zero when the field is removed. In the presence of field, there is now a partial alignment of the atomic magnetic moments in the direction of the field resulting in a net positive magnetisation and positive susceptibility. In addition, the efficiency of the field in aligning the moments is opposed by the randomizing effects of temperature. This results in a

temperature dependent susceptibility. Magnesium, Aluminium, Lithium, Molybdenum and Tantalum are some of the examples for paramagnetic materials.

Ferromagnetic materials are said to be 'magnetic' materials and unlike other types of materials, there exist a strong correlation between atomic magnetic moments. The interactions are produced by electronic exchange forces and result in a parallel or antiparallel alignment of atomic moments. The positive exchange interactions favour a parallel arrangement of magnetic moments in neighbouring atoms. Below a particular temperature called Curie temperature T_c , the interactions overcome randomisation due to thermal agitation and a spontaneous magnetisation appears in the presence of an applied magnetic field. The spontaneous magnetisation reaches its maximum value M_0 (called saturation magnetisation) at 0K corresponding to parallelism of all the individual moments. Above T_c , the thermal randomisation wins over exchange interaction and the material becomes paramagnetic. Figure 1.4 depicts a schematic of phase transition diagram of a ferromagnetic material with temperature.

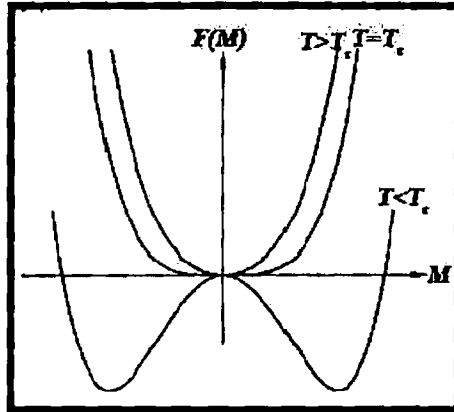


Figure 1.4: Schematic of phase transition (second order) of Paramagnetism – Ferromagnetism.

X-axis is of the phase transition curve represent the magnetisation (order parameter) and Y-axis is the Free energy (F). Below $T=T_c$, the free energy has two minima corresponding a non-zero value of spontaneous magnetisation (either +m or -m). But at $T=T_c$ or $T> T_c$, the free energy curve has a minimum only at $M=0$, indicates the net zero magnetisation. The 3d transition metals such as Fe, Co, and Ni exhibit ferromagnetism at room temperature. Two theories of magnetism were used to explain the ferromagnetism in metals: (i) localized moment theory (ii) band theory in the localized moment theory, the valence electrons are attached to the atoms and cannot move about the crystal. The valence electrons contribute to magnetic moment which is localized at the atom. The localized moment theory accounts for the variation of spontaneous magnetisation with temperature in the ferromagnetic phase and explains the Curie Weiss behaviour above the Curie temperature. In the collective electron model or band theory, the electrons responsible for magnetic effects are ionized from the atoms and are able to move through the crystal. Band theory explains the non integer values of the magnetic moment per atom that are observed in metallic

ferromagnets. In real situations neither model can be considered perfectly correct, but rather a good approximation. By far the most successful method currently available for calculating the magnetic properties of solids is density functional theory which includes all the interactions between all the electrons. Here it is assumed that the electrons choose the arrangement which will give them the lowest possible total energy. However Density Functional Theory (DFT) calculations are both intensive and difficult as the exact form of the exchange and correlation part of the inter-electronic interaction energy is not known.^[175]

In an antiferromagnet, exchange coupling between neighbouring moments that causes the moments to align in an antiparallel fashion: the exact opposite of a ferromagnet. In terms of Heisenberg Hamiltonian interaction, the exchange integral J_{ex} is negative. This antiparallel alignment causes the system to have small positive susceptibility, because an applied field tends to align the spins and this induced alignment is larger than the diamagnetism of the electron orbitals. Similar to ferromagnetic materials, the exchange energy can be defeated at high temperature and then the system becomes paramagnet. Fe_2TiO_2 , $ZnFe_2O_4$, and $CdFe_2O_4$ are some of the examples of antiferromagnetic materials.

Ferrimagnetism characterises a material which microscopically, is antiferromagnetic like, but in which the magnetisation of the two sublattices are not the same. The two sub lattices no longer compensate each other exactly. A finite difference remains to leave a net magnetisation. This spontaneous magnetisation is defeated by the thermal energy above a critical temperature called the Curie temperature and then the system is paramagnetic. Inverse spinel ferrites such as Fe_3O_4 , γFe_2O_3 and inverse spinel mixed ferrites are examples of ferrimagnetic materials.

The way the 'magnetic' materials get magnetised in an applied magnetic field is a highly intriguing question in magnetism. The interesting response of ferromagnetic materials to an applied magnetic field and the way they attained the technical magnetisation demand the concept of 'Domains'.

1.6.1 Magnetic Domains

Weiss first proposed that a ferromagnet contains a number of small regions called domains, where all the magnetic dipoles are aligned parallel to each other. When a ferromagnetic material is in its demagnetised state, the magnetisation averages to zero. The process of magnetisation causes all the domains to orient in the same direction. Domains are separated by domain walls. The formation of domains allows a ferromagnetic material to minimize its total magnetic energy. The main contribution to the magnetic energy are magnetostatic energy, magnetocrystalline energy and magnetostrictive energy which influence the shape and size of the domains.^[176] The technical magnetisation process can be explained by domain theory. In the initial demagnetised state, the domains are arranged that the magnetisation averages to zero. When the field is applied, the domain whose magnetisation is nearest to the field direction starts to grow at the expense of other domains. The growth occurs by domain wall motion is provided by the external magnetic field. Eventually the applied field is sufficient to eliminate all domain walls from the sample leaving a single domain, with its magnetisation pointing along the easy axis oriented closely to the external magnetic field. Further increase in magnetisation can occur only by rotating the magnetic dipoles from the easy axis of magnetisation into the direction of the applied field. The 'anisotropy' of magnetic materials is another important factor determining the magnetisation process.^[175]

1.6.2 Magnetic anisotropy

Magnetic anisotropy generally refers to the dependence of magnetic properties on the direction in which they are measured. The magnitude and type of magnetic anisotropy affect properties such as magnetisation and hysteresis curves in magnetic materials. The magnetic anisotropy can be of two types; intrinsic anisotropy as a result of its crystal chemistry or its shape and induced anisotropy as a result of some processing method.

1.6.2.1 Magnetocrystalline Anisotropy

Magnetocrystalline anisotropy is the tendency of the magnetisation to align itself along a preferred crystallographic direction. For example, body centered cubic Fe has the (100) direction as its easy axis. In nickel, which is a face centered cubic, the easy axis is (111). It is observed that the final value of the spontaneous magnetisation is the same, no matter which axis the field is applied along, but the field required to reach that value is distinctly different in each case. The physical origin of magnetocrystalline anisotropy is the spin orbit coupling resulting in orientation of the spins relative to the crystal lattice in a minimum energy direction, the so called easy direction of magnetisation.

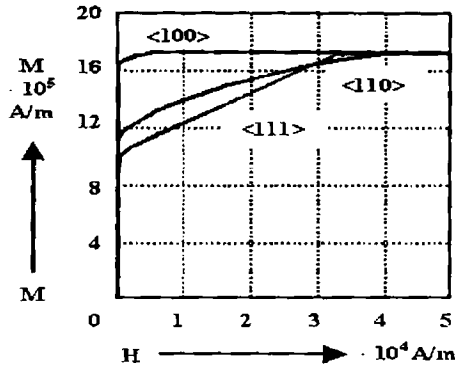


Figure 1.5: Schematic of anisotropy of magnetisation in Fe
(Reproduced from Ref.[176]).

Aligning the spins in any other direction leads to an increase in energy, the anisotropy energy E_k . For a cubic crystal E_k is related to two anisotropy constants K_1 and K_2 by

$$E_k = K_1 (\alpha_1^2 \alpha_2^2 + \alpha_2^2 \alpha_3^2 + \alpha_3^2 \alpha_1^2) + K_2 \alpha_1^2 \alpha_2^2 \alpha_3^2 \quad 1.1$$

where α_1 , α_2 and α_3 are the direction cosines of the magnetisation vector relative to the crystallographic axis. In all materials the anisotropy decreases with increasing temperature and near T_c , there is no preferred orientation for domain magnetisation.

1.6.2.2 Shape Anisotropy

In a non-spherical piece of material it is easier to induce a magnetisation along the long direction than along the short direction. This is because the demagnetization field is less along a short direction, because the induced poles at the surface are farther apart. For a spherical sample there is no spherical anisotropy. The magnetostatic energy density can be written as

$$E = \frac{1}{2} \mu_0 N_d M^2 \quad 1.2$$

where N_d is the tensor and represents the demagnetised factor (which is calculated from the ratio of the axis). M is the saturation magnetisation of the sample.

1.6.2.3 Induced Magnetic Anisotropy

Induced Magnetic Anisotropy is not intrinsic to the material, but is produced by treatment such as annealing which has directional characteristics. Both the magnitude of the anisotropy and the easy axis can be altered by appropriate treatments. Techniques such as casting, rolling or wire drawing is used to induce anisotropy in polycrystalline alloys.

1.7 Fine particle magnetism

The emergence of Nanoscience and Nanotechnology has made tremendous impact on 'magnetism', as it does well in other fields. The advent of sophisticated thin film deposition techniques in the early 1970, boosted the research on ultra-thin magnetic multilayers and their coupling. Interesting and intriguing phenomenon were observed and this motivated scientists to look the magnetic properties of low dimensional system.

Ultrafine magnetic particles with nanometric dimensions are found to exhibit novel properties compared to their conventional coarse grained counterparts. Magnetic nanoparticles are dominated by unique features like single domain nature, superparamagnetism and sometimes by unusual phenomena like spin glass and frustration. The variation of coercivity in ultrafine particles is also an interesting phenomenon. The unusual behaviour exhibited by nanoparticles is mainly due to two major reasons, finite size effects and surface effect.

1.7.1 Single Domain Particles

There is a minimum domain size in a ferromagnetic material below which the energy cost of domain formation exceeds the benefits from decreasing magnetostatic energy. This implies that a single particle of size comparable to the minimum domain size would not break up into domains. Qualitatively it is observed that if a particle is smaller than about ~100nm, a domain wall simply cannot fit inside it, resulting in single domain particles. A single domain particle has high magnetostatic energy but no domain wall energy, whereas a multidomain particle has lower magnetostatic energy but higher domain wall energy. The magnetisation curve for a single domain particle can be calculated using Stoner–Wohlfarth Model.^[175] The coherent domain rotation concept can be discussed as follows; let a magnetic field H is applied at an angle θ to a single domain particle having a uniaxial anisotropy. If the magnetisation of the particle lies at an angle ϕ to the magnetic field direction, the magnetic energy density of the system can be written as,

$$E = K\text{Sin}^2(\theta - \phi) - \mu_0 H M_s \text{Cos}\phi \quad 1.3$$

This energy can be minimized to find the direction of the magnetisation at any given value of the applied magnetic field. Analytic calculations are possible for this model for $\theta = 0$ to $\theta = \pi/2$.

1.7.2 Variation of Coercivity with particle size in fine particles

As the particle size is reduced, it is typically found that the coercivity increases, goes through a maximum and then tend towards zero. In a multidomain particle, magnetisation changes by domain wall motion. The size dependence of coercivity is experimentally found to be given by^[173]

$$H_{ci} = a + \frac{b}{D} \quad 1.4$$

where a and b are constants and D is the particle diameter

Below a critical particle size D_c , the particles become single domain and in this range the coercivity reaches a maximum. The particles with size D_c and smaller change their magnetisation with by spin rotation. As the particle size decreases below D_c , because of the thermal effects, the coercivity decreases according to the relation,

$$H_{ci} = g - \frac{h}{D^{3/2}} \quad 1.5$$

where g and h are constants.

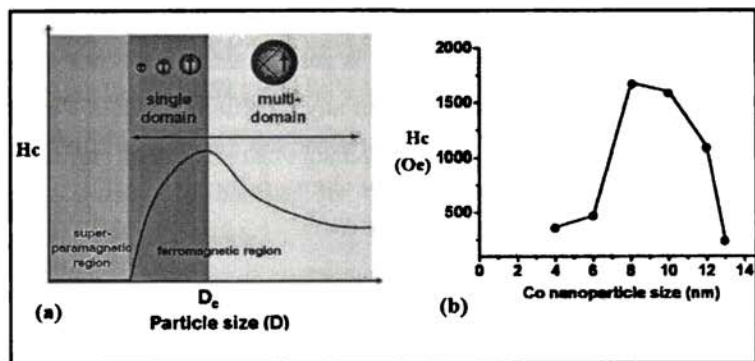


Figure 1.6: Schematic of the coercivity variation with particle size

(Reproduced from Ref.[175]).

Figure 1.6.a depicts the schematic of the coercivity variation with particle size reduction. It is to be noted that below a certain particle size the coercivity of the particles become zero. The particles now behave like paramagnetic particles, but with a giant individual particle magnetic moment. This phenomenon is known as Superparamagnetism.

1.7.3 Superparamagnetism

If single domain particles become small enough that, anisotropy energy KV , where K is the magnetic anisotropy constant and V the volume of the particle would become so small that the thermal fluctuations could overcome the anisotropy forces and spontaneously reverse the magnetisation of a particle from one easy direction to the other even in the absence of an applied field. As a result of the competition between anisotropy and thermal energies, assemblies of small particles show behaviour similar to paramagnetic materials, but with much larger magnetic moment. This moment is the moment of the particle and is equal to $m = M_s V$. It can be quite large amounting to thousands of Bohr Magnetons. An applied field would tend to align this giant moment, but $k_B T$ would fight the alignment just as it does in paramagnet. Thus this phenomenon is called superparamagnetism.^[173] If the anisotropy is zero or very weak, one would expect that the total moment could point in any direction. Hence a classical Langevin Function used for paramagnetism can be used to define magnetisation

$$M = NmL(x) \quad 1.6$$

$$\text{where } L(x) = \text{Coth}(x) - \frac{1}{x}; \quad x = \frac{\mu H}{k_B T} \quad 1.7$$

The two distinct features for superparamagnetic systems are (i) magnetisation curves measured at different temperatures superimpose when M is plotted as a function of H/T and (ii) there is no hysteresis: both remanence and coercivity are zero. The anisotropy energy KV represents an energy barrier to the total spin reorientation hence the probability for jumping thin barrier is proportional to the Boltzmann factor $\exp\left(-KV/k_B T\right)$.

At high temperature, the moments on the particles are able to fluctuate rapidly. The relaxation time τ of the moment of a particle is given by

$$\tau = \tau_0 \exp\left(\frac{KV}{k_B T}\right) \quad 1.8$$

where τ is typically 10^{-9} s.

These fluctuations slow down (τ increases) as the sample is cooled and the system appears static when τ becomes much larger than the measuring time of the particular laboratory experimental technique.

The typical experiment with a magnetometer takes 10 to 100 seconds. Using $\tau=100$ s and $\tau_0=10^{-9}$ s, we can obtain the critical volume as

$$V_{sp} = \frac{25k_B T}{K} \quad 1.9$$

A particle with volume less than this act superparamagnetically on the 100s experimental time scale. The equation can be rearranged to yield

$$T_B = \frac{KV}{25k_B} \quad 1.10$$

T_B is called the blocking temperature. Below T_B , the free movement of the magnetic moment is blocked by the anisotropy. Above T_B the system appears superparamagnetic.

1.7.4 Surface Anisotropy

In small magnetic nanoparticles, there can be another form of anisotropy arising out of surface effects. The surface anisotropy is caused by the breaking of the symmetry and their reduction of the nearest neighbour coordination. The protective shell or ligand molecules which cover the small particles play an important role as well leading to a change of the electronic environment on the particle surface. Surface frustrations and surface spin canting (particularly in magnetic oxide nanosystems) are other two important effects those play crucial role in fine magnetic particles.

Having discussed the various aspects of magnetism and magnetism at the nano level it is imperative that the motivation of the present investigation is spelt out clearly. The following section will take a close look at the motivation for the present investigation and finally the objectives will be spelt out clearly.

1.8 Motivation of the thesis

The impact felt by the emergence of Nanoscience and Nanotechnology on science was so high that, it carves out new directions in fundamental and applied research. Magnetism is one of the areas where the impact of nanoscience and nanotechnology is felt very much. The realization of novel devices based on Giant Magneto Resistance (GMR) and Magneto Caloric Effect (MCE) bear testimony to this fact. From the above discussion it can be seen that a lot more is to be understood on the surface of low dimensional magnetic system of 1D/2D types. This is essential not only in extracting the physics behind various phenomenon at these dimensions but also necessary for to tailoring various properties of these nanostructures for applications. Finally, these nanostructures are to be fabricated using appropriate method because knowledge of the history of the sample preparation and reaction conditions only will help to deduce the correct physics occurring at different stages of preparation.

Initial interest on ultra-thin nanomagnetic thin films now extends to other nanostructures like nanowires and nanoparticles as well due to their application potential in various fields such as data storage, sensors, biological probes and medical therapy. Moreover, structured magnetic materials like nanowires and nanotubes are in great demand due to their potential use in high density data storage and in nano electro-mechanical systems.

The rational assembly of the basic building blocks like atoms or molecules is a key challenge in the engineering of nanostructures and is important to fabricate various nanodevices and structures. There are some well developed methods like arrested precipitation ^[177-178] for 0D nanoclusters and molecular beam epitaxy for 2D nano layers.^[179] But, such a general method cannot be adopted for the growth of 1D nanostructures.

Though template assisted assembly is commonly accepted as a versatile technique, no specific strategy has been adopted for the synthesis of 1-D nanostructures like nanowires, nanotubes and nanorods. Electrodeposition over nanoporous templates is an inexpensive and ingenious technique to fabricate 1-D nanostructures. A general growth mechanism is lacking in the case of template assisted electrodeposition. Presently, engineering the 1-D nanostructures is accomplished by engineering the porous templates, but even this technique could not control the morphology between nanotubes and nanowires. This warrants a detailed investigations on template assisted electrodeposition with various precursors and templates. This is one of the objectives of the present investigation.

Magnetic hybrid structures containing more than one magnetic component are interesting materials where the magnetic properties can be suitably engineered by varying one of the components. Until very recently, this has been achieved by the nanowires and nanotubes of alloys. Core-Shell nanostructures represent a new class of nano system and magnetic core-shell system can control the magnetic properties by controlling the amount of one of the components. Understanding the growth mechanism during template assisted electrodeposition will help design multisegmented magnetic structures with controllable magnetic properties. A systematic study in this direction is not seen in the literatures and such a study will be interesting.

The small dimensions, remarkable strength and the physical properties of carbon nanotubes have caught up the fancy of many scientists and now they are among the most extensively researched materials. The absence of any natural magnetic ordering in carbon nanotubes prevent them from being put in to needful applications. Filling of carbon nanotubes with magnetic materials, which is accepted as an ingenious idea right from the early days of carbon nanotube research, is a viable alternative to impart magnetic properties to carbon nanotubes. A literature survey carried out on this area reveals that amount of magnetic material that can be impregnated in carbon nanotubes is limited and hence its usefulness. A complete filling of magnetic materials is also not attained yet. So multifunctional hybrid magnetic structures are another area of interest where they can find innumerable applications and not much work has been devoted to this aspect.

Carbon nanotube based magnetic structures can have a wide range of applications from radar absorbers to biological probes. The introduction of metals in to CNTs may lead to the modification of dielectric permittivity and magnetic permeability of the composite and this will enhance the microwave absorbing properties. The microwave absorbing properties of these nanostructures will also be of interest because of the smaller dimensions of these structures combined with the higher Snoek's limit and magnetic permeability needed for a good absorber. So yet another objective of the present investigation is to prepare hybrid magnetic nanostructures based on Co, Ni and MWCNTs.

Ferrofluids, which consist of fine magnetic particles suspended in a carrier fluid, are interesting nanomagnetic system having a range of applications from engineering to drug delivery. Moreover, they are unique systems to study the fine particle magnetism and magnetic interactions among them. Various quantum confinement effects such as blue shift due to weak confinement and strain induced redshift^[180] have been reported in

ferrofluids and synthesis of various kinds of ferrofluids is still an active area of research. A lot of ferrohydrodynamic modeling studies were carried out immediately after the first successful synthesis of ferrofluids by Rosenweig et al.^[181] The interesting quantum confinement effects due to the spatial confinement of magnetic particles are not subjected to investigation much.

Nanocapillarity is a complex phenomenon, the phenomenon of wetting the nanoporous channels by capillary force, and is a subject of intense investigation in leading laboratories all around the world. If the ferrofluids could fill the carbon nanotubes by nanocapillarity, it will be a versatile composite system to explore the confinement effects. The reports on biocompatibility of functionalised carbon nanotubes open another possibility of these composites in MRI contrast enhancement and magnetic field aided bio-medical drug delivery. So yet another motivation of the present study is to synthesize biocompatible aqueous ferrofluids and make multifunctional entities based on MWCNTs for various applications. The filling of MWCNTs will be achieved by nanocapillarity.

Non-linear optics plays a salient role in studying the light-matter interactions.^[182] Various materials such as inorganics, organics, organometallics and metals have been studied for their nonlinear optical properties in the past. Optical limiters are a class of nonlinear optical materials, which have potential applications in the protection of sensitive optical detectors and human eyes from accidental exposure to intense light beams. Recently, interest in the field of photonic devices has increased due to the advent of nano particles and nano structures. The nonlinear optical properties of magnetic nanostructures are not explored fully. If they are found to possess interesting optical properties, they will be unique systems having multiple functionalities. Though carbon nanotubes exhibit interesting

nonlinear light transition properties, their composites with magnetic materials are not seen investigated in literatures.

Different mechanisms such as nonlinear scattering, two or three photon absorption, and reverse saturable absorption phenomena including free carrier and excited state absorption are thought to be responsible for optical limiting. Moreover, in the case of a multisegmented system, possibility for the simultaneous occurrence of different mechanisms in the same system giving rise to strong optical limiting properties cannot be ruled out. So the studies on the nonlinear optical properties of magnetic hybrid structures are a fascinating area of research. This is another motive of the present investigation.

Nanomagnetic oxides are promising candidates for high density magnetic storage and other applications. Biocompatibility of magnetic oxide systems find applications in augmented drug delivery, drug targeting and MRI contrast enhancement agents. From a fundamental point of view, magnetic iron oxides are ideal templates for studying ferrimagnetism at the nano level since they possess an ideal two sub lattice with magnetic ions on either site. Synthesis of gamma iron oxide from precursors is also rather difficult, since they more often converted to more stable non-magnetic iron oxide phase. Nonspherical mesoscopic iron oxide particles are interesting candidate materials for studying the shape, size and strain induced modifications of various physical properties namely optical, magnetic and structural. The nonspherical nature of particles assumes to exhibit interesting magnetic and optical properties and these aspects are found to be not explored well in the literatures.

1.9 Objectives of the thesis

The specific objectives of the present investigation are as follows;

- ✚ Synthesis of magnetic nanowires and nanotubes of Ni and Co using various precursors using template assisted potentiostatic electrodeposition.
- ✚ Studies on the structural, morphological and magnetic properties of these nanowires and nanotubes.
- ✚ Formulation of a general growth mechanism for 1-D nanostructures during potentiostatic electrodeposition.
- ✚ Fabrication of hybrid 1-D structures of Ni and Co and verify the generalised growth mechanism.
- ✚ Synthesis of MWCNTs using template assisted Chemical Vapour Deposition and studies on their structure and morphology.
- ✚ Fabrication of carbon nanotube based magnetic heterostructures of Ni and Co using potentiostatic electrodeposition and their structural and magnetic characterizations.
- ✚ Evaluation of microwave absorbing properties of metal filled MWCNTs by cavity perturbation technique.
- ✚ Synthesis of MWCNT-superparamagnetic Iron Oxide composites using ferrofluids with aid of nanocapillarity.
- ✚ Evaluation of the nonlinear optical studies of nanowires and nanotubes of Ni and Co and their hybrid structures with MWCNTs.
- ✚ Synthesis of acicular Iron Oxide nanoparticles using complexing media and studies on their structural, magnetic and optical properties.
- ✚ Correlation of results.

References

1. Harrison, P. Quantum wells, wires and dots (2000) John Wiley, New York.
2. Barnham, K.; Vvedensky, D. (Eds.) Low dimensional semiconductor structures (2001) Cambridge University Press, Cambridge.
3. Davies, J. H. The physics of low dimensional semiconductors (1998) Cambridge University Press, Cambridge.
4. Delerue, C.; Lanno, M. Nanostructures (2004) Springer, New Delhi.
5. Schmid, G. Nanoparticles (2004) Wiley-VCH, Weinheim.
6. Alivisatos, A. P. Science (1996) 271 933.
7. Dvoret, M. H.; Esteve, D.; Urbina, C. Nature (1992) 360 547.
8. Martin, C. R. Science, (1994) 266 1961.
9. Kelsall, R.; Hamley, I.; Geoghegan, M. Nanoscale Science and Technology (2005) John Wiley & Sons, Ltd.: England.
10. Peng, X. G.; Manna, L.; Yang, W.; Wickham, J.; Scher, E.; Kadavanich, A.; Alivisatos, A. P. Nature (2000) 404 59.
11. Lieber, C. M. Solid State Commun. (1998) 107 607.
12. Smalley, R. E.; Yakobson, B. I. Solid State Commun. (1998) 107 597.
13. Gudiksen, M. S.; Lauhon, L. J.; Wang, J. F.; Smith, D.C.; Lieber, C. M. Nature (2002) 415 617.
14. Wong, E. W.; Sheehan, P. E.; Lieber, C. M. Science (1997) 277 1971.
15. Burda, C.; Chen, X.; Narayanan, R.; El-Sayed, M. A. Chem. Rev. (2005) 105 1025.
16. Morones, J. R.; Elechigueurra, J. L.; Camacho, A.; Holt, K.; Kouri, J. B.; Ramirez, J. T.; Yacaman, M. J. Nanotechnology (2005) 16 2346.
17. Lee, H.; Habas, S. E.; Kweskin, S.; Butcher, D.; Somorjai, G. A.; Yang, P. D. Angew. Chem. Int. Ed. (2006) 45 7824.
18. Morones, J. R.; Elechigueurra, J. L.; Camacho, A.; Holt, K.; Kouri, J. B.; Ramirez, J. T.; Yacaman, M. J. Nanotechnology (2005) 16 2346.
19. Rosi, N. L.; Mirkin, C. A.; Chem. Rev. (2005) 105 1547.
20. Xu, R.; Wang, D.; Zhang, J.; Li, Y. Chem. Asian J. (2006) 1, 888.
21. Kamat, P. V. J. Phys. Chem. B (2002) 106 7729.
22. Brugger, P. A.; Cuendet, P.; Gratzel, M. J. Am. Chem. Soc. (1981) 103 2923.

23. Guiling, R.; Jiefang, S.; Jinhua, L.; Xingguo, C.; Zhide, H.; Sesheng X. *Nanoscale Res. Lett.* (2009) 4 640.
24. De, M.; Ghosh, P. S.; Rotello, V. M. *Adv. Mater.* (2008) 20 1.
25. Krans, J. M.; van Rutenbeek, J. M.; Fisun, V. V.; Yanson, I. K.; de Jongh, L. J. *Nature* (1995) 375 767.
26. Al'tshuler, B. L.; Lee, P. A. *Phys. Today* (1988) 36.
27. Likharev, K. K.; Claeson, T. *Sci. Am.* (1992) 80.
28. Likharev, K. K. *IBM J. Res. Dev.* (1988) 32, 144.
29. Elliot, S. R. *The Physics and Chemistry of solids*, Wiley-VCH (2003).
30. Martienssen, W.; Warlimont, H. *Springer Handbook of Condensed Matter and Materials Data*, (2005).
31. Poole, C. P. Jr.; Owens, F. J. *Introduction to Nanotechnology*; John-Wiley and Sons, Inc.: New Jersey, (2003).
32. Stormer, H. L. *Solid State Commun.* (1998) 107 617.
33. Klein, D. L.; Roth, R.; Lim, A. K. L.; Alivisatos, A. P.; McEuen, P. L. *Nature* (1997) 389 699.
34. Jiles, D. C. *Acta Materials (Topical Review)* 51(2003) 5907.
35. Wang, Z. L. *Adv. Mater.* (2000) 12 1295.
36. Hu, J.; Odom, T. W.; Lieber, C. M. *Acc. Chem. Res.* (1999) 32, 435.
37. A Special issue in *MRS Bull.* (1999) 24, 20.
38. Kane, C.; Balents, L.; Fisher, M. P. A. *Phys. Rev. Lett.* (1997) 79 5086.
39. Bockrath, M.; Cobden, D. H.; McEuen, P. L.; Chopra, N. G.; Zettl, A.; Thess, A.; Smalley, R. E. *Science* (1997) 275 1922.
40. Tans, S. J.; Devoret, M. H.; Dai, H.; Thess, A.; Smalley, R. E.; Geerligs, L. J.; Dekker, C. *Nature* (1997) 386 474.
41. Tans, S. J.; Verschueren, A. R. M.; Dekker, C. *Nature* (1998) 393 49.
42. Yang, P.; Lieber, C. M. *Science* (1996) 273 1836.
43. Yang, P.; Lieber, C. M. *Appl. Phys. Lett.* (1997) 70 3158.
44. Yang, P.; Lieber, C. M. *J. Mater. Res.* (1997) 12 2981.
45. Dai, H.; Hafner, J. H.; Rinzler, A. G.; Colbert, D. T.; Smalley, R. E. *Nature* (1996) 384 147.
47. Wong, S. S.; Harper, J. D.; Lansbury, P. T.; Lieber, C. M. *J. Am. Chem. Soc.* (1998) 120 603.

48. Ajayan, P. M.; Tour, J. M. *Nature* (2007) 447 1066.
49. Schmid, G. *Clusters and Colloids: From theory to applications*, (1994) Wiley-VCH: New York.
50. Mirkin, C. A.; Rogers, J. A. *MRS Bull.* (2001) 26 506.
51. Odom, T. W.; Nehl, C. L. *ACS Nano* (2008) 2 612.
52. Hawker, C. J.; Russel, T. P. *MRS Bull.* (2005) 30 952.
53. Li, M.; Coenjarts, C. A.; Ober, C. K. *Adv. Polym. Sci.* (2005) 190 183.
54. Athanassiou, E. K.; Grossmann, P.; Grass, R. N.; Stark, W. J. *Nanotechnology* (2007) 18 165606 (7pp).
55. Pradeep, T. *Nano, Essentials*, Tata McGraw-Hill Publishing Company, New Delhi (2007).
56. Hadjipanayis, G. C.; Siegel, R.W. *Nanophase Materials Synthesis Properties Applications* (1993) Kluwer Academic Publishers, The Netherlands.
57. *Organic and Inorganic nanostructures*, Alexei Nabok, Artech House Inc. Norwood MA (2005).
58. Lamer, V. K.; Pinegar, R. H. *J Am. Chem. Soc.* (1950) 72 4847
59. Masala, O.; Seshadri, R. *Annu. Rev. Mater. Res.* (2004) 34 41.
60. Faraday, M. 1857, *Phil. Trans. R. Soc. London*, 147, 145-181.
61. Brust, M.; Walker, M.; Bethell, D.; Schiffrin, D. J.; Whyman, R. *Chem. Commun.* (1994) 7 801.
62. Heath, J. R.; Knobler, C. M.; Leff, D. V. *J. Phys. Chem. B* (1997) 101 189.
63. He, S.; Yao, J.; Jiang, P.; Shi, D.; Zhang, H. *Langmuir* (2001) 17 1571.
64. Li, X; Zhang, J.; Xu, W.; Jia, H.; Wang, X. *Langmuir* (2003) 19 4285.
65. Tan, Y.; Li, Y.; Zhu, D. 2003, *J. Coll. Int. Sci.*, 258, 244.
66. Pastoriza, S. I.; Liz, M. L. M. *Langmuir* (1999) 15, 948.
67. Tan, Y.; Dai, X.; Li, Y., Zhu, D. *J. Mater. Chem.* (2003) 13 1069.
68. Sondi, I.; Goia, D. V.; Matijevic, E. *J. Coll. Int. Sci.* (2003) 260 75.
69. Lee, C.; Wan, C.; Wang, Y. *Adv. Fun. Mater.* (2001) 11 344.
70. Ayyappan, S.; Gopalan, S. R.; Subbanna, G. N.; Rao, C. N. R. *J. Mater. Res.* (1997) 12 398.
71. Hyeon, T. *Chem. Commun.* (2003) 8, 927.
72. Petit, C.; Taleb, A.; Pileni, M. P. *J. Phys. Chem. B* (1999) 103 1805.

73. Lin, X. M.; Sorensen, C. M.; Klabunde, K. J.; Hadjipanayis, G. C. *Langmuir* (1998) 14 7140.
74. Wilcoxon, J. P.; Provencio, P. P. J. *Phys. Chem. B* (1999) 103 9809.
75. Suslick, K. S.; Hyeon, T.; Fang, M. *Chem. Mater.* (1996) 8 2172.
76. Chen, D. H.; Hsieh, C. H. J. *Mater. Chem.* (2002) 12 2412.
77. Murray, L. B.; Sun, S.; Doyle, H.; Betley, T. *MRS Bull.* (2001) 26 985.
78. Dinega, D. P.; Bawendi, M. G. *Angew. Chem. Int. Ed.* (1999) 38 1788.
79. Park, S. J.; Kim, S.; Lee, S.; Khim, Z. G.; Char, K.; Hyeon, T. J. *Am. Chem. Soc.* (2000) 122 8581.
80. Li, Y.; Liu, J.; Wang, Y.; Wang, Z. L. *Chem. Mater.* (2001) 13 1008.
81. Sun, S.; Murray, C. B.; Weller, D.; Folks, L.; Moser, A. *Science* (2000) 287 1989.
82. Sobal, N. S.; Ebles, U.; Mohwald, H.; Giersig, M. J. *Phys. Chem. B* (2003) 107 7351.
83. Chen, M.; Nikles, D. E. *J. Appl. Phys.* (2002) 91, 8477.
84. Rao, C. N. R. *Annu. Rev. Phys. Chem.* (1989) 40 291.
85. Rajmathi, M.; Seshadri, R. *Curr. Opin. Solid State Mater. Sci.* (2002) 6 337.
86. George, M.; John, A. M.; Nair, S. S.; Joy, P. A.; Anantharaman, M. *R. J. Magn. Mater.* (2006) 302 190.
87. Nair, S. S.; Thomas, J.; Suchand Sandeep, C. S.; Anantharaman, M. R.; Philip, R. *Appl. Phys. Lett.* (2008) 92 171908.
88. Malini, K. A.; Anantharaman, M. R.; Sindhu, S. *Int. J. Plastics and Rubber Composites* (2002) 31 449.
89. Hyeon, T.; Chung, Y.; Park, J.; Lee, S. S.; Kin, Y. W.; Park, B. H. J. *Phys. Chem. B* (2002) 106 6831.
90. Chen, X.; Lenhert, S.; Hirtz, M.; Lu, N.; Fuchs, H.; Chi, L. *Acc. Chem. Res.* (2007) 40 393.
91. Herman, M. A.; Sitter, H. *Molecular Beam Epitaxy-Fundamentals and Current Status*; Springer-Verlag: Berlin, (1989).
92. Parker, E. H. C. *The Technology and Physics of Molecular Beam Epitaxy*; Plenum Press: New York, (1985)
93. Ritala, M.; Leskela, M. *Nanotechnology* (1999) 10 19.
94. Puurunen, R. L. *J. Appl. Phys.* (2005) 97 121301.

95. Baibich, M. N.; Broto, J. M.; Fert, A.; Nguyen, F.; Petroff, F. *Phys. Rev. Lett.* (1988) 61 2472
96. Binasch, G.; Gruenberg, P.; Saurenbach, F.; Zinn, W. *Phys. Rev. B* (1989) 39 4828.
97. Berchmans, S.; Thomas, P. J.; Rao, C. N. R. *J. Phys. Chem. B* (2002) 106 4647.
98. Lee, D.; Donkers, R. L.; DeSimone, J. M.; Murray, R. W. *J. Am. Chem. Soc.* (2003) 125 1182.
99. Pillai, Z. S.; Kamat, P. V. *J. Phys. Chem. B* (2004) 108 945.
100. Chaki, N. K.; Singh, P.; Dharmadhikari, C. V.; Pillai, V. K. *Langmuir* (2004) 20 10208.
101. Peng, X. *Adv. Mater.* (2003) 15 459.
102. Schmid, G. *Nanoparticles: From Theory to Application*; Wiley-VCH: (2004).
103. G. Cao, *Nanostructures and Nanomaterials: Synthesis, Properties and Applications*; Imperial College London, (2004).
104. Egusa, S.; Redmond, P. L.; Scherer, N. F. J. *Phys. Chem. C* (2007) 111 17993.
105. Brust, M.; Walker, M.; Bethell, D.; Schiffrin, D. J.; Whyman, R. J. *Chem. Soc., Chem. Commun.* (1994) 801.
106. Kim, M. -K.; Jeon, Y. -M.; Jeon, W. S.; Kim, H. -J.; Hong, S. G.; Park, C. G.; Kim, K. *Chem. Commun.* (2001) 667.
107. Ganesan, M.; Freemantle, R. G.; Obare, S. O. *Chem. Mater.* (2007) 19 3464.
108. Peng, S.; Wang, C.; Xie, J.; Sun, S. J. *Am. Chem. Soc.* (2006) 128 10676.
109. Cerrina, F.; Marrian, C. *MRS Bull.* (1996) 21 56.
110. Matsui, S.; Ochiai, Y. *Nanotechnology* (1996) 7 247.
111. Hong, S. H.; Zhu, J.; Mirkin, C. A. *Science* (1999) 286 523.
112. Dagata, J. A. *Science* (1995) 270 1625.
113. Levenson, M. D. *Solid State Technol.* (1995) 38 81.
114. Menke, E. J.; Thompson, M. A.; Xiang, C.; Yang, L. C.; Penner, R. M. *Nature Mater.* (2006) 5 914.
115. Gou, L.; Murphy, C. J. *Chem. Mater.* (2005) 17 3668.
116. Wiley, B.; Sun, Y.; Xia, Y. *Acc. Chem. Res.* (2007) 40 1067.
117. Choi, J.; Sauer, G.; Nielsch, K.; Wehrspohn, R. B.; Gosele, U. *Chem. Mater.* (2003) 15 776

118. Xia, Y.; Rogers, J. A.; Paul, K. E.; Whitesides, G. M. *Chem. Rev.* (1999) 99 1823.
119. Yu, Y. -Y.; Chang, S. -S.; Lee, C. -L.; Wang, C. R. C. *J. Phys. Chem. B* (1997) 101 6661.
120. Narayanan, R.; El-Sayed, M. A. *Nano Lett.* (2004) 4 1343.
121. Iijima, S. *Nature* (1991) 354 56.
122. Rao, C. N. R.; Nath, M. *Dalton Trans.* (2003) 1.
123. Hu, J.; Odom, T. W.; Lieber, C. M. *Acc. Chem. Res.* (1999) 32 435.
124. Colbert, D. T.; Zhang, J.; McClure, S. M.; Nikolaev, P.; Chen, Z.; Hafner, J. H.; Ownes, D. W.; Kotuja, P. G.; Carter, C. B.; Weaver, J. H.; Smalley, R. E. *Science* (1994) 266 1218.
125. Ebbesen, T. W.; Ajayan, P. M. *Nature* (1992) 358 220.
126. Chopra, N. G.; Luyken, R. J.; Cerry, K.; Crespi, V. H.; Cohen, M. L.; Louie, S. G.; Zehi, A. *Science* (1995) 269 966.
127. Terrones, M.; Hsu, W. K.; Terrones, H.; Zhang, J. P.; Ramos, S.; Hare, J. P.; Castillo, R.; Prassides, K.; Kroto, H. W.; Watton, D. R. *M. Chem. Phys. Lett.* (1996) 259 568.
128. Tenne, R.; Margulis, L.; Lenut, M.; Hodes, G. *Nature* (1992) 360 444.
129. Feldman, Y.; Wasserman, E.; Srolovit, D. J.; Tenne, R. *Science* (1995) 267 222.
130. Iijima, S.; Ichihashi, T. *Nature* (1993) 363603.
131. Wu, C. G.; Bein, T. *Science* (1994) 266 1013.
132. Dai, H.; Wang, E. W.; Lu, Y. Z.; Fan, S.; Lieber, C. M. *Nature* (1995) 375 769.
133. Wong, E. W.; Maynor, B. W.; Burns, L. D.; Lieber, C. M. *Chem. Mater.* (1996) 8 2041.
134. Namatsu, H.; Kurihara, K.; Nagase, M.; Makino, T. *Appl. Phys. Lett.* (1997) 70 619.
135. Martin, J. J.; Noguees, J.; Liu, K.; Vicent, J. L.; Schuller, I. K. J. *Magn. Mater.* (Topical Review) 256 (2003) 449.
136. Prinz, G.; Hathaway, K. (Eds.) *Magnetoelectronics*, *Phys. Today* 48(4) (1995) (special issue).
137. Levy, P. M.; Zhang, S.; Fert, A. *Phys. Rev. Lett.* 65 (1990) 1643].
138. Cowburn, R. P. *Science* 287 (2000) 1466.
139. White, R. L.; New, R. M. H.; Pease, R. F. W. *IEEE Tran. Magn.* 33 (1997) 990.

140. Cao, H.; Wang, L.; Qiu, Y.; Wu, Q.; Wang, G.; Zhang, L.; Liu, X. *ChemPhysChem* (2006) 7 1500.
141. Fasol, G. *Science* 280 (1998) 545.
142. Fert, A.; Piraux, L. *J. Magn. Magn. Mater.* (1999) 200, 338.
143. Sahoo, S.; Petravic, O.; Kleemann, W.; Stappert, S.; Dumpich, G.; Nordblad, P.; Cardoso, S.; Freitas, P. P. *Appl. Phys. Letts.* (2003) 82, 4116.
144. Garcia, J. M.; Asenjo, A.; Velazquez, J.; Garcia, D.; Vazquez, M.; Aranda, P.; Hitzky, E. *R. J. Appl. Phys.* (1999) 85 5480.
145. Martin, J. I.; Nogues, J.; Liu, K.; Vicent, J. L.; Schuller, I. K. *J. Magn. Magn. Mater.* (2003) 256 449-451.
146. Yu, C. Y.; Yu, Y. L.; Sun, H. Y.; Xu, T.; Li, X. H.; Li, W.; Gao, Z. S.; Zhang, X. Y. *Material Letters* (2007) 61 1859.
147. Sellmyer, D. J.; Zheng, M.; Skomski, R. *J. Phys.: Condens. Matter.* 13 (2001) R433.
148. Razeeb, K. M.; Rhen, F. M. F.; Roy, S. *J. Appl. Phys.* (2009) 105 083922.
149. Huang, X. H.; Li, G. H.; Dou, X. C.; Li, L. *J. Appl. Phys.* (2009) 105 084306.
150. Wang, Y. W.; Zhang, L. D.; Meng, G. W.; Peng, X. S.; Jin, Y. X.; Zhang, J. *J. Phys. Chem. B* (2002) 106 2502.
151. Wu, C. G.; Lin, H. L.; Shau, N. L. *J. Solid State Electrochem* (2006) 10 198.
152. Talapara, S.; Tang, X.; Padi, M.; Kim, T.; Vajtai, R.; Sastry, G. V. S.; Shima, M.; Deevi, S. C.; Ajayan, P. M. *J. Mater. Sci.* (2008) DOI: 10.1007/s10853-008-3015-1.
153. Sunder, R. S.; Deevi, S. C. (2005) *Int. Mater. Rev.* 50 1.
154. Zhu, H.; Yang, S.; Ni, G.; Yu, D.; Du, Y. (2001) *Scripta Mater.* 44 2291.
155. Muhl, T.; Elefant, D.; Graff, A.; Kozhuharova, R.; Leonhardt, A.; Monch, I.; Ritschel, M.; Simon, P.; Zotova, S. G.; Schneider, C. M. *J. Appl. Phys.* (2003) 93, 10.
156. Julio, A. R. M.; Banhardt, F.; Terrones, M.; Grobert, N.; Ajayan, P. M.; Sumpter, B. G.; Wang, M.; Bando, Y.; Golberg, D. *PNAS* (2009) 106 12 4591.
157. Reddy, A. L. M.; Ramaprabhu, R. *Nanoscale Res. Lett.* (2008) 3 76.

158. Tsang, S. C.; Chen, Y. K.; Harris, P. J. F.; Green, M. L. H. *Nature* (1994) 372 159.
159. Ajayan, P. M.; Ebbesen, T. W.; Ichihashi, T.; Iijima, S.; Tanigaki, K.; Hiura, H. *Nature* (1993) 362 522.
160. Subramoney, S. *Adv. Mater.* 10, 1157 (1998). Kyotani, T.; Tsai, L. F.; Tomita, A. *Chem. Comm.* (1997) 701.
161. Ajayan, P. M. *Chem. Rev.* (1999) 99 1787
162. Kroto, H. W.; Heath, J. R.; O'Brien, S. C.; Curl, S. C.; Smalley, R. E. *Nature* (1985) 318 162.
163. Yakabson, B. I.; Smalley, R. E. *Am. Sci.* (1997) July-August 324.
164. Saiti, R.; Dresselhaus, M. S.; Dresselhaus, G. *Physical Properties of Carbon nanotubes* (1998) World scientific New York.
165. *Aligned Carbon Nanotubes*, Wang, X.; Liu, Y.; Zhu, D. *Encyclopedia of Nanoscience and nanotechnology*, Nalwa, H. S. (Edt.), Vol. 1 American Scientific Publishers.
166. Ajayan, P. M.; Zhou, O. Z. *Applications of carbon nanotubes, in carbon nanotube synthesis, structure, properties and applications* (eds. M. S. Dresselhaus, G. Dresselhaus and Ph. Avouris), Springer publications (2001) (Book chapter).
167. Ajayan, P. M.; Iijima, S. *Nature* (1993) 361 333.
168. *Filling of carbon nanotubes*, P. K. Tyagi, M. K. Singh, D. S. Misra. *Encyclopedia of Nanoscience and Nanotechnology*, 3 417 (2004).
169. Bianco, A.; Kostarelos, K.; Prato, M. *Curr. Opin. Chem. Biol.* (2005) 9(6)674.
170. Gobert, N.; Hsu, W. K.; Zhu, Y. Q.; Hare, J. P.; Kroto, H. W. *Appl. Phys. Lett.* (1999) 75 3363.
171. Wei, B. Q.; Shima, M.; Pati, R.; Nayak, S. K.; Singh, D. J.; Li, Y. B.; Nasu, S.; Ajayan, P. M. *Small* (2006) 2 804.
172. Georgakilas, V.; Gournis, D.; Tzitzios, V.; Pasquato, L.; Guldi, D. M.; Prato, M. *J. Mater. Chem.* (2007) 17 2679.
173. Cullity, B. D. *Introduction to Magnetic Materials*, (1972) Addison-Wesley Publ. Com.
174. Chikazumi, S. *Physics of magnetism*, John Wiley and Sons Inc., New York (1964).
175. Blundell, S. *Magnetism in Condensed Matter*, Oxford Master Series in Condensed Matter, Oxford (2001).

176. Nicola, S. *Magnetic Materials Fundamentals and device applications*, Cambridge University Press, Cambridge (2003).
177. Murray C. B.; Norris, D. J.; Bawendi, M. G.; *J. Am. Chem. Soc.* (1993) 115 8706.
178. Dabbousi, B. O.; Rodriguez, V. J.; Mikulec, F. V.; Heine, J. R.; Mattoussi, H.; Ober, R.; Jensen, K. F. Bawendi, M. C. *J. Phys. Chem. B* (1997) 101 9463.
179. Herman, M. A.; Slitter, H. *Molecular Beam Epitaxy* Springer New York (1989).
180. Nair, S. S.; Mathew, M. Anantharaman, M. R. *Chem. Phys. Lett.* (2005) 408 398.
181. Rosensweig, R. E. *Ferrohydrodynamics* Cambridge University Press, Cambridge (1985).
182. Sutherland, R. L. *Hand book of nonlinear optics*, (2003) Second edition, Marcel Dekker, Inc. New York.

Chapter 2

Experimental Techniques

The advent of nanoscience and nanotechnology demands state of the art microcharacterisation tools. Most of the methods involve electrons, photons, or ions as a probe beam striking the material to be analysed. This chapter reviews the fabrication of nanostructures using electrodeposition and various characterisation tools employed in the present study. 1-D magnetic nanostructures are synthesised using the electrodeposition and a Potentiostat/Galvanostat is employed for this. A description about the electrodeposition technique is provided at the beginning of this chapter. Analysis of various nanostructures are carried out using state of the art tools such as X-ray Diffraction (XRD), Scanning Electron Microscope (SEM), Transmission Electron Microscope (TEM), High-Resolution Transmission Electron Microscope (HRTEM), Selected Area Electron Diffraction (SAED), Energy Dispersive X-ray Spectroscopy (EDS), Raman analysis, Atomic Force Microscopy (AFM), Magnetic Force Microscopy (MFM), Fourier Transform Infrared Spectroscopy (FT-IR), Vibrating Sample Magnetometer (VSM), Superconducting Quantum Interference Device Magnetometer (SQUID Magnetometer), Thermo-Gravimetric analysis (TGA) and UV-Vis NIR spectrophotometer. This chapter also discusses the details of Zero Field Cooled-Field Cooled magnetisation studies and other thermomagnetisation studies.

2.1 Fabrication techniques and tools

2.1.1 Electrodeposition

Electrodeposition is the process by which a metal is deposited on a surface from a solution of its ions by means of passing an ac/dc current. The electrodeposition process can be divided into processes; nucleation and growth. Nucleation, which dominates very early stages, is a heterogeneous reaction of reducing ions into a smaller cluster forming a new phase on an electrode. Growth is the process of reducing ions on the existing nuclei, thereby expanding the new phase. The nuclei eventually overlap and form a film of the reduced metal on the substrate. If substrate used is a patterned one, the resulting deposit will also have a pattern of the substrate. The nucleation and growth reactions are important in determining the properties of the resulting films, especially those of thin films with thickness of the order of tens of nanometer.^[1]

Eventhough, electrodeposition is a relatively old science, how the deposit is initiated on the substrate during electrodeposition is not yet well understood. There are numerous theories on nucleation, with no clear consensus among researchers while studying the nucleation phenomena. There are several variables in the system, from the conditions of the surface and the electrolyte to the applied driving force.

Nucleation of a foreign material on to a substrate is assumed to take place on active sites. Electrocrystallisation is a specific case of phase formation and hence the steady state rate of heterogeneous nucleation can be described by the classical theory of nucleation, if the basic kinetic and thermodynamic parameters of the process are expressed in terms of the electrochemical quantities. Several theories of nucleation process exist which account for the time dependence of the number of nuclei growth. Fleischmann and Thirsk,^[2] Kaishev and Mutaftshiev,^[3] Markov and

Stoycheva^[4] and Fletcher and Lwin,^[5] are some of the significant ones among them. The Fleischmann and Thirsk model begins with the basic assumption that there are a fixed number of active sites, N_0 on the surface and it is independent of applied potential. This model predicts that at long times all of the active sites will be converted to nuclei. Modified Fleischmann and Thirsk model is applying by many researchers to fits the experimental data better. In most of these modifications, they allowed to vary the total number of active sites on the surface of the substrate with potential. The theory of Kaishev and Mutaftshiev, it was latter generalised by Markov and Kashchiev,^[6] is based on the assumption that different active sites on the surface have different critical over potentials for nucleation. A critical over potential is one below which an active site can not be nucleated. The Markov and Stoycheva is another model which combines the aspects of both the Fleishmann and Thirsk model and Kaishev and Mutaftshiev model. In this model, the saturation number of active sites, which is dependent on the overpotential, is identical to that described in the Kaishev and Mutaftshiev model. This model predicts the saturation of number of nuclei after a long time deposition. Fletcher and Lwin model is another model which discusses the nucleation during electrodeposition. It is based on the following assumptions;

1. The total number of active sites is a constant independent of over potential
2. All active sites experience the same overpotential for nucleation.
3. A random distribution of surface energies exists at the interface between crystal nuclei and active sites.

This model also agrees with Fleschmann and Thirsk model that after a long time of deposition, all the active sites will become nucleated.

Various growth mechanisms (some of them are numbered below as A, B, C) were also proposed for the continued growth of a metal deposit.^[7]

- A.
 - 1. Diffusion of ionic species through the solution directly to the location of lattice build up.
 - 2. Discharge of species at the sites where the lattice is to be built up.
 - 3. Lattice formation.
- B.
 - 1. Diffusion of ionic species through the solution to the surface.
 - 2. Charge transfer on the surface
 - 3. Diffusion of discharged species over the surface to sites where the lattice is built up.
 - 4. Lattice formation.
- C.
 - 1. Diffusion of ionic species through the solution to the surface.
 - 2. Diffusion of charged species over the surface to sites where the lattice is to be built up.
 - 3. Charge transfer and lattice formation.

Out of these mechanisms, C is considered to be most likely method of lattice growth and is proposed by Gerischer, Conway and Bockris.^[8-9]

2.1.2 Potentiostat

A potentiostat is the electronic hardware (Figure 2.1.a) required to control a three electrode cell (Figure 2.1.b) run most electroanalytical cells. The system functions by maintaining the potential of the working electrode at a constant level with respect to the reference electrode by adjusting the current at an auxiliary electrode. It consists of an electric circuit which are usually described in the form of simple op-amps.^[10]

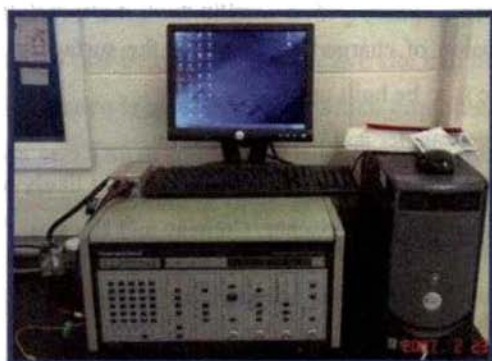
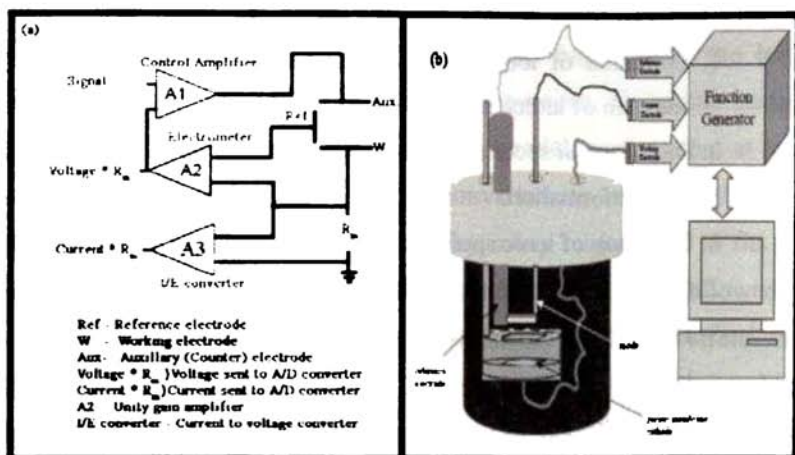


Figure 2.1: (a) Block diagram of a Potentiostat/Galvanostat system, (b) 3 electrode electrodeposition cell, (c) potentiostat used for the present study (273A).

In almost all applications, the potentiostat measures the current flow between the working electrode and auxiliary electrode. The controlled variable in a potentiostat is the cell potential and the measured variable is the cell current.

The main parts of a potentiostat are: working electrode, reference electrode, auxiliary electrode (counter electrode), electrometer and control

amplifier. A potentiostat can also be operated as a Galvanostat or as a Zero Resistance Ammeter (ZRA). Potentiostat will become a Galvanostat when the feedback is switched from the cell voltage signal to cell current signal (Figure 2.1.a).

Working electrode is the electrode where the potential is controlled and the current is measured. For many physical electrochemistry experiments the working electrode is an inert material such as gold, silver, platinum, or glassy carbon. The reference electrode is used in measuring the working electrode potential. A reference electrode should have a constant electrochemical potential as long as no current flows through it. The most common reference electrodes are saturated calomel electrode (SCE) and the silver/silver chloride (Ag/AgCl) electrode. The auxiliary electrode is a conductor that completes the cell circuit. The auxiliary electrode in the lab cells is generally an inert conductor like platinum or graphite. The current that flows in to the solution via working electrode leaves the solution via auxiliary electrode. Electrometer circuit measures the voltage difference between the reference and working electrode. Control amplifier measures the cell voltage with the desired voltage and drives current in to the cell to force the voltages to be the same.

Three electrode deposition has a definite edge over two electrode electrodeposition technique. Most of the voltammetry experiments, where the half cell reactivity of an electrolyte is investigated, use two electrodes (working electrode and auxiliary electrode) to conduct the experiment. The working electrode, which makes contact with the electrolyte, will apply the desired potential in a controlled way and facilitate the transfer of electrons to and from the electrolyte. A second electrode acts as the other half of the cell. This second electrode must have a known potential with which it measures the potential of the working electrode, furthermore it must balance the electrons added or removed by the working electrode. While this is a viable

setup, known as two electrode deposition has a number of shortcomings. Most significantly, it is extremely difficult for an electrode to maintain a constant potential while passing current to counter redox events at the working electrode. This can be solved by separating the role of supplying the electrons and referencing the potential in to two separate electrodes. The reference electrode is a half cell with a known reduction potential. Its only role is to act as reference in measuring and controlling the working electrodes potential and at no point does it pass any current. The auxiliary electrode passes all the current needed to balance the current observed at the working electrode. To achieve this current, the auxiliary will often swing to extreme potentials at the edges of the solvent window, where it oxidizes or reduces the solvent or supporting electrolyte. These electrodes, the working, reference, and auxiliary electrodes, constitute the modern three electrode system.

2.2 Analysis tools and techniques

2.2.1 X-ray diffraction studies (XRD)

X-ray diffraction patterns have been widely used in nanoparticle research as a primary characterisation technique for obtaining features like crystal structure, crystallite size, lattice constants and strain. Information about particle size distribution and mechanical stress can be inferred from the analysis of the width of the diffraction lines.

X-rays are high energy electromagnetic radiation having energies ranging from about 200eV to 1MeV. The three basic components of X-ray diffractometer are X-Ray source, specimen and X-ray detector. A thin layer of the sample powder is spread on a flat non diffracting glass slide and is exposed to the x-ray beam. If an element in the specimen has an atomic number slightly below that of the target metal, the X-rays will be strongly absorbed leading to decrease in intensity of the diffracted beam. The XRD

patterns of the samples were recorded on the X-ray diffractometer (Rigaku Dmax-C) using Cu K α radiation ($\lambda=1.5418 \text{ \AA}$), which has energy of 8.04keV.

In XRD a collimated beam of X-ray with a wavelength of 1.5418 \AA is incident on a specimen and is diffracted by the crystalline planes in the specimen according to the Bragg's law^[11]

$$n\lambda = 2d\sin\theta \quad 2.1$$

where λ is the wavelength of the X-radiation, n is an integer, d is the spacing between atomic planes in the crystalline planes and θ is known as diffraction angle. The intensity of the diffracted x-rays was measured and plotted as a function of diffraction angle 2θ . From the 2θ values of the peaks, the lattice spacing (d) values are calculated using the equation (2.1). *Lattice parameter* was calculated assuming cubic symmetry by employing the relation

$$d_{h,k,l} = \frac{a}{\sqrt{h^2 + k^2 + l^2}} \quad 2.2$$

The lattice parameter 'a' can be calculated from the equation

$$a = \frac{\lambda}{2\sin\theta} \sqrt{h^2 + k^2 + l^2} \quad 2.3$$

The *average particle size* was determined from the measured width of their diffraction curves by using Debye Scherrer's formula,^[12]

$$D = \frac{0.9\lambda}{\beta \cos\theta} \quad 2.4$$

Here λ is the wavelength of Cu K α radiation ($\lambda = 1.5418 \text{ \AA}$), β is the angular width which is equal to the full width half maximum.

The broadening of x-ray diffraction peaks can be obtained obtained with a diffractometer, and this information can be directly quantified.

However it is important to realize that the broadening of diffraction peaks arises mainly due to three factors

1. Instrumental effects: these effects include imperfect focusing, unresolved α_1 and α_2 peaks, or the finite widths of α_1 and α_2 peaks in cases where the peaks are resolved. These extraneous sources can cause broadening in the peak.
2. Crystallite size: the peaks become broader due to the effects of small crystallite sizes, and thus an analysis of the peak broadening can be used to determine the crystallite size from 100 to 500nm.
3. Lattice strain: lattice strain can also cause to the broadening of the diffraction peaks. If all the effects mentioned are simultaneously present in the specimen, the peaks will be very broad.

2.2.2 Scanning Electron Microscope (SEM)

The scanning electron microscope (SEM) is a type of electron microscope that images the sample surface by scanning it with a high-energy beam of electrons in a raster scan pattern. The electrons interact with the atoms that make up the sample producing signals that contain information about the sample's surface topography, composition and other properties such as electrical conductivity.^[13] There are many advantages for using the SEM instead of a light detector. The SEM has a large depth of field, which allows more of a specimen to be in focus at one time. The SEM also has much higher resolution, so closely spaced specimens can be magnified at much higher levels.

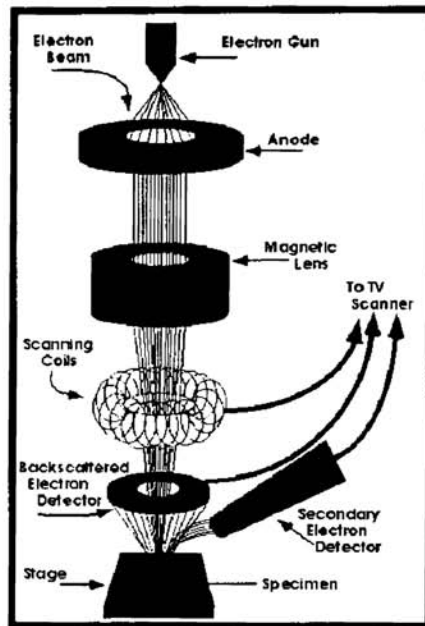


Figure 2.2: Schematic diagram of Scanning Electron Microscopy.

In Scanning Electron Microscopy, an electron beam with primary electron energy typically of 1-10keV is focused by a lens system into a spot of 1-10nm in diameter on the sample surface. The focused beam is scanned in a raster across the sample by a deflection coil system in synchronous with an electron beam of a video tube, which is used as an optical display. Both beams are controlled by the same scan generator and the magnification is just the size ratio of the display and scanned area on the sample surface. A variety of signals can be detected, including secondary electrons, backscattered electrons, x-rays, cathodoluminescence and sample current. The two dimensional map of the signal yields a SEM image. The main applications of SEM are in surface topography and elemental mapping. By appropriate choice of the detector, the signal of the electrons from a desired energy range can be monitored.^[14]

Field emission SEM (FESEM) is another type of SEM instrument where electrons are produced using the phenomenon of 'field emission'. There are three major types of electron sources: thermionic tungsten, LaB₆, and hot and cold field emission. In the first case, a tungsten filament is heated to allow electrons to be emitted via thermionic emission. Temperatures as high as 3000⁰C are required to produce a sufficiently bright source. These filaments are easy to work with but have to be replaced frequently because of evaporation. The material LaB₆ has a lower work function than tungsten and thus can be operated at lower temperatures, and it yields higher source brightness. However, LaB₆ filaments require much better vacuum than tungsten to achieve good stability and a longer lifetime. Recently, field emission electron sources have been produced. These tips are very sharp; the strong electric field created at the tip extracts electrons from the source even at low temperatures. In this case, the energy profile is sharper and less the effect of chromatic aberrations of the magnetic defocusing lenses. Although they are more difficult to work with, since they need very high vacuum and occasional cleaning and sharpening via thermal flashing, the enhanced resolution and low voltage applications of field emission tips are making them unique for high resolution scanning. ^[15]

2.2.3 Transmission Electron Microscopy (TEM)

Transmission Electron Microscopy is a straight forward technique to determine the size and shape of the nanostructured materials as well as to obtain structural information. In TEM, electrons are accelerated to 100KeV or higher projected on to a thin specimen by means of a condenser lens system, and penetrate in to the sample.^[13] TEM uses transmitted and diffracted electrons which generates a two dimensional projection of the sample. The principal contrast in this projection or image is provided by diffracted electrons. In bright field images the transmitted electrons generate

bright regions while the diffracted electrons produce dark regions. In dark field image the diffracted electrons preferentially form the image. In TEM, one can switch between imaging the sample and viewing its diffraction pattern by changing the strength of the intermediate lens. The greatest advantage that TEM offers are the high magnification ranging from 50 to 10^6 and its ability to provide both image and diffraction information from a single sample.

The high magnification or resolution of TEM is given by

$$L = \frac{h}{\sqrt{2mqV}} \quad 2.5$$

where m and q are the electron mass and charge, h the Planck's constant and V is the potential difference through which the electrons are accelerated.

The schematic of a transmission electron microscope is shown in figure 2.3.

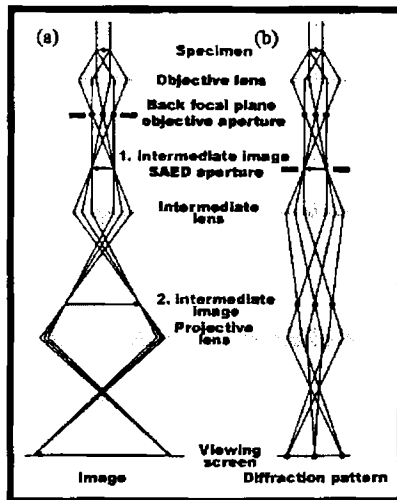


Figure 2.3: Transmission Electron Microscope for imaging and Selected Area Diffraction Pattern (Reproduced from Ref.[16])

Typically a TEM consists of three stages of lensing. The stages are the objective lenses, intermediate lenses and the projector lenses. The objective lens forms a diffraction pattern in the back focal plane with electrons scattered by the sample and combines them to generate an image in the image plane (1. intermediate image). Thus diffraction pattern and image are simultaneously present in the TEM. It depends on the intermediate lens which appears in the plane of the second intermediate image and magnified by the projective lens on the viewing screen. Switching from a real space to a reciprocal space (diffraction pattern) is easily achieved by changing the strength of the intermediate lens. In imaging mode, an objective aperture can be inserted in the back focal plane to select one or more beams that contribute to the final image (Bright field (BF), Dark field (DF), High Resolution TEM (HRTEM)). The BF image is formed by effectively cutting out all the diffracted beams, leaving out only transmitted beam to form the image. The bright field image is bright only in areas that have crystalline planes that are tilted such that they do not satisfy the Bragg condition. The DF image will be obtained on the other hand if the transmitted beams are blocked instead of diffracted beams.

2.2.4 High-Resolution TEM

High resolution transmission electron microscope (HRTEM)^[17] can generate lattice images of the crystalline material allowing the direct characterisation of the samples atomic structure. The resolution of the HRTEM is 1 nm or smaller. However, the most difficult aspect of the TEM technique is the preparation of samples. High-resolution TEM is made possible by using a large-diameter objective diaphragm that admits not only the transmitted beam, but at least one diffracted beam as well. All of the beams passed by the objective aperture are then made to recombine in the image-forming process, in such a way that their amplitudes and phases are preserved. When

viewed at high-magnification, it is possible to see contrast in the image in the form of periodic fringes. These fringes represent direct resolution of the Bragg diffracting planes; the contrast is referred to as *phase* contrast. The fringes that are visible in the high-resolution image originate from those planes that are oriented as Bragg reflecting planes and that possess interplanar spacings greater than the lateral spatial resolution limits of the instrument.

2.2.5 Selected Area Electron Diffraction Pattern (SAED)

Selected area diffraction offers a unique capability to determine the crystal structure of individual nanomaterials and the crystal structure of the different parts of a sample. A small area of the specimen can be selected from a high resolution transmission image and its electron diffraction pattern (rings or spots) produced on the screen of the microscope by making appropriate arrangement in the lenses of TEM. This is an optional arrangement in HRTEM. The arrangement for taking the diffraction pattern is shown in figure 2.3.b. The SAED allows the researcher to determine lattice constant of the crystalline material which can help in species identification. Basically diffraction patterns are distinguishable as spot patterns resulting from single crystal diffraction zones or ring patterns are obtained from the randomly oriented crystal aggregates (polycrystallites). For nanocrystallites, the diffraction patterns will be a diffused ring patterns. The ' d ' spacing between lattice planes can be estimated radius r of the diffracted rings from the relation $\lambda L = rd$, if the camera constant λL is known. The estimation of d values enable us to describe the crystal structure of the crystalline specimen.^[18-19]

2.2.6 Energy Dispersive X-ray Spectroscopy (EDS)

Energy dispersive X-ray spectrometer (EDS) attached to the transmission electron microscope analyses characteristic X-ray radiation emitted from the specimen when the electron beam interact with the specimen. The main use of EDS is to accurately determine the composition of the sample under investigation. Upon exposing the samples to high energy electron beams the various atoms present in the sample emit characteristic X-rays which can be observed as several distinct peaks on an energy scale. The intensities of the peaks can be compared with the peaks of a standard sample to obtain the relative amounts of each atomic species, whereby accurate composition of the sample can be determined. The use of EDS has been demonstrated in oxide nanoparticle research in a number of reports.^[20-21]

2.2.7. Atomic Force Microscopy

The successful achievements of scanning tunneling microscopy have inspired the development of a set of novel scanning probe microscopy methods such as AFM, MFM, LFM etc. These techniques are based on the usage of piezoelectric transducers that provide the ability to control the spatial position of probing tip relative to the sample surface with great accuracy and thus to map the measured surface property on an atomic or nanometer scale. Among such methods, Atomic Force Microscopy has found the widest application.

The Atomic Force Microscopy was invented by Binnig, Quate, and Gerber in 1986. AFM senses the forces between the tip and the sample.^[14] This microscope can image surfaces with atomic resolution by scanning a sharp tip across the surface at forces smaller than the forces between atoms. A commercially available silicon tip was used in all studies.^[22]

The principle of AFM operation is illustrated in the following figure 2.4.

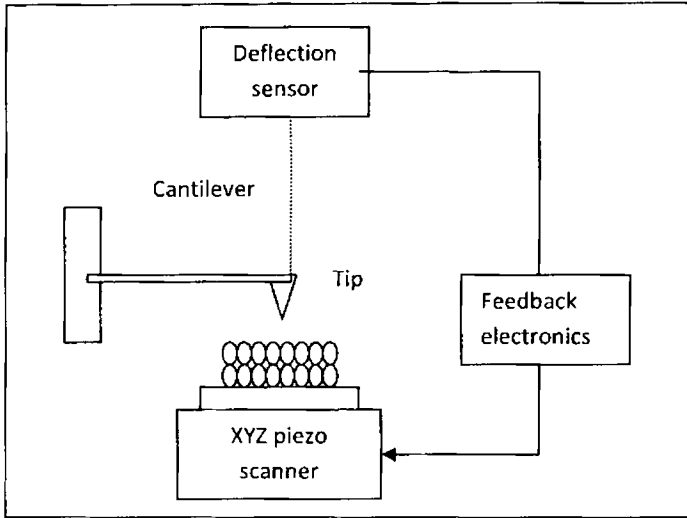


Figure 2.4: Schematic illustration of AFM operation.

The cantilever with the attached stylus is sandwiched between the AFM sample and the tunnelling tip. It is fixed to a small piezoelectric element called the modulating piezo which is used to drive the cantilever beam at its resonant frequency. The interatomic forces between the tip and the sample surface atoms cause the cantilever to deflect. The AFM sample is connected to a three dimensional piezoelectric drive i.e, the x,y,z scanner .A feedback loop is used to keep the force acting on the stylus at a constant level. The cantilever displacement is measured by a deflection sensor. Typically sensors can detect deflections as small as 10^{-2} Å. Measuring the deflection of the cantilever while the tip is scanned over the sample allows the surface topography to be mapped.^[14, 23]

The evident advantage of AFM is that it is applicable for studying all types of surfaces, conducting, semiconducting and insulating. STM is generally applicable only to conducting samples.

Tapping mode AFM is of particular interest in determining topography and phase morphology of films. In tapping mode, the silicon probe tip oscillates at its resonance frequency as it rasters across the sample surface, experiencing only intermittent contact with the surface. Tapping mode does not provide atomic resolution but appears to be advantageous for imaging rough surfaces with topographical corrugation. Three Types of Tapping Mode Data are follows:

Height Data: The vertical position of the probe tip is monitored by noting changes in the length of the z-axis on the xyz scanning piezo tube. Input voltage to the scanning piezo tube is proportional to the length of the tube. The change in the z-axis is plotted as a topographical map of the sample surface. Height data is a good measure of the height of surface features but does not show distinct edges of these features.

Phase Data: This type of imaging monitors the change in phase offset, or phase angle, of the input drive signal [to the drive piezo] with respect to the phase offset of the oscillating cantilever. The phase of the drive signal (i) is compared to the phase of the cantilever response signal (ii) on the photo diode detector. The phase offset between the two signals is defined as zero for the cantilever oscillating freely in air. As the probe tip engages the sample surface, the phase offset of the oscillating cantilever changes by some angle with respect to the phase offset of the input drive signal. As regions of differing elasticity are encountered on the sample surface, the phase angle between the two signals changes. These changes in phase offset are due to differing amounts of damping experienced by the probe tip as it rasters across the sample surface. These differences are plotted as the so-called 'phase image'.

Amplitude Data: The amplitude of the cantilever is monitored by the photo diode detector. The RMS value of the laser signal on the y-axis of the detector is recorded for each of the 512 segments on a given raster of the

probe tip. These values are plotted as an amplitude map of the sample surface. Amplitude images tend to show edges of surface features well. ^[8]

2.2.8 Magnetic Force Microscopy (MFM)

A magnetic force microscope is actually derived from Atomic Force Microscopy. Here, unlike in the case of AFM, a magnetic tip is used for study and thus it can probe the magnetic interaction between tip and magnetic materials. MFM normally works in non-contact mode. The MFM senses the stray magnetic field above the surface of a sample. A magnetic tip (usually magnetic materials, such as Co/Fe or magnetic alloys, coated silicon tip) is brought into close proximity with the surface and a small cantilever is used to detect the force between the tip and the sample. The tip is scanned over the surface to reveal the magnetic domain structure of the sample at up to 50 nm resolution.

2.2.9 Raman Spectroscopy

Raman spectroscopy is used to identify different molecules and even functional groups within larger molecules. The bonds formed between atoms have specific vibrational frequencies that correspond to the atom's masses and the strength of the bond between them. Complex molecules therefore exhibit many peaks and can be readily identified by the pattern or "fingerprint" created by those peaks. As such, there are many uses for micro Raman spectrometers as they can non-destructively identify microscopic samples or microscopic areas of larger samples. When an intense monochromatic light beam impinges on the sample, the electric field of the incident radiation distorts the electron clouds that make up the chemical bonds in the sample, storing some energy. When the field reverses as the wave passes, the distorted electron clouds relax and the stored energy is reradiated. Although, the incident beam may be polarized so that the electric

field is oriented in a specific direction with respect to the sample, the scattered beam is reradiated in all directions, making possible a variety of scattering geometries. Most of the stored energy is reradiated at the same frequency as that of the incident exciting light. This component is known as the Rayleigh scattering and gives a strong central line in the scattering spectrum. However, a small portion of the stored energy is transferred to the sample itself, exciting the vibrational modes. The vibrational energies are deducted from the energy of the incident beam and weak side bands appear in the spectrum at frequencies less than that of the incident beam. These are the Raman lines. Their separation from the Rayleigh line is a direct measure of the vibrational frequencies of the sample.^[15]

2.2.10 Fourier Transform Infrared Spectroscopy

FTIR spectroscopy is a technique that provides information about the chemical bonding or molecular structure of materials, whether organic or inorganic. It is used to identify unknown materials present in a specimen. The technique works on the fact that bonds and groups of bonds vibrate at characteristic frequencies. A molecule that is exposed to infrared rays absorbs infrared energy at frequencies which are characteristic of that molecule. During FTIR analysis, a spot on the specimen is subjected to a modulated IR beam. The specimen's transmittance and reflectance of the infrared rays at different frequencies is translated into an IR absorption plot consisting of reverse peaks. The resulting FTIR spectral pattern is then analyzed and matched with known signatures of identified materials in the FTIR library. FTIR spectroscopy does not require a vacuum, since neither oxygen nor nitrogen absorbs infrared rays. FTIR analysis can be applied to minute quantities of materials, whether solid, liquid, or gaseous. When the library of FTIR spectral patterns does not provide an acceptable match, individual peaks in the FTIR plot may be used to yield partial information

about the specimen. Schematic diagram of a Fourier transform infra red spectrometer is shown in the figure 2.5.

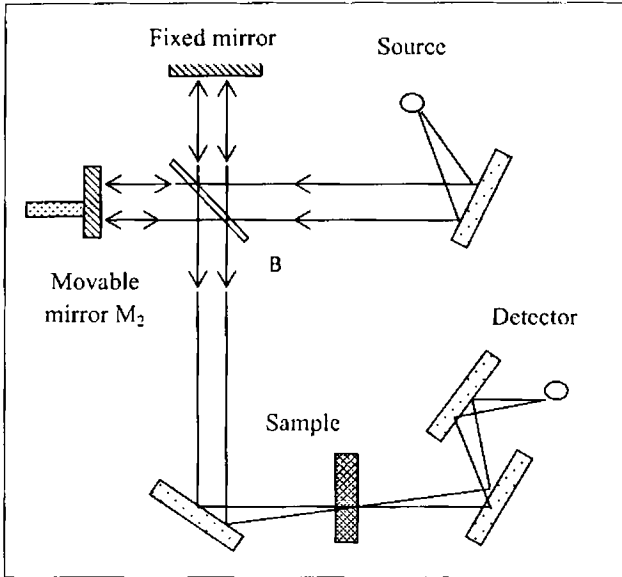


Figure 2.5: Schematic diagram of a Fourier transform infra red spectrometer.

A parallel beam of radiation is directed from the source to the interferometer, consisting of a beam splitter B and two mirrors M_1 and M_2 . The beam splitter is plate of suitably transparent material coated so as to reflect 50% of the radiation falling on it. Thus half of the radiation goes to M_1 and half to M_2 , returns from both these mirrors along the same path and is then recombined to a single beam at the beam splitter. If a monochromatic radiation is emitted by the source, the recombined beam leaving B shows constructive or destructive interference depending on the relative path lengths B to M_1 and B to M_2 . As the mirror M_2 is moved smoothly towards or away from B, therefore, a detector sees radiation alternating in intensity.

The production of spectrum is a two stage process. Firstly, without the sample in the beam, mirror M_2 is moved smoothly over a period of time. Through a distance of about 1 cm, while the detector signal – the interferogram is collected into the multichannel computer; the computer carries out the Fourier transformation of the stored data to produce the background spectrum. Secondly a sample interferogram is recorded in exactly the same way. Fourier transformed and then ratioed against the background spectrum for plotting as a transmittance spectrum. Alternatively the sample and background spectra may each be calculated in absorbance forms and the latter simply subtracted from the former.^[24]

2.2.11 UV-Visible Spectroscopy

Ultraviolet-visible spectroscopy or ultraviolet-visible spectrophotometry involves the spectroscopy of photons in the UV - Visible region. It uses light in the visible and adjacent near ultraviolet and near infrared ranges. In this region of the electromagnetic spectrum, molecules undergo electronic transitions. The instrument used in ultraviolet-visible spectroscopy is called a UV/Vis spectrophotometer. It measures the intensity of light passing through a sample (I), and compares it to the intensity of light before it passes through the sample (I_0). The ratio I / I_0 is called the transmittance, and is usually expressed as a percentage (%T). The absorbance A is based on the transmittance,^[25]

$$A = -\log(\%T)$$

2.6

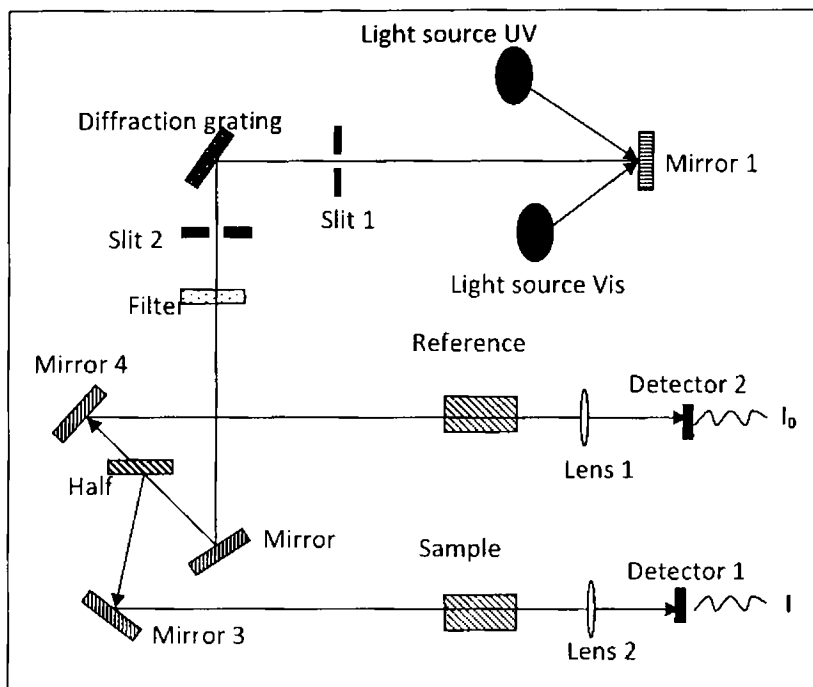


Figure 2.6: Schematic diagram of UV-Visible spectroscopy.

A diagram of the components of a typical spectrometer is shown in the following diagram 2.6. The functioning of this instrument is relatively straightforward. A beam of light from a visible and/or UV light source is separated into its component wavelengths by a prism or diffraction grating. Each monochromatic (single wavelength) beam in turn is split into two equal intensity beams by a half-mirrored device. One beam, the sample beam, passes through a small transparent container (cuvette) containing a solution of the compound being studied in a transparent solvent. The other beam, the reference, passes through an identical cuvette containing only the solvent. The intensities of these light beams are then measured by electronic detectors and compared. The intensity of the reference beam, which should

have suffered little or no light absorption, is defined as I_0 . The intensity of the sample beam is defined as I . Over a short period of time, the spectrometer automatically scans all the component wavelengths in the manner described. The ultraviolet (UV) region scanned is normally from 200 to 400 nm, and the visible portion is from 400 to 800 nm.

The absorption coefficient is calculated from the spectrum by dividing the αd (fluence) value by the thickness (d) of the sample and it is plotted against the photon energy. The intercept of this plot on the photon energy axis gives the band gap of the material. The probable energies for the transitions were estimated from the Tauc plot by plotting the $(\alpha hv)^{1/2}$ vs. hv graphs.

2.2.12 Thermo-Gravimetric Analysis (TGA)

The thermal properties like heat capacities, the glass transition temperature, melting and degradation of macromolecules can be analysed using thermogravimetry and differential thermal analysis along with differential scanning calorimetry (DSC). Thermal measurements are based on the measurement of dynamic relationship between temperature and some property of a system such as mass, heat of reaction or volume when the material is subjected to a controlled temperature programme.

In thermo-gravimetric analysis, the mass of the sample is recorded continuously as a function of temperature as it is heated or cooled at a controlled rate. A plot of mass as a function of temperature, known as thermogram, provides both quantitative and qualitative information. The apparatus required for thermo-gravimetric analysis include a sensitive recording analytical balance, a furnace, a temperature controller, and a programmer that provides a plot of the mass as a function of temperature. Often an auxiliary equipment to provide an inert atmosphere for the sample is also needed. Changes in the mass of the sample occurs as a result of

rapture and/or formation of various physical and chemical bonds at elevated temperature that led to the evolution of volatile products or formation of reaction products. Thus TGA curve provides information regarding the thermodynamics and kinetics of various chemical reactions, reaction mechanisms, and intermediate and final reaction products.

2.2.13 Magnetisation studies

This section discusses the important tools used for the magnetisation studies in the present investigation. At the end, various magnetisation measurement schemes such as zero field cool, field cool and M(T) studies are also discussed.

2.2.13.1 Vibrating Sample Magnetometer (VSM)

A vibrating sample magnetometer (VSM) operates on Faraday's Law of induction, which tells us that a changing magnetic field will produce an electric field. This electric field can be measured and provides us information about the changing magnetic field. A VSM is used to measure the magnetic behaviour of magnetic materials. Using VSM the hysteresis loop parameters namely saturation magnetisation (M_s), coercive field (H_c), remanence (M_r) and squareness ratio (M_r/M_s) can be derived. The schematic of a vibrating sample magnetometer is given in figure 2.7.

In a VSM, the sample to be studied is placed in a constant magnetic field. If the sample is magnetic, this constant magnetic field will magnetize the sample by aligning the magnetic domains or the individual magnetic spins, with the field. The stronger the constant field, the larger the magnetisation. The magnetic dipole moment of the sample will create a magnetic field around the sample, sometimes called the magnetic stray field. As the sample is moved up and down, this magnetic stray field change as a function of time and can be sensed by a set of pick up coils. A transducer

converts a sinusoidal ac drive signal provided by a circuit located in the console in to a sinusoidal vertical vibration of the sample rod and the sample is thus made to undergo a sinusoidal motion in a uniform magnetic field. Coils mounted on the pole pieces of the magnet pick up the signal resulting from the sample motion.

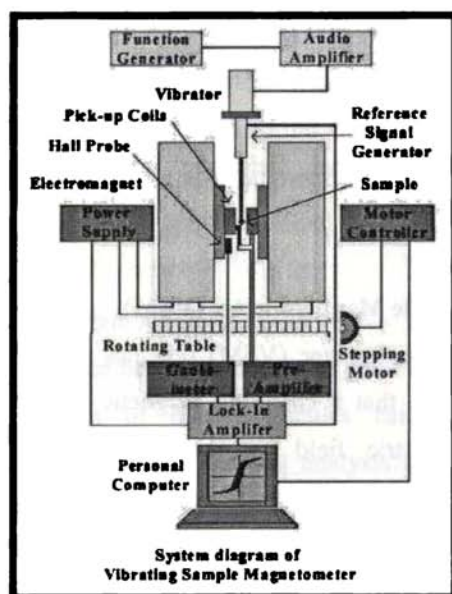


Figure 2.7: Vibrating Sample Magnetometer

The alternating magnetic field will cause an electric field in the pick up coil as according to Faradays law of induction, the current will be proportional to the magnetisation of the sample. The greater the magnetisation, the greater the induced current. The induction current is amplified by a trans-impedance amplifier and a lock-in amplifier. The various components are interfaced via a computer. Controlling and monitoring software, the system can tell you how much the sample is magnetized and how magnetisation depends on the strength of the constant

magnetic field. For particular field strength, the corresponding signal received from the probe is translated into a value of magnetic moment of the sample. When the constant field varies over a given range, a plot of magnetisation versus magnetic field strength is generated.

A dipole moment is induced in the sample when it is placed in a uniform magnetic field be M . Then the amount of magnetic flux linked to the coil placed in the vicinity of this magnetic field is given by

$$\phi = \mu_0 n \alpha M \quad 2.7$$

where ' μ_0 ' is the permeability of free space, ' n ' the number of turns per unit length of coil and α represents the geometric moment decided by position of moment with respect to coil as well as shape of coil.

Anharmonic oscillator of the type,

$$Z = Z_0 + A \exp(j\alpha z) \quad 2.8$$

induces an emf in the stationary detection coil. The induced emf is given by

$$V = -\frac{d\phi}{dt} = -j\omega\mu_0 nMA \left(\frac{\partial\alpha}{\partial z}\right) e^{j\omega z} \quad 2.9$$

If amplitude of vibration (A), frequency ω and $\frac{\partial\alpha}{\partial z}$ are constant over the sample zone then induced voltage is proportional to the magnetic moment of the sample. A cryogenic setup attached to the sample permits low temperature measurements. This is the basic idea behind VSM.³⁰⁻³²

2.2.13.2 SQUID Magnetometer

SQUID magnetometer is the instrument used to measure extremely sensitive magnetic fields of the order of 10^{-14} T. The superconducting quantum interference device (SQUID) consists of two superconductors separated by thin insulating layers to form two parallel Josephson junctions. The great sensitivity of the SQUID devices is associated with measuring changes in

magnetic field associated with one flux quantum ($h/2e$). The basic principle that follows in a SQUID magnetometer is that, if a constant biasing current is maintained in the SQUID device, the measured voltage oscillates with the changes in phase at the two junctions, which depends upon the change in the magnetic flux. Counting the oscillations allows to evaluate the flux change which has occurred. Hence, when the sample is moved through the superconducting magnetic coils, a flux change is induced in the pick up coils. Highly magnetic sample should be moved slowly through the coils in order not to exceed the maximum slewing rate of the electronic system.^[26]

2.2.13.3 Field Cooled and Zero Field Cooled Measurements

Various magnetic interactions are competing in a system of nanoparticles. Magnetisation memory and relaxation measurements are the unique methods to probe these magnetic interactions. Zero field cooled (ZFC) and Field cooled (FC) measurements provide a means of investigating the effects of the various magnetic interactions. In a ZFC measurement, sample is cooled to liquid helium temperatures under zero applied magnetic fields. Then small uniform external field is applied and the net magnetisation is measured while heating the sample at a constant rate. For small magnetic particles, this curve has a characteristic shape. As the particle cools in a zero applied magnetic field, they will tend to magnetise along the preferred crystal directions in the lattice, thus minimizing the magneto-crystalline energy. Since the orientation of each crystallite varies, the net moment of the systems will be zero. Even when a small external field is applied the moments will remain locked into the preferred crystal directions, as seen in the low temperature portion of the ZFC curve. As the temperature increases more thermal energy is available to disturb the system. Therefore more moments will align with the external field direction in order to minimize the Zeeman energy term. In other words, thermal vibration is providing the activation energy required for the Zeeman

interaction. Eventually the net moment of the system reaches a maximum where the greatest population of moments has aligned with the external field. The peak temperature is called blocking temperature T_B which depends on particle volume, (In principle, the maximum moment obtained from the ac susceptibility at negligibly small fields is the actual blocking temperature. From the dc measurements, if the FC/ZFC curves deviate below the maximum in ZFC, then the maximum can be taken as the blocking temperature). As temperature rises above T_B , thermal vibrations become strong enough to overcome the Zeeman interaction and thus randomize the moments.^[27-28]

Field cooled measurements proceed in a similar manner to ZFC except that the constant external field (a small magnetic field which lies in the initial permeability region) is applied while cooling and heating. The net moment is usually measured while heating. However, the FC curve will diverge from the ZFC curve at a point near the blocking temperature. This divergence occurs because the spins from each particle will tend to align with the easy crystalline axis that is closest to the applied field direction and remain frozen in that direction at low temperature. Thermal Remnant Magnetisation (TRM) curves are obtained by cooling in field to the measurement start temperature. The field is then removed and the magnetisation is recorded as a function of temperature while the sample is heated. It is important to note that ZFC, FC and TRM are non equilibrium measurements.^[29,31] The rate of heating and cooling are important in all these measurements. These DC magnetisation measurements determine the equilibrium value of magnetisations in the samples.

References

1. Arthur, W. A. A Text book of Physical Chemistry (1979) Academic Press, 2nd Edition, New York.
2. Fleischmann, M.; Thrisk, H. R. *Electrochim. Acta* (1960) 2 22.
3. Kaishev, R.; Mutaftshiev, B. *Electrochim. Acta* (1965) 10 643.
4. Markov, I.; Stoycheva, E. *Thin solid films* (1972) 35 21.
5. Fletcher, S.; Lwin, T. *Electrochim. Acta* (1983) 28 237.
6. Markov, I.; Kashchiev, D. J. *Crystal Growth* (1972) 16 170.
7. Fleischmann, M.; Thrisk, H. R. *Advances in electrochemistry and electrochemical engineering*, (1963) 3 123 Edited by Delahay P.; Tobias, C. W. Wiley, New York.
8. Gerisher, H. *Elektrochem.* (1958) 62 256.
9. Conway, B. E.; Bockris, J. O. M. *Electrochim. Acta* (1961) 3, 340.
10. Bard, A.J.; Faulkner, L.R. *Electrochemical Methods: Fundamentals and Applications*. (2000) New York: John Wiley & Sons, 2nd Edition.
11. Kittel, C. *Introduction to solid state physics* (1997) John-Wiley & Sons New York.
12. Cullity, B. D. *Elements of x-ray diffraction* (1978) Addison-Wesley Publ. company, Inc. 2nd California.
13. Watt, M. *The principle and practise of electron microscopy* (1997) Cambridge Uni. Press, Cambridge.
14. Oura, K.; Lifshits, V. G.; Saranin, A. A. ; Zotov, A. V. ; Katayama, M. *Surface science, an introduction* (2003) Springer-Verlag Berlin Heidelberg, Germany.
15. Brundle, C. R.; Evans, C. A. Wilson, S. *Encyclopedia of materials characterisation* (1992) Reed Publishing, USA.
16. <http://www.microscopy.TEMED.htm> (12/05/2009).
17. Subramanian, A.; Marles, L. D. *Ultramicroscopy* (2004) 98 151.
18. Schamp, C. T.; Jesser, W. A. *Ultramicroscopy* (2005) 103 165.
19. Murr, L. E. *Electron and ion microscopy and microanalysis, principles and applications* Mc-Graw Hill Inc. New York (1982).
20. Lin, C. H.; Kuo, P. C.; Pan, J. L.; Huang, D. R.; *J. Appl. Phys.* (1996) 79 6035.
21. Xu, X.; Freidman, G.; Humfield, K. D.; Majetich, S. A.; Acher, *Chem. Mater.* (2002) 14 1249.

22. Jamshid, K.; Avlyanor, Jack, Y.; Josefowicz,, MacDirmid, A. G. *Synthetic Metals* (1995) 73 (3) 205.
23. Binning, G.; Quate, C. F.; Gerber, C. *Phy. Rev. Lett.* (1986) 56 (9) 930.
24. Banwell, C. N.; McCash, E. M. *Fundamentals of molecular spectroscopy* (1994) Tata McGraw Hill 4th Edition.
25. Pankov J.J *Optical Processes in Semiconductors* (1971) Printice-Hall, New Jersey, USA.
26. K. Gramm, L. Lundgren, Beckman, *Physica Scripta.* (1976) 13, 93.
27. Denardin, J. C.; Brandle, A. L.; Knobel, M.; Panissod, P.; Palchomov, A. B.; Liu, H.; Zhang, X. X. *Phys. Reb B* (2002) 65 0644221.
28. Michele, O.; Hesse, J.; Bremers, H.; Polychroniadis, E. K.; Efthimiadis, K. G.; Ahlers, J. *Phys.: Condens. Matter* (2004) 16 427.
29. Roy, A.; Srinivas, V.; Ram, S.; Toro, J. A. D. *J. Appl. Phys.* (2006) 100 094307.
30. Dormann, J. L.; Fiorani, J. *Magn. Magn. Mater.* (1995) 415 140.
31. Battle, X.; Labarta, A. *J. Phys. D: Appl. Phys.* (2002) 35 R15 (Topical Review).

Chapter 3

Fabrication of Magnetic Nanostructures of Nickel and Cobalt and Elucidation of Mechanism of Growth

Magnetic nanowires and nanotubes are ideal materials for the fabrication of various multifunctional nanostructures which can be manipulated by means of an external magnetic field. This chapter discusses the fabrication, structural, morphological and magnetic properties of Nickel and Cobalt nanowires and nanotubes. A plausible growth mechanism, mobility assisted growth mechanism, has been suggested for the growth of one-dimensional nanostructures during potentiostatic electrodeposition inside porous alumina membrane. The veracity of the mobility assisted growth mechanism has been tested using various precursors. The template assisted synthesis has been extended to synthesize hybrid structures of Ni and Co, a new system called Ni @ Co nanorods. The interesting magnetic features observed in these one dimensional nanostructures are elaborately discussed in this chapter.

**A part of the work discussed in this chapter has been reported in*

- 1. "J. Phys. Chem. C" (2008, 112, 14281)*
- 2. "Nano Research" (2008, 1, 465)*
- 3. "Nanoscale Res. Lett." (2009, Accepted)*

3.1 Introduction

Design and control of nanowire and nanotube growth with limited degree of complexity will surely impact the development of nanotechnology.^[1] Soon after the discovery of carbon nanotubes by Iijima,^[2] nanotube based materials received sufficient attention from the scientific community because of their extensive application potential in nanodevices and sensors.^[3] Nanohole arrays having uniform size and shape have been identified as potential materials for fabricating various functional nanodevices.^[4-7] Tubular structures offer multitudes of opportunities because they can be used as pipes, microcavities, or microcapsules. Nanoholes, for example, with large surface area, can successfully replace the low purity nanoparticles that are prepared using more sophisticated techniques for various applications such as catalysis, sensor technology, high density magnetic storage, and delivery vehicles.^[8-9]

Inorganic nanotubes have also attained considerable attention during the last few years due to their diverse utilities in racemic mixtures, sensors, selective separation or selective ion transportation.⁸ However, literature on non-carbon nanotubes is limited as compared to their carbon counterparts.^[10-14] Among the non carbon cousins, much interest has been devoted to metal nanotubes and nanowires. Several techniques are reported for the synthesis of metal nanotubes. This include chemical routes such as chemical reduction of metallic complexes and chemical vapour infiltration within porous templates such as AAO or polymer nanochannels.^[14,9,10,15] There are also reports where in nanotubes and nanowires have been synthesized using highly sophisticated techniques like pulsed laser deposition or molecular beam epitaxy.^[16-17]

Magnetism is a cooperative phenomenon and is dictated by size, dimension, shape, structure and morphology of the constituent phases along with the type and strength of the magnetic coupling that exists among the

constituent phases.^[18-20] Nanoscaled magnetic materials have been receiving much attention, due to their unique magnetic properties that are different from their bulk counter parts and are promising candidates for various applications. One dimensional structures-nanowires, nanotubes and nanorods provide an ideal platform for exploring properties like magnetisation reversal and shape anisotropy.^[21] Ferromagnetic nanowires and nanotubes of Fe, Co and Ni are candidate materials for studying fundamental phenomena like micromagnetic reversal process and quantum size effects.^[22-23] Ferromagnetic nanowires and nanotubes have innumerable applications in areas such as ultrahigh density recording,^[24-25] GMR sensors,^[26] supermolecular architectures^[27] and nanoscale electronic and optoelectronic devices.^[28-29] Moreover, control of morphology in nanostructures is very vital in tailoring their properties.^[30]

Deposition of metals inside nanometric pores of membranes is the most inexpensive technique to produce nanosized patterned structures. The template assisted synthesis is developing in to an elegant chemical approach for the fabrication of nanoscale structures, as an alternative to sophisticated lithographical methods,^[31] especially for larger areas. Here, the template assisted electrodeposition is receiving much attention for the fabrication of magnetic nanostructures because of its low cost, simplicity of operation, and the ability to tailor magnetic properties by tuning the length and diameter of the porous material. Aligned wires obtained via electrodeposition are likely to replace today's unstructured magnetic media with tera bit per square inch capacity. These nanowires are promising candidates for nanoscopic electrodes in applied electrochemistry^[32-33] and for various other fundamental studies.^[34-36]

The high ordering and the magnetic nature of the wires will induce outstanding cooperative phenomenon that differ from the bulk and even from their thin film counterparts. Among these ordered magnetic wires, the

interwire interactions play an important role and have been the subject of extensive investigations.^[37-40] It has been reported that these interwire interactions are so strong that they can even change the easy axis of magnetisation and control the magnetisation reversal depending upon the strength of the interaction.^[21-23] A complete understanding of the mechanism of magnetisation reversal in such systems remains elusive and is a challenge to researchers. Rivas et al.^[38] reported the change of easy axis of Cobalt nanowires depending up on the magnetostatic interaction among them and Escrig et al.^[37] studied the geometry dependence of coercivity in nickel nanowires. These studies indicate that the modes of magnetisation reversal and other magnetic properties in such systems are strongly influenced by the microstructure and the interwire separation between nanowires. A complete understanding of the mechanism of magnetisation reversal in such systems remains elusive and it is persisting as a challenge for researchers.

Ferromagnetic nanotubes based on Ni, Fe and Co are being investigated in great detail due to their application potential in diverse fields such as perpendicular magnetic recording, cell separation, diagnosis, therapeutics and magnetic resonance imaging for detection. The ease with which they can be functionalized using specific group is an added advantage of these nanostructures and can be used for drug targeting and other applications in biotechnology.^[41-42] However, not much literature exists as regard the utilization of magnetic nanotubes in medicine. A survey of literature reveals that a systematic method of preparation of nanotubes and elucidation of growth mechanism is largely elusive.^[3,43]

Electrodeposition over nanoporous membrane is a simple, low cost and an ingenious technique for the preparation of one dimensional structure with high purity. The ability of this technique to tune the material properties by controlling the length and diameter makes it promising for nanoscale

material fabrication as an alternative to more expensive techniques such as Molecular Beam Epitaxy and micro lithography.^[44]

Most of the reports on the synthesis of magnetic nanotubes are by chemical modification of inner surface of the porous template prior to the deposition.^[4,9,10,15,17] However, these techniques result in low yield and impure structures. Moreover, the mechanism leading to the formation of nanostructures from nanoporous template is seldom elucidated which is very essential for tailoring the properties of these nanostructures.^[3]

Hybrid magnetic nanostructures with high coercivity have immense application potential in various fields. Metallic magnetic nanotubes/wires of Ni, Co and Fe and also their alloys such as FePt, CoPt, NiFe, NiZn, CoCu and FeB were investigated in great detail due to their application potential in diverse fields such as perpendicular recording, cell separation, diagnosis, therapeutics, and magnetic resonance imaging.^[45-49] Controlled synthesis of smart nanostructures based on magnetic materials assumes important due to their potential applications in various fields and the possibility for manipulating these structures using an external magnetic field.^[50] The Co-Ni system is special due to the capability of tuning the magnetic properties such as coercivity, by varying the Co content.^[46] Several groups have reported the synthesis of various magnetic alloys using template assisted electrodeposition^[45-48] and they have achieved this by mixing the electrolyte precursors in different compositional ratio. The lacuna of such techniques is the unpredictability in the magnetic properties such as coercivity of the resultant one dimensional structures after electrodeposition. Co-axial hybrid magnetic structures synthesized via two step electrodeposition technique can surpass this problem by controlling the deposition of one of the components. Preparation and characterisation of such hybrid structures is the main motive of this study presented through this chapter.

3.2. Experimental

Alumina membranes (AAO template, Whatman) of high purity (99.9%) and uniform pore density, with average pore diameter ~ 150 nm and thickness $\sim 60\mu\text{m}$, were employed for electrodeposition. Figure 3.1 shows the FESEM and AFM image (top view) of AAO template employed for electrodeposition.

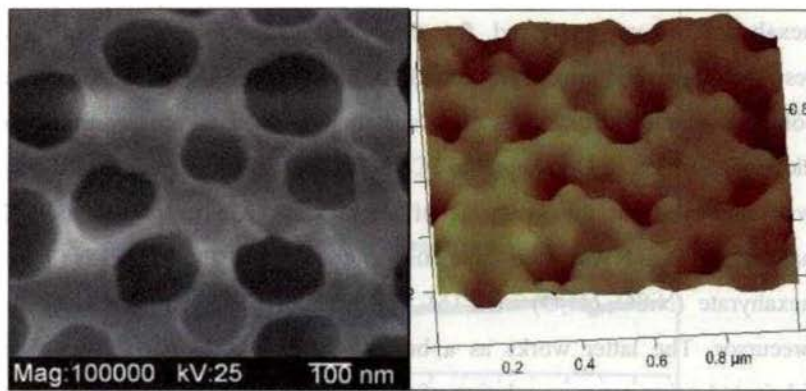


Figure 3.1: (a) FESEM image, (b) AFM image of AAO template used for electrodeposition.

The FESEM and AFM images are well correlated and both confirm the uniform distribution of pores and average pore size is found to be ~ 150 nm. The three electrode potentiostatic electrodeposition (as explained in Chapter 2) was carried out by employing metal coated AAO template as working electrode. Initially, a layer of Ag (about 200nm thickness) was thermally evaporated onto one side of the AAO template which acted as the working electrode for the electrochemical deposition. The electrodeposition was carried out on the nanopores, using a standard three electrode potentiostat system (Princeton EG & G 273 A). Ag/AgCl was the reference electrode and platinum was used as the counter electrode. It is noteworthy

that using this process the length of the metal nanotube can be controlled by varying the time of deposition.

Various metal salt solutions were employed as precursors for electrodeposition. The electrodeposition was standardised at a constant voltage of -1V. Different precursors like Cobalt acetate, Cobalt acetate tetrahydrate, Cobalt sulphate heptahydrate were used for the electrodeposition of Cobalt where as Nickel Sulphate and Nickel sulphate hexahydrate were employed for the electrodeposition of Nickel. The resultant nanostructures were found to highly depend on the precursor solutions employed. 0.2 M Cobalt acetate was used as the precursor for electrodeposition of Co nanotubes (Co NTs) and Cobalt acetate tetrahydrate was employed for the synthesis of thick walled Co nanotubes. For Ni nanowires (Ni NWs), the aqueous solution of 0.2M nickel sulphate hexahydrate ($\text{NiSO}_4 \cdot 6\text{H}_2\text{O}$) in 0.1M Boric acid (H_3BO_3) was used as the precursor. The latter works as a buffer. Co nanowires (Co NWs) were fabricated using aqueous solution of 0.2M $\text{CoSO}_4 \cdot 7\text{H}_2\text{O}$ in 0.1M Boric acid (H_3BO_3). Once the electrodeposition was over, AAO was dissolved using 3M Sodium hydroxide (NaOH) [alkaline treatment].

X ray powder diffraction pattern of nanotubes was recorded using Cu K α radiation, $\lambda=1.5418\text{\AA}$ (Rigaku Dmax-C). The morphology of the nanotubes after removing the template was studied by Field Emission Scanning Electron Microscope (SEM), JSM-6335 FESEM. Room temperature and low temperature magnetic properties of these nanotubes were investigated using a SQUID magnetometer (MPMS-5S XL Quantum Design). Surface morphology and the magnetic phases were identified using an Atomic Force Microscopy/Magnetic Force Microscopy (AFM/MFM) (Nanoscope Digital Instruments). Transmission Electron Microscopy (TEM) experiments were performed using JEM 2010 Transmission Electron Microscope.

3.3. Results and Discussion

3.3.1 Nickel Nanowires and Tubes

The growth rate of Ni NWs synthesised using Nickel sulphate hexahydrate was studied at each hour and it was found that a 5 hour electrodeposition results in high aspect ratio Ni NWs of average length 50 μm and diameter ~ 150 nm.

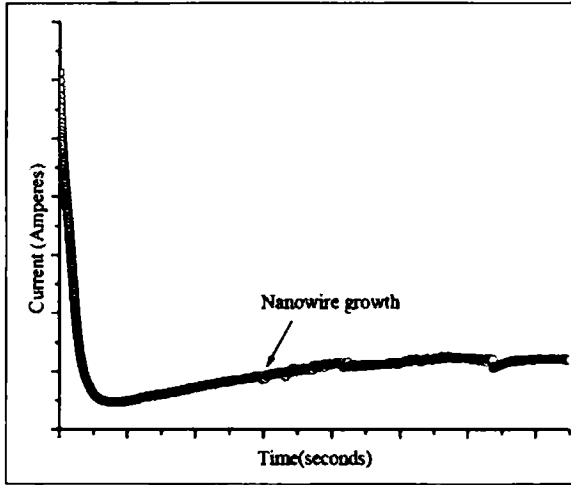


Figure 3.2: Electrodeposition curve of Ni NWs.

Figure 3.2 shows a typical electrodeposition curve exhibiting the time dependence of electrical current during electrodeposition for Ni NWs. The horizontal part of the current transient indicates the production of nanowires in the pores of the alumina membrane. Current variation also shows that there is no over-deposition and the nanowire is in the growth state.^[51]

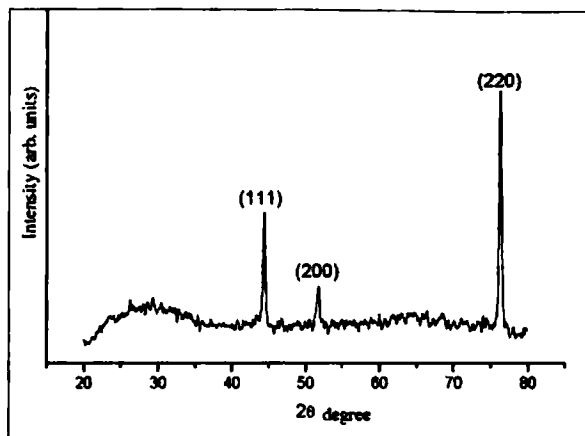


Figure 3.3: XRD patter of Ni NWs inside AAO template.

XRD pattern of Ni NWs (Figure 3.3) indicates that the wires are highly crystalline (polycrystalline) in nature and they crystallize in the face centred cubic phase. Preferential growth along (220) can also be noticed from the XRD pattern. It must be noted here that the broad diffraction occurring around $15-35^{\circ}$ is due to amorphous alumina.^[52]

The high relative intensity ratio of 220 and 111 diffraction lines in the case of Ni NWs is an evidence for strong texturing along $\langle 110 \rangle$ direction.^[53]

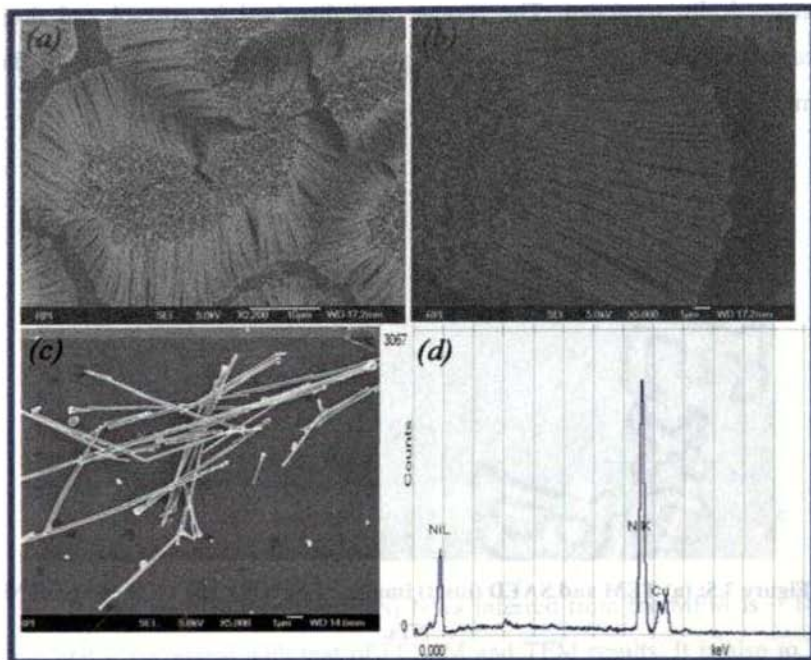


Figure 3.4: (a), (b), (c) FESEM images of Ni NWs, (d) EDS of Ni NWs.

FESEM images (Figure 3.4. a, b and c) indicate the formation of good quality nanowires with a maximum length of $50\mu\text{m}$ and diameter of 150 nm . Figure 3a and Figure 3b depict the bundles of Ni NWs after the separation of AAO template by alkaline treatment. Figure 3c shows individual Ni NWs on a silicon substrate. Figure 3d is the EDS of Ni NWs after removing the AAO template. The purity of Ni NWs is verified using EDS and it is to be noted that there is no other elemental impurities. The peak corresponding to Cu ($\sim 15\%$ of Ni) arises from the Cu tape used for EDS measurements.

TEM and SAED images of Ni NWs are shown in Figure 3.5.a. It must be noted here that the samples were subjected to TEM studies after removing the template (alumina) using 3M NaOH and the residue was

magnetically separated. The residue was dissolved in ethanol and drop casted over copper grid. The quality of the nanowire is evident from the micrograph.

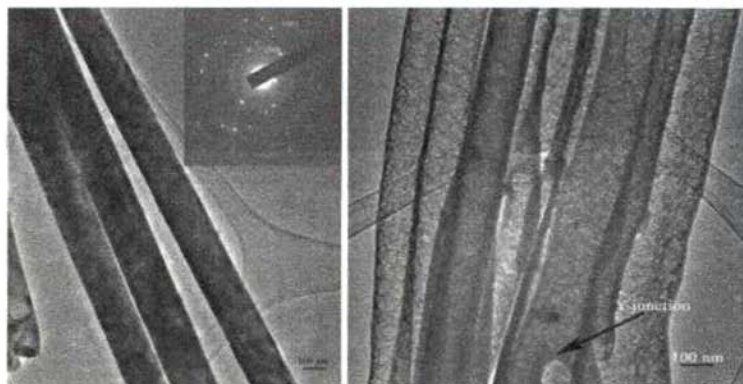


Figure 3.5: (a) TEM and SAED (inset) images of Ni NWs, (b) TEM image of Ni NTs.

The SAED patterns (Figure 3.5.a, inset) indicate that the nanowires are crystalline in nature. The marked (200) and (311) planes corresponds to that of Ni.

Nickel nanotubes (Ni NTs) have been obtained after electrodeposition by replacing the precursor with Nickel sulphate (NiSO_4). Figure 3.5.b depicts the TEM image of Ni NTs. A Y-junction formed in the Ni NTs may be due to the defect already present in the AAO template (voltage variation during the synthesis of AAO template leads to various hierarchical branched structures).^[1,54]

The nanowires within the alumina template were subjected to morphological studies using AFM/MFM. Figure 3.6 shows the AFM and MFM images of bulk Ni NWs.

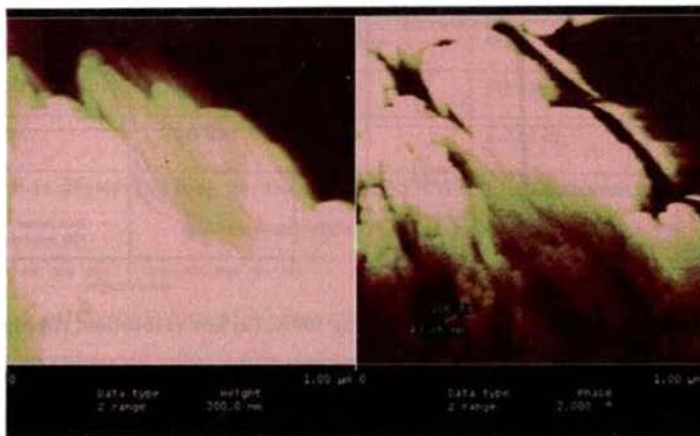


Figure 3.6: AFM-MFM images of Ni NWs along with the AAO template.

The average diameter of Ni NWs inferred from the MFM is ~ 160 nm and is correlated with that of FESEM and TEM results. It is also to be noted from the MFM image that the electrodeposited Ni NWs exhibit the “skyscraper” phenomenon associated with the lack of length uniformity and control. This can be removed by selective etching of the surface using concentrated acids.^[27]

3.3.2.1 Magnetisation studies on Ni Nanowires

Magnetisation measurements (M-H measurements) were carried out using a SQUID magnetometer. SQUID measurements were carried out by keeping the nanowires inside AAO template so as to keep their alignment intact. Magnetisation studies of Ni NWs show features similar to that of Nickel nanotubes^[55], but the length of the nanowire for the present study is much higher and hence exhibit a high shape anisotropy. The M-H curves at 300K and 6K are shown in Figure 3.7 (7a and 7b) and Figure 8 respectively.

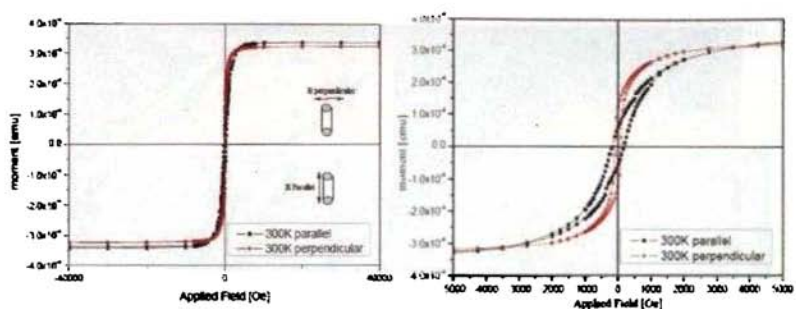


Figure 3.7: M-H curves of Ni NWs at 300K, (a) low resolution, (b) high resolution.

Figure 3.7.b represents the rescaled and expanded view of Figure 3.7.a, representing the in- and out- of plane coercivity differences.

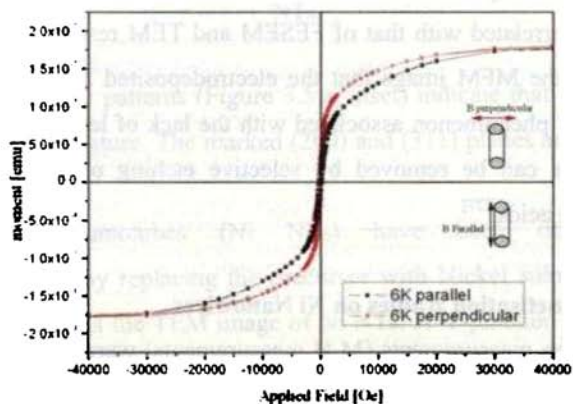


Figure 3.8: M-H curve of Ni NWs at 6K.

The loop parameters are evaluated and are exhibited in Table.1.

Temperature	Field Parallel		Field perpendicular	
	H _c	M _r /M _s	H _c	M _r /M _s
300 K	180 Oe	0.2	90 Oe	0.36
6 K	260 Oe	0.1	220 Oe	0.2

Table 3.1: Hysteresis loop parameters for Ni NWs at two different geometries and two different temperatures.

Coercivity values of Ni nanowires (H_c parallel and H_c perpendicular) exhibit an enhanced value compared to the bulk Ni (around 0.7 Oe for Ni^[55-56]). The coercivity values reported for Nickel nanowires of similar diameters is ~220Oe for longitudinal fields with a squareness value of 0.8.^[57] The squareness obtained for parallel field is much less than the reported values for Nickel nanowire. It has long been known that aligning nanoparticles gives rise to magnetic anisotropy, that is, a squarer hysteresis loop for a magnetic field applied parallel to the direction of the alignment than for a magnetic field applied perpendicular to this direction. This behavior is predicted by the Stoner-Wohlfarth model or more recent calculations and verified experimentally by a large number of studies.^[58-63]

The Crystal anisotropy K₁ of Ni NW is ~ 4×10⁴ erg/cm³ and shape anisotropy is $\pi M_s^2 = 7 \times 10^5$ erg/cm³. Due to this large shape anisotropy and high aspect ratio (~330), the easy magnetisation direction always lies along the wire axis. Moreover, for an fcc lattice the anisotropy orientation is pointing along the (110) direction. Therefore, from XRD and magnetisation measurements it is to be concluded that anisotropy axis is aligned along the wire axis and it adds up to the shape anisotropy. So the easy axis is parallel to the wire axis. Reported measurements on isoradial Ni NWs are on polycarbonate membranes or single crystal mica films where the typical pore

density is $10^{-2}\mu\text{m}^{-2}$.^[31] In the case of alumina template (used for the present study) the pore density lies in the range of 10^2 - $10^3\mu\text{m}^{-2}$.

Figure 3.9 indicates that the inter pore distance in the alumina template is $\sim 100\text{nm}$.

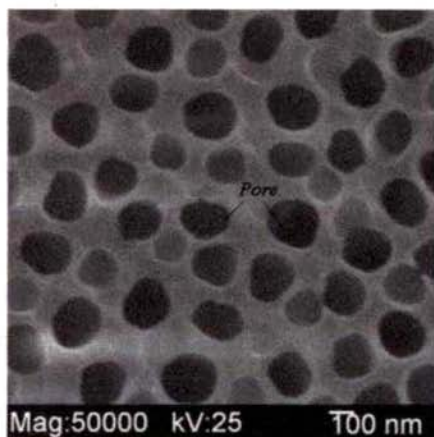


Figure 3.9: FESEM image of AAO template indicating the inter-pore distance.

The high pore density in the case of alumina results in high interwire interaction which induces a dipolar field due to the adjacent wire interaction. This dipolar field will act as the demagnetization field, which is given by $\Delta H = -\Delta N M$, where ΔN is the demagnetization factor and M is the magnetisation. The low M_r/M_s , observed in the case of parallel field, where it is expected to be ~ 1 , is due to this high interwire interaction. Both the magnetisation curves are highly sheared due to this demagnetization field indicating strong interwire interaction, which is expected because the average separation between the nanowires is $\sim 100\text{ nm}$. The alumina template is unable to mediate exchange interactions over more than a few interatomic distances, so the interaction between the wires is realized only through magnetostatic dipolar interactions.^[64]

The effect of high dipolar interaction for perpendicular fields is to reduce the saturating field. Saturating field for perpendicular field is $H_{L5}=7\text{Koe}$ whereas that of parallel field is $H_{H5}=10\text{Koe}$. M-H curve recorded at 6K exhibits an increase in coercivity and decrease in remanence parallel to the nanowire axis, consistent with an enhanced contribution of cubic magnetocrystalline anisotropy which is in competition with the uniaxial shape anisotropy.^[65] Shape anisotropy is identical at low and high temperature measurements, because of the large length to diameter ratio (~ 330).^[66] Figure 3.10 shows the $M(T)$ measurement at 20Koe parallel to the nanowire. In this measurement the sample is cooled in zero field to low temperature (5K). Then a field of 20Koe is applied parallel to the wire and the $M(T)$ curve has been measured by warming up the sample in this field.

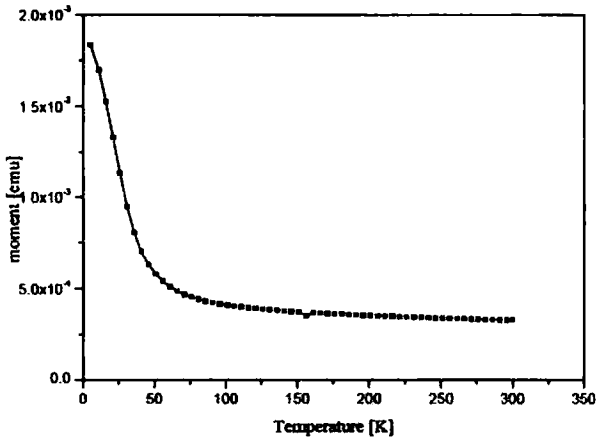


Figure 3.10: M-T curve of Ni NWs at 20Koe.

Such a study enables one to compare the thermal demagnetization process with field induced reversal process at low temperatures. $M(T)$ curves show a switching of magnetisation from a high magnetisation value to a lower one (\sim one order change in magnetisation value) at a temperature \sim

20K during warming. Since the sample is ferromagnetic both at low and room temperatures as inferred from M-H curves, this cooperative switching can only result because of surface spin disorder. Since there are no indications of any oxide layer formation as evident from the XRD (Figure 3.3), the chance of surface spin disorder resulting from antiferromagnetic interaction of nickel oxide is ruled out. The only possibility for such a switching of magnetisation in the parallel field measurement can be because of the dipolar interaction between adjacent nanowires. This helps to align the spin antiferromagnetically between adjacent wires. Magnetisation switching in terms of shape anisotropy is questionable and will not be complete in the case of wires where an interwire magnetostatic interaction exists. In the case of strong interwire interaction, the individual wires switches cooperatively and it is more or like the magnetisation switching happens in a thin film.^[67] M-T curve in Figure 3.10 depicts such a cooperative switching and hence this type of unusual M-T curve also proclaims the presence of strong interwire magnetostatic interactions in Ni.

3.3.2 Cobalt Nanowires and Tubes

X ray Diffraction (Rigaku Dmax-C) pattern (Figure 3.11.a) of cobalt nanotubes (Co NTs, synthesized using Cobalt acetate) indicate the formation of polycrystalline pure cobalt hexagonal close packed phase (space group:p63/mmc). Broad features appearing in the 15-35° 2 θ range arise from the amorphous alumina. This is in agreement with the earlier reports.^[52]

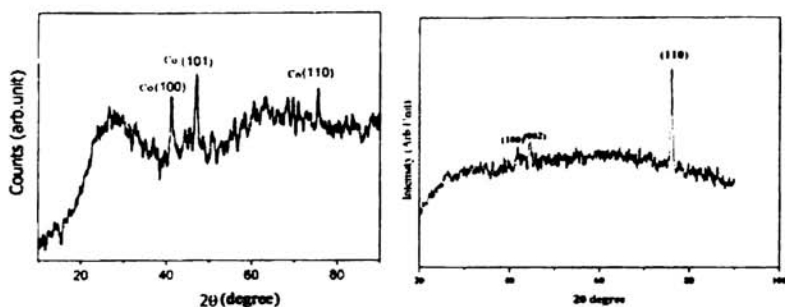


Figure 3.11: XRD Pattern of (a) Cobalt NTs and, (b) Co NWs, with alumina template.

Figure 3.11.b. shows the XRD pattern of Cobalt nanowires (Co NWs, synthesized using cobalt sulphate heptahydrate). The formation of highly crystalline (polycrystalline) and textured Co hcp phase is evident from the XRD. The FESEM images of Cobalt nanotubes, after removal of supporting alumina template by alkaline treatment, are depicted in Figure 3.12. Figure 3.13 shows the TEM image of Cobalt nanotubes and Figure 3.14, the Energy Dispersive Spectrum (EDS) of Co NTs which confirms the presence of Cobalt in cobalt nanotubes and also establishes the absence of other elemental impurities.

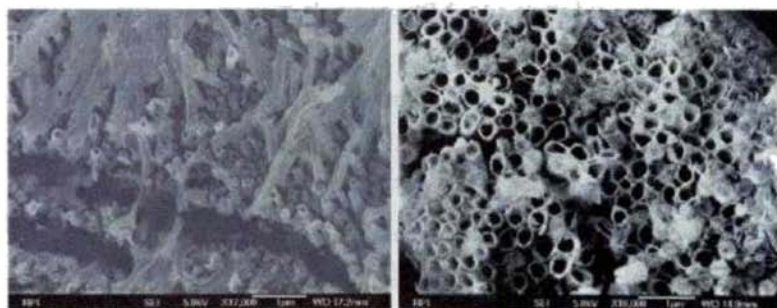


Figure 3.12: FESEM images of Cobalt nanotubes, (a) 1hr electrodeposition (b) Top view of 5hr deposited nanotube.

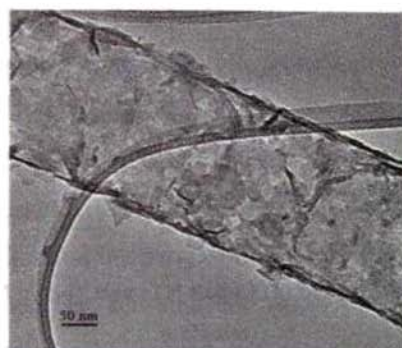


Figure 3.13: TEM image of Co NT.

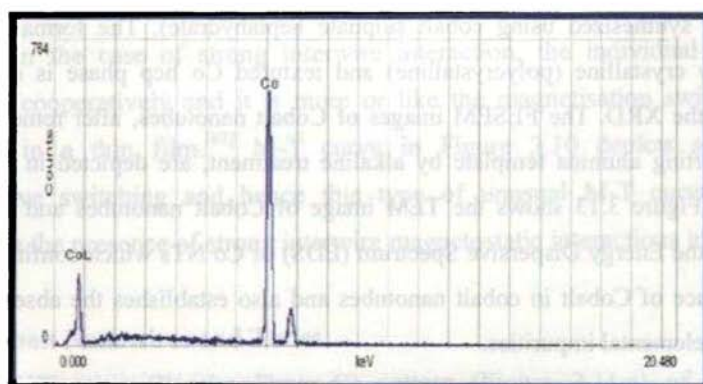


Figure 3.14: EDS of Cobalt nanotube.

The absence of other impurities in the nanotubes is further confirmed by FT-IR (Figure 3.15.a) and Micro Raman analysis (at an excitation wavelength of 514.5nm, Figure 3.15.b). The FT-IR and Raman analysis were carried out after etching the AAO template using NaOH (alkaline treatment). The FT-IR peaks corresponding to 630 and 1385 cm^{-1} can be assigned to Metal-Hydroxide bond and $-\text{OH}$ in plane bending

vibration.^[68] The metal hydroxide group may arise during the alkaline treatment and subsequent rinsing using deionised water.

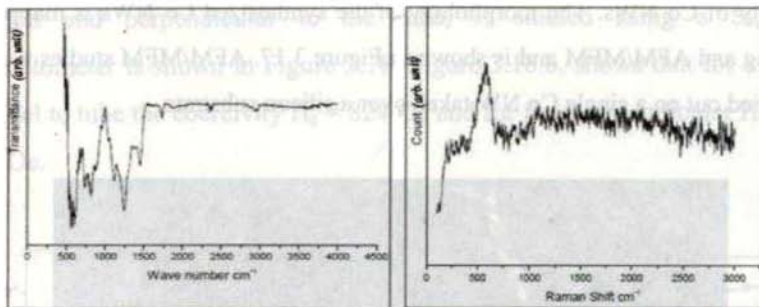


Figure 3.15: (a) FT-IR, (b) Microraman analysis of Co nanotube (After etching out the alumina template with NaOH).

Moreover, the peak corresponding to $\sim 550 \text{ cm}^{-1}$ in the Raman spectrum (Figure 3.15.b) can also be assigned to that of Cobalt hydroxide, formed during the etching process. The FESEM image of Co NWs (synthesized using Cobalt sulphate heptahydrate) is shown in Figure 3.16.a.

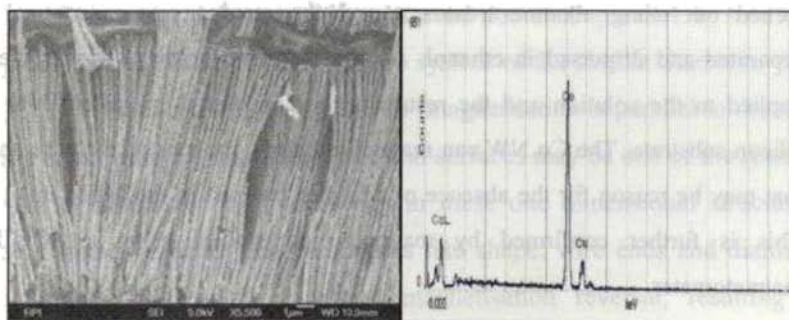


Figure 3.16: (a) FESEM image, (b) EDS of Co NWs.

The electrodeposition was carried out for a time period of 5 hours and the resultant nanowires have found to be having an average length of $50\mu\text{m}$. The EDS of Co NWs is shown in Figure 3.16.b. This confirms the purity of Co NWs. The morphology of the synthesized Co NWs is mapped using AFM/MFM and is shown in Figure 3.17. AFM/MFM studies were carried out on a single Co NW taken over a silicon substrate.

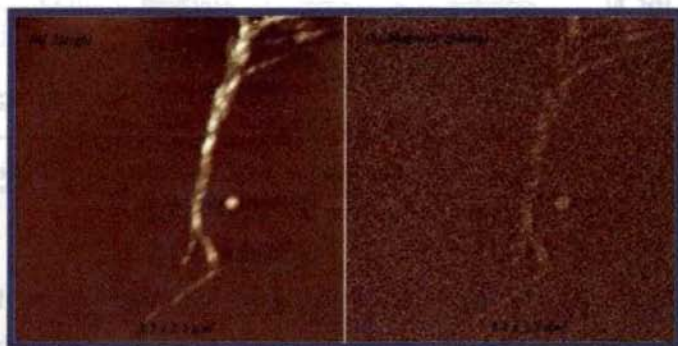


Figure 3.17: AFM, MFM images of a single Co NW over a silicon substrate.

The sample has been prepared as follows; the AAO template is etched out using alkaline treatment and the residue was magnetically separated and dispersed in ethanol. A high magnetic field ($\sim 1\text{T}$) was then applied to the solution and the resultant solution was drop casted over a silicon substrate. The Co NW can be magnetised along the axis of the wire and that may be the reason for the absence of a higher contrast in the MFM image. This is further confirmed by magnetisation studies using a SQUID magnetometer.

3.3.2.2 Magnetisation studies on Co nanotubes

Magnetic hysteresis loops, which display the magnetic response of a magnetic sample to an external applied magnetic field, have been used to

characterize the nanostructured materials. SQUID measurements are carried out by keeping the nanotubes inside AAO template so as to keep their alignment intact. Room temperature $M(H)$ behaviours for both fields parallel and perpendicular to the tube, is studied using a SQUID magnetometer is shown in Figure 3.18. Figure 3.18.b. shows that for a field parallel to tube the coercivity $H_c = 824$ Oe and for field perpendicular H_c is ~ 123 Oe.

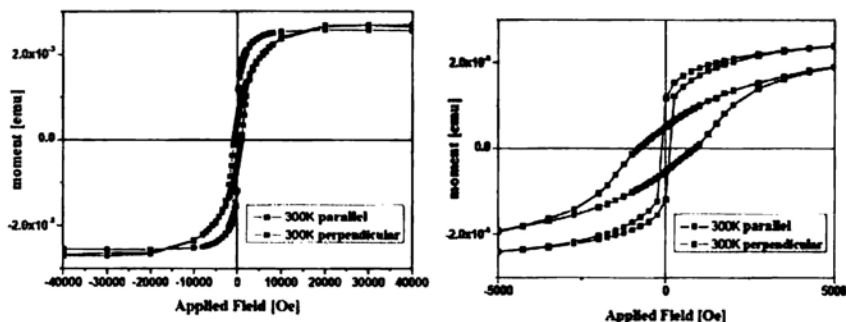


Figure 3.18: Room Temperature M-H curve of Co NTs.

This very high coercivity observed for field parallel to the tube (highest reported value for Cobalt wire system of the similar diameter ~ 150 nm)^[10,42,64,69] indicates that easy axis of magnetisation is parallel to the tube axis. Perfect ordering and defect free end surfaces may be one of the reasons for the exhibition of high coercivity in these one dimensional structures. Recent studies indicate that parameters like shape, wire ends and diameter fluctuations will lead to localized magnetisation reversal, resulting in reduction of coercivity.^[70] Eventhough the magnetisation is parallel to the tube, squareness (M_r/M_s) is less compared to the M_r/M_s value obtained with field perpendicular to the tube and hence a higher anisotropy results along the tube. This is due to the high inter-tubular interaction where the inter-tubular separation is ~ 100 nm. Since alumina template is not able to mediate

exchange interactions over more than a few inter-atomic distances, the interaction between the tubes are predominantly magnetostatic dipole interactions.^[71] The magnetic field produced by a dipole at a distance, x in a direction perpendicular to the dipole is given by the relation,

$$H_x = \frac{m}{(x^2 - \frac{l^2}{4})^{3/2}} \quad 3.1$$

where m is the magnetic moment and l is the length of the dipole. So this field, effectively acts as the demagnetizing field and will become an important factor when the intertubular distance is of the same order of tubular diameter. The magnetostatic interaction between larger nanometer tubes or wires, which are closely packed in an alumina template, is more important than smaller ones.^[72] The main effect of wire or tube interaction is to decrease the saturation field for perpendicular fields,^[73] and this effectively reduces the anisotropy. Figure 3.19 shows the M-H behaviour of Co NTs for the field perpendicular to the nanotube.

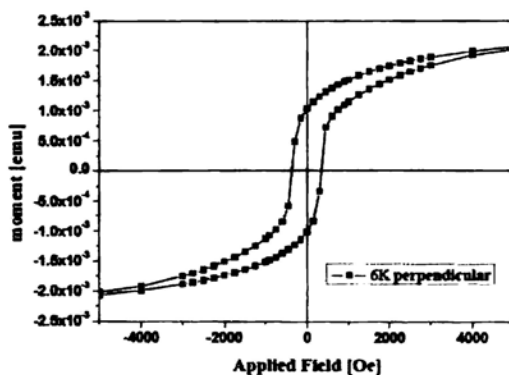


Figure 3.19: M-H curve of Co NTs at 6K.

The enhancement of H_c at low temperature ($H_c \sim 3450\text{Oe}$) is consistent with the monotonic increase of uniaxial anisotropy constant with

decreasing temperature, with the basic assumption that the shape anisotropy is independent of temperature for high aspect ratio tubes.²²

3.3.2.3 Magnetisation studies on Co nanowires

The SQUID magnetisation studies were carried out on Co NWs and are shown in Figure 3.20.

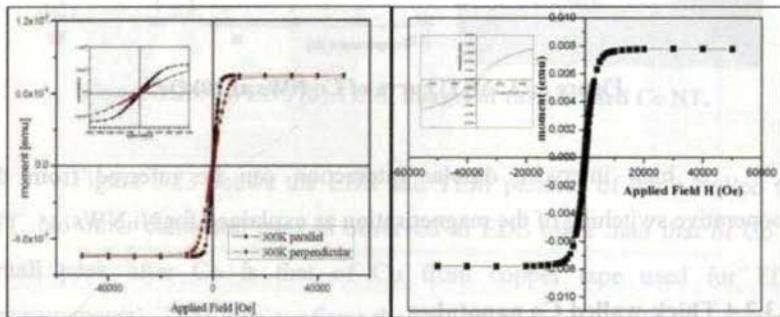


Figure 3.20: M-H curves of Co NWs, (a) at 300 K, (b) at 6K.

Room temperature (300K) and low temperature (6K) magnetic properties of Co NWs are depicted in Figure 3.20.a and 3.20.b respectively. The loops (parallel and perpendicular) are highly sheared and both exhibit a very low M_r/M_s (~ 0.1). This is perhaps due to the high interwire interaction. Room temperature coercivity values of Ni NWs and Co NWs are by and large comparable. As in the case of Ni NWs, low temperature coercivity of Co NWs exhibit an enhanced value ($H_{c\parallel} \sim 290$ Oe) because of higher magnetocrystalline anisotropy by these materials at low temperatures. A high field $M(T)$ measurement were also performed on Co NWs in the same way as done for Ni NWs and is depicted in Figure 3.21.

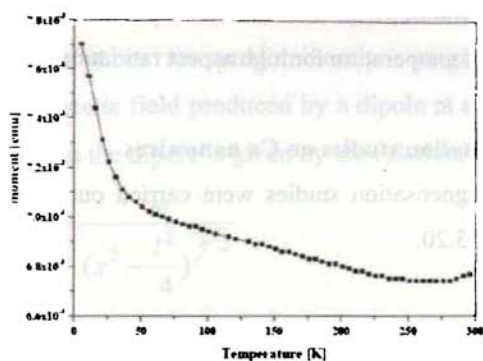


Figure 3.21: M(T) curve of Co NWs at 20kOe.

A high interwire dipolar interaction can be inferred from the cooperative switching of the magnetisation as explained for Ni NWs.

3.3.2.4 Thick-walled Co nanotubes

Thick-walled nanotubes (some of them are completely filled as wires) of Cobalt were obtained when the precursor was replaced by an aqueous solution of Cobalt acetate tetrahydrate. Parameters like pH, molarity and field gradient are kept constant for both depositions (cobalt acetate and cobalt acetate tetrahydrate). Figure 3.22.a. and 22.b. show the FESEM images (side view and top view) of thick-walled cobalt nanotubes.

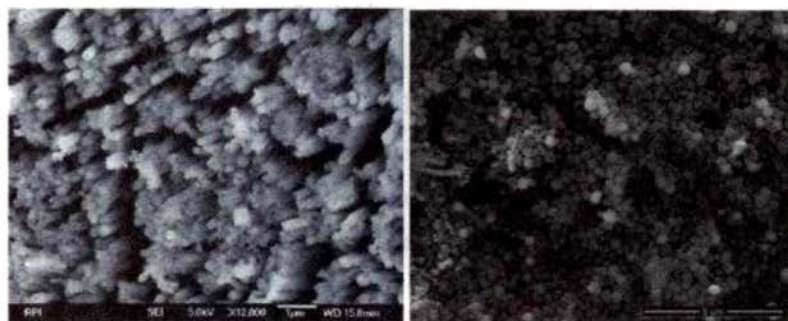


Figure 3.22: FESEM images of thick walled Co NTs (a) side view, (b) top view.

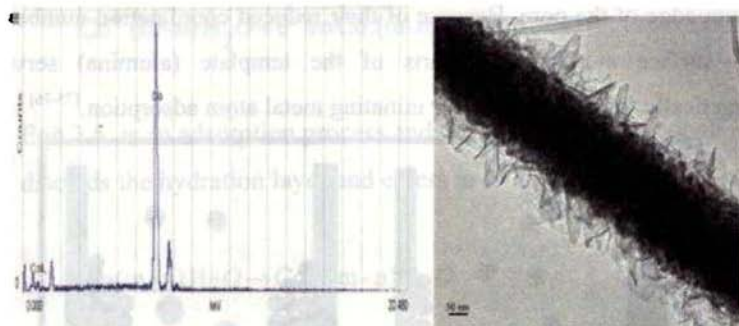


Figure 3.23: (a) EDS (b) TEM, images of thick walled Co NT.

Figure 3.23 shows the EDS and TEM pictures of thick walled Co NT. No other elemental peak is observed in EDS other than that of Co (a small peak after Co is that of Cu from copper tape used for EDS measurements). TEM also confirms the quality of nanotubes and the patches came at the surface may be due to the organic solvents used for TEM measurements.

3.3.3 Mobility assisted Growth mechanism

Understanding the growth mechanism plays an important role in controlling and designing of nanostructures. Yao *et al.* [74] have explained a possible growth mechanism for the formation of metal nanostructures over alumina based on a current assisted growth mechanism. However, the role of metal ion mobility was not forthcoming in their investigations. It must be noted here that Yao *et al.* have carried out the electrodeposition at constant current density while the present set of experiments was carried out by keeping the voltage constant.

A possible mechanism based on the mobility assisted formation of nanotubes and wires in the case of constant voltage (Potentiostatic) deposition is discussed below. It is an already established fact that growth

mechanism in a porous material originates from the cathode surface at the bottom edge of the pore. Because of their reduced coordination number and high surface area, porous parts of the template (alumina) serve as energetically favourable sites for initiating metal atom adsorption.^[75-76]

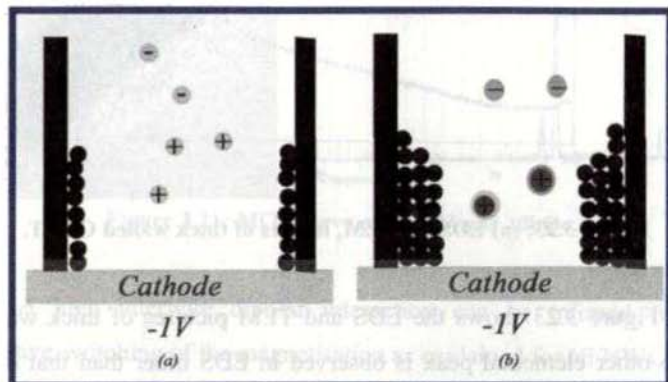


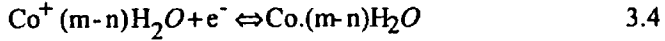
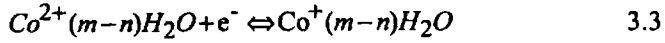
Figure 3.24: Schematic of mobility assisted growth mechanism, (a) nanotube growth, (b) nanowire growth.

When a negative potential is applied to the working electrode, divalent metal ions of Co^{2+} (Ni^{2+} ion in the case of Nickel sulphate) surrounded by hydration layer move towards the cathode and reduces to metal. This is a tri stage process and are as follows.

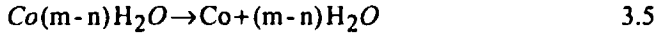
1. The hydration number of metal ions decreases and the metal ions (Co^{2+}) are rearranged in solution near the cathode surface which can be written as follows,



2. Co^{2+} ions, surrounded by water molecules are then reduced. This is a step by step process as observed in 3.3 and 3.4,



3. Eqn.3.5. is an adsorption process and the adsorbed metal cobalt discards the hydration layer and enters in to the crystal lattice.



The movement rate of ions in a given electric field E is depends on two factors, mobility of ions and the potential gradient across the working and counter electrode.

$$V_+ = \mu_+ \frac{dE}{dx} \quad 3.6$$

$$V_- = \mu_- \frac{dE}{dx} \quad 3.7$$

where V_+ , V_- are the movement rates of cobalt ion and acetate ion and μ_+ , μ_- are the mobility of cobalt ion and acetate ion respectively. The components of the metal ion movement rate V_{\parallel} and V_{\perp} and their competitions are the key parameters determining the resultant geometry after electrodeposition. Cao *et al.*³ reported the formation of nanowires under low applied current density, where in $V_{\parallel} \approx V_{\perp}$. At high applied current densities, this will lead to high values of $\frac{dE}{dx}$, and nanotubes are the resultant geometries because in this case $V_{\parallel} \gg V_{\perp}$. In our investigation a constant potential is maintained (Potentiostatically) for electrodeposition instead of keeping the current density constant (Galvanostatically).

A schematic representation of the mobility assisted growth of nanotubes and wires are depicted in Figure 3.24.a. and Figure 3.24.b.

respectively. The mobility of cobalt ions in cobalt acetate and cobalt acetate tetrahydrate can be different. The presence of other inorganic ions and organic additives in the double layer or adsorbed on to the surface can greatly modify the electro-crystallisation and growth process. The three factors affecting the mobility of the ions during electrodeposition are the asymmetry effect, electrophoretic effect and the viscous effect. Each of these can be different from precursor to precursor and the electrophoretic effect, which is due to the radicals of water of hydration, can be prominent in hydrated salt solutions. Based on these considerations, several deposition mechanisms have been proposed.^[77-79] So the extra hydration in tetrahydrate will act as a dead layer and shield the metal ions from the external potential. This case is similar to that of low current density deposition in Current Directed Tubular Growth Mechanism (CDTG) as discussed by Yao *et al.*, where V_{\parallel} is similar to V_{\perp} . Here, as the time increases, metal atoms will fill most of the template pores until they are completely filled. But in the case of Cobalt acetate, Cobalt ion mobility will be much higher and also have an enhanced parallel velocity component. So a Co nanotube is the resultant one.

The key factors determining the morphology of the one dimensional objects (nanowires or tubes) in an electrodeposition are the mobility of metal ions and number of hydrated ions attached. Similarly, in the case of Nickel ions, the mobility can be different in Nickel sulphate and Nickel sulphate hexahydrate. It is also inferred that the presence of hydration layer will act as a shield for external applied potential and thereby ion mobility can be reduced. This mechanism is validated and generalised by other precursors like cobalt sulphate too. This can be treated as a general growth mechanism in the constant voltage deposition process for all types of metal nanowires, and open the possibility for controlling the formation of one dimensional structures. Optimization and standardization of process parameters will help

to control the thickness of nanotubes and there by pave way for tailoring the properties.

3.3.4 Ni @ Co core-shell nanostructures

The expertise gained during the synthesis of Ni and Co nanowires and nanotubes using various precursors extended to the synthesis of their hybrid structures. Nickel (Ni) electrodeposited inside Cobalt (Co) nanotubes (a new system named Ni @ Co nanorods) are fabricated using a two step potentiostatic electrodeposition method. Testing the veracity of the growth mechanism in other porous membranes such as metal nanotubes will help to design multisegmented nanostructures; they can find enormous applications in various fields such as energy storage, controlled transport, and magnetic memory elements. ^[80]

3.3.4.1 Fabrication of Ni @ Co nanorods

0.2 M Cobalt acetate was used as the precursor for electrodeposition for making cobalt nanotubes and the deposition was carried out for a time period of 1 hour. Ni NWs have been electrodeposited in to these Co NTs using 0.2M nickel sulphate hexahydrate ($\text{NiSO}_4 \cdot 6\text{H}_2\text{O}$) in 0.1M Boric acid (H_3BO_3) as electrolyte for 1 hour.

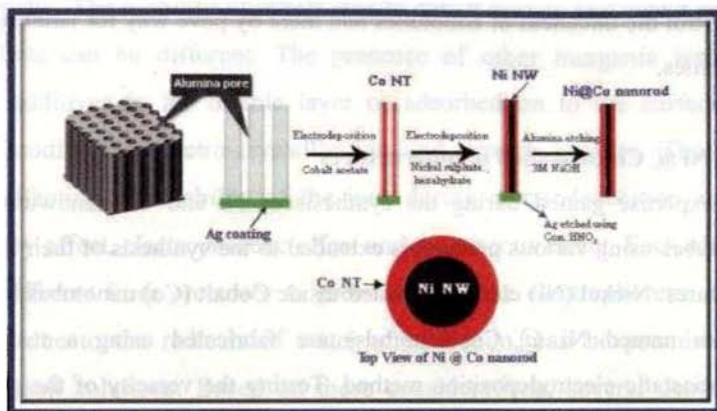


Figure 3.25: Schematic diagram showing the synthesis of Ni @ Co nanorods.

The formation of Co NT and subsequent formation of Ni NW inside Co NT are consistent with the mobility assisted growth mechanism as discussed above for nanoporous alumina. In generalizing this mobility assisted growth mechanism, it is to be concluded that mobility of the cation and the hydration layer over the cation are the important parameters determining the morphology of one dimensional structure after electrodeposition.

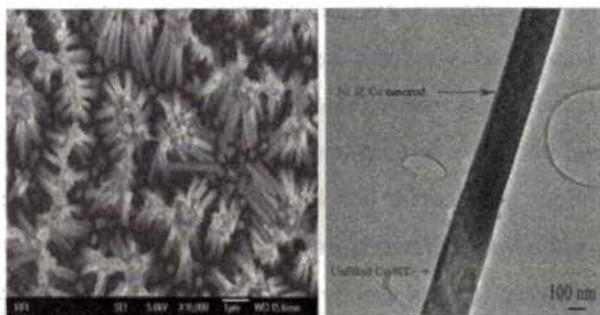


Figure 3.26: (a) FESEM image of Ni @ Co nanorods, and (b) TEM image of Ni @ Co nanorod.

Figure 3.26.a depicts the FESEM image of Ni @ Co nanorods. It indicates that the Ni @ Co nanorods have an average length of 15 μ m and diameter of ~150 nm. The formation of core-shell nanostructure with Co NT as shell and Ni NW as core is clear from the TEM image (Figure 3.26.b). The compositional analysis of these nanorods has been carried out using Energy Dispersive Spectrum (EDS), and is shown in Figure 3.27.

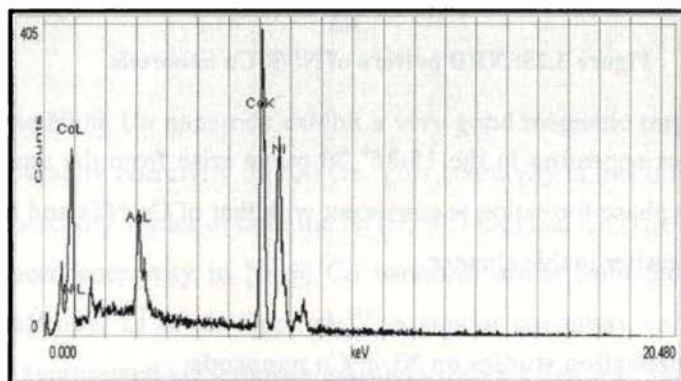


Figure 3.27: EDS of Ni @ Co nanorods.

The presence of Co and Ni is evident from the EDS. The presence of small amount of silver (Ag) is coming from the back coating, which served as working electrode during electrodeposition. The phase formation in Ni @ Co nanorods is verified using XRD pattern. Figure 3.28 shows the XRD pattern of Ni @ Co nanorods and it indicates the presence of two separate phases, face centred cubic (fcc) Ni and hexagonally closed packed (hcp) Co. It also indicates that the Ni @ Co nanorods are crystalline.

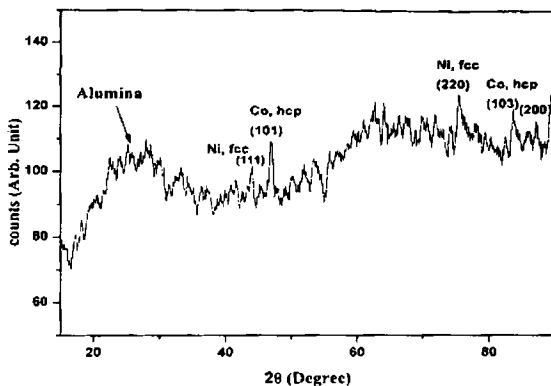


Figure 3.28: XRD pattern of Ni @ Co nanorods.

Broad features appearing in the $15\text{-}35^\circ$ 2θ range arise from the amorphous alumina. The phase formation is consistent with that of Co NTs and Ni NWs as presented earlier in this chapter.

3.3.4.2 Magnetisation studies on Ni @ Co nanorods

In order to investigate the magnetic properties of crystalline Ni @ Co nanorods, room temperature and low temperature (6K) magnetic properties of the Ni @ Co nanorods were evaluated using SQUID magnetometer. Figure 3.29.a and 3.29.b depict the room temperature and low temperature (6K) $M(H)$ curves of Ni @ Co nanorods measured parallel to the nanorods respectively.

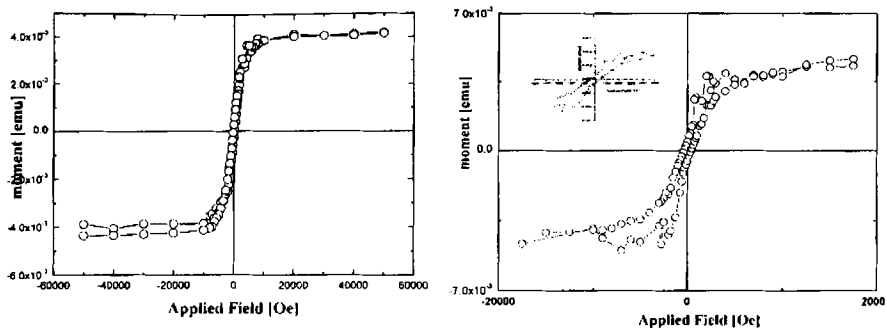


Figure 3.29: M(H) curves of Ni @ Co nanorods; (a) at room temperature (b) at 6K.

The Ni @ Co nanorods exhibit a very good magnetic response with room temperature coercivity of 200 Oe. This coercivity is much higher than the bulk coercivity values of both the Ni ($H_c=0.7$ Oe) and Co ($H_c=10$ Oe).^[56] The enhanced coercivity in Ni @ Co nanorods arises from the enhanced shape anisotropy. Li et al. reported^[45] a similar coercivity value for Co nanotubes synthesized via template assisted synthesis, but it is much smaller than of Co NTs discussed earlier having very high aspect ratio. This is due to the fact that the shape anisotropy in the earlier report is much higher (aspect ratio of Co NTs is ~ 330) than that of the present (aspect ratio of Ni @ Co nanorods is ~ 100). The coercivity value for Ni @ Co nanorods is higher than that reported for Ni NWs^[80] having very high aspect ratio and it is due to the presence of cobalt. This indicates that one can tailor the coercivity of these heterostructures by controlling the aspect ratio as well as cobalt content. M(H) curve at 6K exhibit an enhanced coercivity of ~ 380 Oe. This is much higher than the other reported values of Co based alloy nanowires.^[41] The enhancement in coercivity at low temperatures is consistent with the monotonic increase of uniaxial anisotropy constant with decreasing temperature, with the basic assumption that the shape anisotropy is independent of temperature for high aspect ratio tubes.^[66] Similar to Co

NTs, Co NWs and Ni NWs, squareness ratio (M_r/M_s) of the Ni @ Co nanorods is also very small. This may be due to the very high magnetic dipolar interrod interaction between each rod. This type of hybrid magnetic system with higher aspect ratio and much higher coercivity can find applications in fields such as data storage where a high coercivity is required.

Conclusion

Magnetic nanowires and nanotubes of Ni and Co are synthesised using template assisted electrodeposition technique. Highly crystalline and textured Ni NWs and Ni NTs are synthesised using Nickel sulphate as precursor for electrodeposition in a potentiostatic electrodeposition of -1V. Co NTs of highly ordered with hexagonal close packed structure are formed by the electrodeposition of cobalt acetate (for the first time) in a constant potential of -1V. The nanotubes and nanowires of 5 hour electrodeposited have a maximum outer diameter of ~150 nm and length of ~50 μ m. Co NTs exhibit the highest reported longitudinal coercivity ~820 Oe at room temperature. Co NWs with high aspect ratio (~330) and high coercivity are synthesized by electrodeposition using and cobalt sulphate heptahydrate ($\text{CoSO}_4 \cdot 7\text{H}_2\text{O}$) precursor and constant potential of -1V. They exhibit a preferential growth along $\langle 110 \rangle$. Cobalt acetate tetrahydrate is employed to fabricate thick-walled nanotubes. A very high interwire interaction resulting from magnetostatic dipolar interaction was observed between nanowires and nanotubes. An unusual low temperature magnetisation switching due to this dipolar interaction for field parallel to the wire axis is evident from the peculiar high field M(T) curve.

A plausible mechanism for the formation of nanotubes and nanowires during template assisted electrodeposition based on mobility assisted growth mechanism is elucidated. Such tunability and control over

the formation of magnetic nanotubes or wire opens a unique opportunity to systematically approach these one dimensional structures for exploring their possible applications in areas such as magnetic recording, sensors, catalysis, and so forth. The role of hydration layer on the resulting one dimensional geometry in the case of potentiostatic electrodeposition is verified. These highly crystalline textured Ni and Co NWs and NTs are possible candidates for perpendicular recording and various other multifunctional devices. Moreover, understanding the growth mechanism of one dimensional structures will help design different coaxial multifunctional nanostructures which can find enormous applications in various fields.

A novel magnetic nanostructure called Ni @ Co nanorods with Ni NW as core and Co NT as shell was synthesized using a two step electrodeposition method. Mobility assisted growth mechanism for the formation of one dimensional nanostructures in potentiostatic electrodeposition is verified in the case of other nanoporous membrane such as Co NTs too. Structural studies indicate the formation of Ni and Co in two phases. Magnetic studies exhibited a high coercivity for the Ni @ Co NTs and they can find enormous applications in various fields where high coercivity is required.

References

1. Meng, G. W.; Jung, Y. J.; Cao, A.; Vajtaj, R.; Ajayan, P. M. *PNAS* (2005) 102 7074.
2. Iijima, S. *Nature* (1991) 354 56.
3. Cao, H.; Wang, L.; Qiu, Y.; Wu, Q.; Wang, G.; Zhang, L.; Liu, X. *ChemPhysChem* (2006) 7 1500.
4. Yanagishita, T.; Nishio, K.; Masuda, H. *Adv. Mater.* (2005) 17 2241.
5. Park, M.; Harrison, C.; Chaikin, P. M.; Register, R. A.; Adamson, D. *H. Science* (1997) 276 1401.
6. Tonucci, R. J.; Justus, B. L.; Campillo, A. J.; Ford, C. E. *Science* (1992) 258 783.
7. Whitney, T. M.; Jiang, J. S.; Searson, P. C.; Chien, C. L. *Science* (1993) 261 1316.
8. Steinhart, M.; Wehrshon, R. B.; Gosele, U.; Wendorff, J. H. *Angew. Chem. Int. Ed.* (2004) 43 1334.
9. Bao, J.; Tie, C.; Xu, Z.; Zhou, Q.; Shen, D.; Ma, Q. *Adv. Mater.* (2001) 13 21.
10. Nielsch, K.; Castano, F. J.; Matthias, S.; Lee, W.; Ross, C. A. *Adv. Eng. Mater.* (2005) 7 4.
11. Xia, Y.; Yang, P.; Sun, Y.; Wu, Y.; Mayers, B.; Gates, B.; Yin, Y.; Kim, F.; Yan, H. *Adv. Mater.* (2003) 15 353.
12. Rao, C.N.R.; Nazh, M.; *Dalton Trans.* (2003) 1 1.
13. Remskar, M. *Adv. Mater.* (2004) 16 1497
14. Tenne, R. *Colloids Surf. A* (2002) 208 83.
15. Lee, W.; Scholz, R.; Nielsch, K.; Gosele, U. *Angew. Chem. Int. Ed.* (2005) 44 6050.
16. Heydon, G. P.; Hoon, S. R.; Farley, A. N.; Tomlinson, S. L.; Valera, M. S.; Attenborough, K.; Schwarzacher, W. J. *Phys. D Appl. Phys.* (1997) 30 1083.
17. Sharif, R.; Shamaila, S.; Ma, M.; Yao, L. D.; Yu, R. C.; Han, X. F.; Khaleeq-ur-Rahman, M. *Appl. Phys. Lett.* (2008) 92 032505.
18. Puntces, V. F.; Krishnan, K. M.; Alivisatos, A. P. *Science* (2001) 291 2115.
19. Jung, S. W.; Park, W. I.; Yi, G. C.; Kim, M. Y. *Adv. Mater.* (2003) 15 1358.
20. Bao, J.; Liang, Y.; Xu, Z.; Si, L. *Adv. Mater.* (2003) 15 1832.

21. Sahoo, S.; Petravic, O.; Kleemann, W.; Stappert, S.; Dumpich, G.; Nordblad, P.; Cardoso, S.; Freitas, P. P. *Appl. Phys. Letts.* (2003) 82 4116.
22. Garcia, J. M.; Asenjo, A.; Velazquez, J.; Garcia, D.; Vazquez, M.; Aranda, P.; Hitzky, E. R. *J. Appl. Phys.* (1999) 85 5480.
23. Martin, J. I.; Nogues, J.; Liu, K.; Vicent, J. L.; Schuller, I. K. *J. Magn. Magn. Mater.* (2003) 256 449.
24. Yu, C. Y.; Yu, Y. L.; Sun, H. Y.; Xu, T.; Li, X. H.; Li, W.; Gao, Z. S.; Zhang, X. Y. *Materials Letters* (2007) 61 1859.
25. Whitney, T. M.; Searson, P. C.; Jiang, J. S.; Chien, C. L. *Science* (1993) 261 1316.
26. Basu, S.; Chatterjee, S.; Saha, M.; Bandyopadhyay, M.; Mistry, K.; Sengupta, K. *Sens. Actuators B* (2001) 79 182.
27. Meng, G.; Cao, A.; Cheng, J. Y.; Vijayaraghavan, A.; Jung, Y. J.; Shima, M.; Ajayan, P. M. *J. Appl. Phys.* (2005) 97 064303.
28. Lew, K. K.; Redwing, J. J. *J. Cryst. Growth* (2003) 254 14.
29. Wang, Y. C.; Leu, I. C.; Hon, M. H. *J. Cryst. Growth* (2002) 237 564.
30. Athanassiou, E. K.; Grossmann, P.; Grass, R. N.; Stark, W. J. *Nanotechnology* (2007) 18 165606 (7pp).
31. Fert, A.; Piraux, L. *J. Magn. Magn. Mater.* (1999) 200 338-358.
32. Fasol, G. *Science* (1998) 280 545.
33. Martin, C. R. *Science* (1994) 266 1961.
34. Kodama, R. H.; Berkwitz, A. E.; Meniff, E. J.; Foner, S. *Phys. Rev. Lett.* (1996) 77, 394.
35. Goya, G. F.; Forseca, F. C.; Jardin, R. F.; Muceillo, R.; Carreno, N. L. V.; Longo, E.; Leite, E. R. *J. Appl. Phys.* (2003) 93 6531-6533.
36. Kafil, M. R.; Saibal, R. *J. Appl. Phys.* (2008) 103, 084302.
37. Escrig, J.; Lavin, R.; Palma, J. L.; Denardin, J. C.; Altbir, D.; Cortes, A.; Gomez, H. *Nanotechnology* (2008) 19 075713(6pp).
38. Rivas, J.; Kazadi Mukenga Bantu, A.; Zaragoza, G.; Blanco, M. C.; Lopez-Quintela, M. A. *J. Magn. Magn. Mater.* (2002) 249 220-225.
39. Gubbiotti, G.; Tacchi, S.; Carlotti, G.; Vavassori, P.; Singh, N.; Goolaup, S.; Adeyeye, A. O.; Stashkevich, A.; Kostylev, M. *Phys. Rev. B* (2005) 72 224413.
40. Goolaup, S.; Adeyeye, A. O.; Singh, N. *J. Appl. Phys.* (2006) 100 114301.

41. Bao, J.; Chen, W.; Liu, T.; Zhu, Y.; Jin, P.; Wang, L.; Liu, J.; Wei, Y.; Li, Y. *ACS Nano*, (2007) 1 293.
42. Srivastava, A. K.; Singh, R. S.; Sampson, K. E.; Singh, V. P.; Ramanujan, R. V.; *Metallurgical and Materials Transactions A* (2007) 38A 717.
43. Wang, T.; Wang, Y.; Li, F.; Xu, C.; Zhou, D. *J. Phys. Condens. Matter.* (2006) 18 10545.
44. Fert, A.; Piroux, L. *Journal of Magnetism and Magnetic Materials* (1999) 200 338.
45. Dongdong Li, Richard S Thompson, Gerd Bergmann, and Jia G Lu, *Adv. Mater.*, (2008) 20 1.
46. Talapatra, S.; Tang, S.; Padi, M.; Kim, T.; Vajtai, R.; Sastry, G V C; Shima, M.; Dcevi, S. C.; Ajayan, P. M. *J. Mater. Sci.*, (2008) 44 2271.
47. Xiang-Zi Li, Xiang-Wen Wei, Yin Ye, *Mater. Lett.*, (2009) 63 578.
48. Chun Uney Wu, Hu Long Lin, Nai Ling Shau, *J. Solid. State Electrochem*, (2006) 10 198.
49. Licai Fu, Jun Yang, Qinling Bi, Weimin Liu, *Nanoscale Res. Lett.*, (2009) 4, 11.
50. F S Ou, M M Shaijumon, P M Ajayan, *Nano Lett.*, (2008) 8, 1853.
51. Bantu, A. K. M.; Rivas, J.; Zaragoza, G.; Quintela, M. A. L.; Blanco, M. C. *J. Appl. Phys.* (2001) 89 3393.
52. Cao, H.; Wang, L.; Qiu, Y.; Wu, Q.; Wang, G.; Zhang, L.; Liu, X. *ChemPhysChem* (2006) 7 1500.
53. Cao, H.; Tie, C.; Xu, Z.; Hong, J.; Sang, H. *Appl. Phys. Lett.* (2001) 78 1592.
54. Guowen, M.; Fangming, H.; Xianglong, Z.; Bcnsong, C.; Danchi, Y.; Jianxiong, L.; Qiaoling, X.; Mingguang, K.; Xiaoguang, Z.; Yajun, J.; Zhaoqin, C.; Min, Y.; Swastik, K.; Robert, V.; Ajayan, P. M. *Ange. Chem.* (2009) DOI :10.1002/anie.200901999.
55. Bao, J.; Tie, C.; Xu, Z.; Zhou, Q.; Shen, D.; Ma, Q. *Adv. Mater.* (2001) 13, 1631.
56. Chikazumi, S. *Physics of Magnetism*. New York, John Wiley & Sons, (1964).
57. Sun, L.; Hao, Y.; Chein, C. L.; Searson, P. C. *IBM J. RES. & DEV.* (2005) 49 79.

58. Stoner, E. C.; Wohlfarth, E. P. *Philos. Trans. R. Soc. London, Ser. A* (1991) 27 3475.
59. Russier, V.; Petit, C.; Pileni, M. P. *J. Appl. Phys.* (2003) 93, 10001.
60. Sahoo, Y.; Cheon, M.; Wang, S.; Luo, H.; Furlani, E., P.; Prasard, P. N. *J. Phys. Chem. B* (2004) 108 3380.
61. Ngo, A. T.; Pileni, M. P. *Adv. Mater.* (2000) 12 276.
62. Pileni, M. P. *Adv. Funct. Mater.* (2001) 11 323.
63. E. Alphande, Y. Ding, T. Ngo, Z. L. Wang, L. F. Wu and M. P. Pileni, *ACS Nano* (2009).
64. Sellmyer, D. J.; Zheng, M.; Skomski, R. *J. Phys.; Condens. Matter* (2001) 13 R433.
65. Heydon, G. P.; Hoon, S. R.; Farley, A. N.; Tomlinson, S. L.; Valera, M. S.; Attenborough, K.; Schwarzacher, W. *J. Phys. D: Appl. Phys.* (1997) 30 1083.
66. Henry, Y.; Ounadjela, K.; Piraux, L.; Dubois, S.; George, J. M.; Duvail, J. L. *Eur. Phys. J.B* (2001) 20 35.
67. Ounadjela, K.; Ferre, R.; Louail, L.; George, J. M.; Maurice, J. L.; Pirax, L.; Dubuis, S. *J. Appl. Phys.* (1997) 81 5455.
68. Smith, B. *Infrared spectroscopy interpretation* CRC Press, USA (1999).
69. Henry, Y.; Ounadjela, K.; Piraux, L.; Dubois, S.; George, J. M.; Duvail. *Eur. Phys. J. B* (2001)20 35.
70. Yu, C. Y.; Yu, Y. L.; Sun, H. Y.; Xu, T.; Li, X. H.; Li, W.; Gao, Z. S.; Zhang, X. Y. *Materials Letters* (2007) 61 1859.
71. Sellmyer, D. J.; Zheng, M.; Skomski, R. *J. Phys.; Condens. Matter* (2001) 13 R433.
72. Sun, L.; Hao, Y.; Chein, C. L.; Scarson, P. C. *IBM J. RES. & DEV.* (2005) 49 1.
73. Martin, J. I.; Nogues, J.; Liu, K.; Vicent, J. L.; Schuller, I. K.; J. *Mag. Mag.Mater.s* (2003) 256 449.
74. Yoo, W. C.; Lee, J. K. *Adv. Mater.* (2004) 16 1097
75. Lahav, M.; Schayek, T.; Vaskevich, A.; Rubinstein, I. *Angew. Chem.* (2003) 115 5734.
76. Lahav, M.; Schayek, T.; Vaskevich, A.; Rubinstein, I. *Angew. Chem. Int. Ed.* (2003) 42 5576.

77. Handbook of metallurgical process design-George E Totten, Kiyoshi Funatani, Lin Xie, CRC Press (2004).
78. Arthur W Adamson, A Text book of Physical Chemistry, Academic Press, 2nd Edition, New York (1979).
79. Puri, B. R.; Sharma, L. R.; Pathania, M. S. Principles of physical chemistry Vishal publishing Co., India (2006).
80. R Sharif, S Shamaila, M Ma, L D Yao, R C Yu, X F Han, M Khaleeq-ur-Rahman, Appl. Phys. Lett. (2008) 92 032505.

Chapter 4

Synthesis and Properties of MWCNT Based Magnetic Heterostructures and Their Possible Applications

This chapter discusses the fabrication of Multiwalled Carbon Nanotubes (MWCNTs) using template assisted Chemical Vapour Deposition and their subsequent hybridisation with magnetic materials such as Cobalt, Nickel and Iron Oxide. Cobalt and Nickel were electrodeposited inside aligned MWCNTs employing different precursors for electrodeposition. These hybrid structures were then subjected to detailed structural, morphological and magnetic investigations. The veracity of the mobility assisted growth mechanism inside carbon nanotubes is also tested. Nickel filled MWCNTs were subjected to microwave absorption studies in the S-band using cavity perturbation technique and the results were compared with that of bare MWCNTs and Ni NWs. Aqueous ferrofluids based on Iron Oxide are synthesized using a controlled co-precipitation technique. Carbon nanotubes are filled with aqueous Ferrofluids using the principle of nanocapillarity. Structural, morphological and magnetic properties of these nanocomposites are analysed using FESEM, TEM, SAED, Micro-Raman and SQUID magnetometer.

**A part of the work discussed in this chapter has been reported in*

1. *"Nanotechnology" (2009, 20, 055607)*
2. *"ECS Letters" (2009, 12(4), K21)*
3. *"Nanotechnology" (2009, 20, 285702)*

4.1 Introduction

The landmark paper on carbon nanotubes (CNTs) by Iijima^[1] in 1991 and the subsequent successful synthesis of CNTs in bulk^[2] triggered a multitude of research activities on CNT based materials. CNTs and CNT based materials are appealing to both engineers and scientists because of their superlative physicochemical properties.^[3-7] The unique and interesting electronic, mechanical, optical and structural properties of carbon nanotubes made them extremely promising for applications in materials science and medicine.^[8-9] CNTs assume significance not only because of their unique electrical and optical properties but they are also ideal templates for the synthesis of various other nanostructures. The formation of tubular structures, ranging from a few nanometers to few tens of nanometers in diameter suggests the possibility of engineering these nanostructures on scales considerably larger than those to the fullerenes and immense research is underway in these tubular carbon nanostructures all over the world. Moreover, these excellent quasi-one-dimensional nanostructures provide a unique platform for studying the physics at low dimensions.^[10]

The combination of magnetic materials and CNTs is emerging as an interesting area of advanced research.^[11] Nanocomposites consisting of carbon nanotubes (CNTs) and magnetic materials have been attracting the interest of many researchers and considerable amount of research is underway in this area, especially on the synthesis and properties.^[12-13] Numerous attempts were made earlier to fill CNTs with metallic elements or compounds.^[14-19] The application potential of these metal encapsulated composites extend to various fields like spin polarized transportation, magnetoresistive random access memory, nano-electronic devices and radar absorbers.^[20] The microwave absorbing properties of CNT-metal composites are of importance because of its usefulness in military and business fields.^[21] A good electromagnetic absorber should possess the required dielectric

permittivity and appropriate magnetic permeability in a given frequency of operation leading to perfect impedance matching. Due to the modification of their electronic structure, metal incorporated CNTs are found to be good microwave absorbers.^[22] Embedding metallic inclusions in MWCNTs will also provide encapsulation and passivation leading to long term stability.

The filling of CNTs is accepted as an ingenious idea right from the early days of CNT research^[23-28] and attempts for complete filling of CNTs are an ongoing research activity rewarded only with partial success.^[29] The confined existence of particles inside CNTs might introduce interesting new properties which are unseen in these systems previously.^[30] Moreover filling of CNTs leads to confinement of particles and confinement of nanoparticles leads to possible quantum mechanical effects. Various chemical^[31] and physical methods^[32] are in vogue for filling of CNTs. Immediately after the theoretical prediction of capillary filling of CNTs by Pederson and Broughton,^[33] attempts were made to fill CNTs by capillary action of molten metals. However attempts to completely fill CNTs were in vain or have met with only partial success.^[34]

Electrodeposited metal nanowires are increasingly becoming popular, and they are a hot topic of research due to their application potential in ultrahigh density magnetic recording, ultrafast optical switching, and microwave devices. Metal nanotubes are another interesting system of current research where they can find enormous applications in hybrid nanostructures for possible energy storage devices, cell separation and diagnosis.^[35] Electrodeposition of metals inside CNTs has not yet been perfected due to the buckling and bending of carbon nanotubes during electrodeposition. Electrodeposited ferromagnetic fillings inside the carbon shell are protected against oxidation and hence ensure long term stability. Moreover, decoration of CNTs with magnetic nanoparticles, such as coating or loading CNTs with $\gamma\text{-Fe}_2\text{O}_3$, NiFe_2O_4 , and Fe_3O_4 impart new optical,

magnetic and electrochemical properties to CNTs.^[9] The hybrid magnetic nanostructures based on CNTs can find applications ranging from electromagnetic devices to biomedical fields such as magnetically guided drug delivery systems and agents for hyperthermia.^[36]

With the growing demand for good electromagnetic shields and absorbers the attention of scientists turned towards CNT based microwave absorbers. Isolated metallic soft magnetic materials have an upper hand over traditional ferrite based microwave absorbers because of their higher Snoek's limit in the GHz frequency regime.^[37-39] Filling of CNTs with 3d transition metals like Ni/Fe/Co will render them useful for applications such as electromagnetic interference shields and microwave absorbers. Due to the suppression of eddy current, isolated metallic particles having sizes less than their skin-depth can exhibit enhanced microwave absorption.^[40] Che *et al.*^[41] reported the microwave absorption of iron encapsulated carbon nanotubes and the enhanced microwave absorption of this system is attributed to the better impedance match between the dielectric loss and magnetic loss. Researchers adopted catalytic pyrolysis or wet chemical routes for the synthesis of MWCNTs-metal composites.^[38,42] Template assisted electrodeposition is an alternative to such techniques and it is an efficient and simple method for metal filling of MWCNTs.

The S band of the electromagnetic spectrum is extensively employed in weather radars, communication satellites, direct broadcast satellites, mobile satellite services and also in emerging WiMAX technology.^[43-45] Ni is employed as a filler in MWCNT due to its large resonance line width and it can be used for large band width microwave absorbers^[46] and literature reports on the microwave absorbing properties of Ni-MWCNT composite is rather scarce or seldom reported. The evaluation of complex dielectric permittivity of MWCNTs, Ni nanowires (Ni NWs) and Ni filled MWCNTs thus assume significance.

Nanocapillarity is the spontaneous penetration of fluids into wettable capillaries, and can be effectively utilized for filling large area of CNTs.^[29] This technique received the much needed fillip when open ended aligned CNTs were prepared.^[47] Potential applications of filled CNTs with different materials are in areas such as nanofluidic devices and functional devices like nanoexplorers and cell manipulators. The lack of complete understanding of liquid flow through nanochannels has propelled further activities on filling of CNTs by capillarity and their further characterizations.^[48-49] It must be noted here that the melting of materials often results in loss of useful physical properties of materials. Filling of CNTs with colloidal suspensions was thought of as an alternative to filling of CNTs with molten materials.

Ferrofluids (FF) are colloidal suspensions of magnetic particles and they display novel magnetic and magneto optical properties. The condition for arresting both agglomeration arising out of magnetic dipolar interaction and sedimentation due to gravity necessitates the size of magnetic particles inside the suspension to lie within 10nm.^[50] These nanometer sized magnetic particles in a ferrofluid are to be coated with an organic hull thus preventing them from agglomeration. The size constraint leads to interesting applications for ferrofluids under the action of an applied magnetic field. FFs can either be synthesized using hydrocarbon carriers or they can be aqueous based. Hydrocarbon based FFs are noted for their extensive applications in various engineering fields.^[51] The magneto optical and viscous properties of these FFs are utilized in making devices like heat sinks, damping arrestors and optical switches and can be used as magnetic inks in high speed printing technology.^[52] Aqueous magnetic fluids find innumerable applications in therapy, diagnostics and as nanoprobe for biological applications.^[53]

The absence of any natural magnetic ordering in CNT and the growing demand for structured nanomagnets in fields such as NEMS (Nano Electro Mechanical Systems),^[29] medicine and in defence persuaded

hybridization of CNT with magnetic materials. Use of FM melts to fill CNT is not practical because of the high melting point of FM metals and the interaction between their melts and carbon.^[34] Attempts to fill CNTs with magnetic oxides (ferrites) by employing physical methods such as vigorous stirring with salts^[54] and other chemical means did not realise the desired objectives. This persuaded researchers to seek alternatives and filling MWCNTs with FF was proposed as a viable alternative. Fabrication of CNT- FM composites can be achieved if FM particles can be dispersed as colloidal suspensions in a carrier fluid. Fortunately, FFs offer this platform and can be effectively utilized for this purpose.

In addition to a plethora of applications that can be perceived with FF filled CNTs, they are ideal templates for investigating the magnetic properties at the fundamental level. Confinement of ultrafine magnetic particles will give rise to volume effects and will induce shape anisotropy. Complex interplay between various interactions like exchange interaction, dipolar interaction, shape anisotropy along with various other surface effects will provide a unique opportunity to probe these interactions from a fundamental perspective. FFs are interesting because of the possibility of manipulating the interparticle interaction via dilution. For example, it would be interesting to explore the phenomena of confinement of superparamagnetic iron oxide nanoparticles (SPIONs) inside MWCNTs. FF filled CNTs can serve as potential nanoprobe for biological applications and as agents for magnetic hyperthermia. The ease with which CNTs can be functionalized provides further leverage to target CNTs to a specific site by the application of an external magnetic field. So yet another motivation of the present study is to explore these possibilities by the synthesis of a CNT-SPION composite.

4.2. Experimental

4.2.1 Synthesis of MWCNTs

MWCNTs were synthesized by template assisted chemical vapour deposition (CVD) over nanoporous alumina template (99.9% pure, Whatman). Acetylene (C_2H_2) was used as the precursor for pyrolysis and argon as a carrier gas. The temperature for pyrolysis was optimized at $650\text{ }^{\circ}C$ for the formation of nanotubes. The flow rate of acetylene (10 sccm) and argon (70 sccm) were optimized during the CVD process to obtain MWCNTs with a maximum inner diameter of $\sim 150\text{nm}$. The resultant nanotubes were plasma etched for removing the amorphous carbon content using a Radio Frequency (RF) plasma unit (Harrick PDC-32G, plasma power 18 W) and then used for further characterization. Figure 4.1 shows the schematic of template assisted CVD set up.

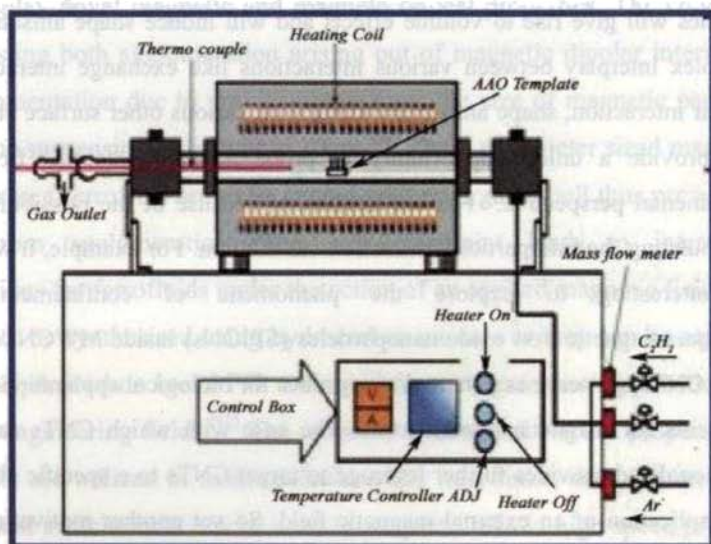


Figure 4.1: Schematic of template assisted CVD synthesis.

The resulting carbon nanotubes have an average length of $\sim 60 \mu\text{m}$. The FESEM images of MWCNTs are shown in Figure 4.3.

4.2.2. Metal filling inside MWCNTs

Nickel and Cobalt are electrodeposited inside MWCNTs using potentiostatic electrodeposition (as explained in Chapter 2 and Chapter 3). Different precursors are employed for electrodeposition. Schematic of electrodeposition is depicted in Figure 4.2.

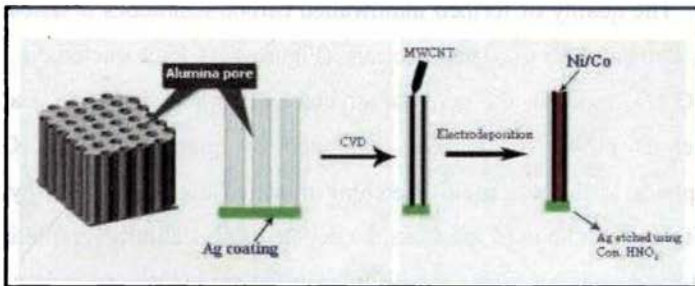


Figure 4.2: Schematic of electrodeposition inside MWCNTs.

Initially, the Ag coated AAO templates are subjected to Chemical Vapour Deposition (CVD) in order to grow MWCNTs inside the nanopores. These AAO templates are used as working electrode for electrodeposition and electrodeposition was carried out inside the AAO templates containing MWCNTs.

4.3 Results and discussion

The FESEM images (both lateral and top) of as synthesised MWCNTs are shown in Figure 4.3.

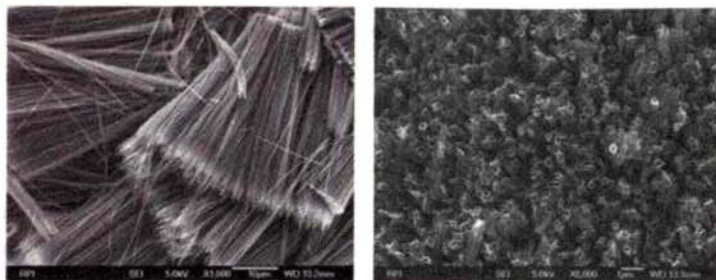


Figure 4.3: FESEM images of MWCNTs, (a) lateral view, (b) top view.

The quality of formed multiwalled carbon nanotubes is tested using Micro Raman analysis. The spectrum (Figure 4.4) is characteristic of the order G (E_{2g} mode in the graphite structure of carbon, 1600 cm^{-1}) and the disorder D (1343 cm^{-1}) peaks exhibited by graphite.^[55] The G-band corresponds to the tangential stretching mode of highly oriented pyrolytic graphite and can be used to assess the degree of crystallinity /graphitisation. The D-band originates from the disorder in the sp^2 hybridised carbon atoms and is characteristic of lattice distortions in the curved graphite sheets and/or tube ends.

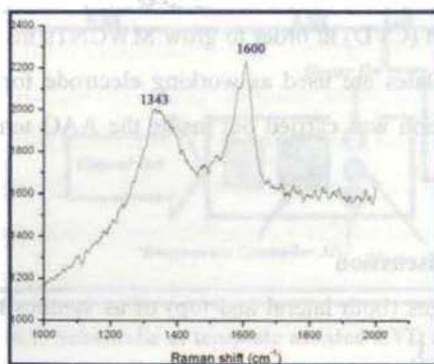


Figure 4.4: Micro Raman spectrum of MWCNT (excitation: 514.5 nm).

It is assumed that extend of graphitization is taken as a yard stick for good quality CNTs. This is found from the relative intensities of G and D peaks from the Raman spectra (relatively high intensity ratio of G to D (~ 1.2)) it is to be concluded that the formed carbon nanotubes are of high purity.^[56]

4.3.1. Ni filled MWCNTs

Nickel has been electrodeposited inside MWCNTs using Nickel sulphate hexahydrate as precursor. FESEM images of Ni filled MWCNTs are shown in Figure 4.5.

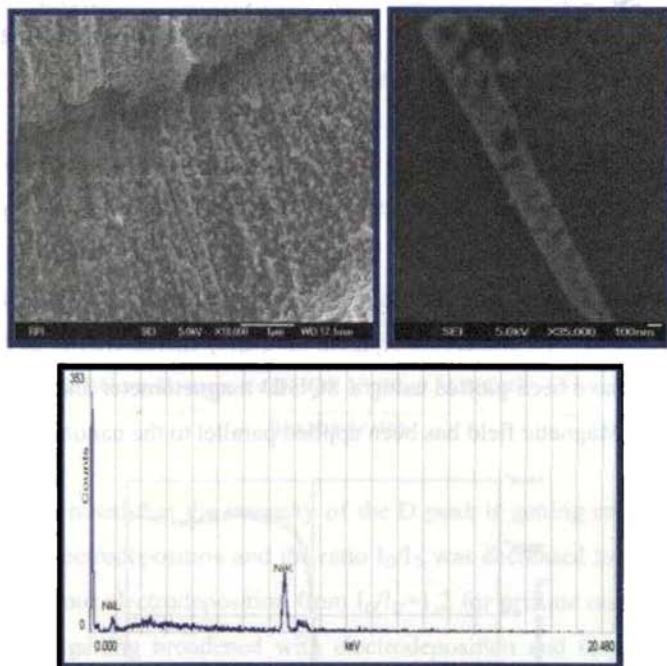


Figure 4.5: FESEM image of Ni filled MWCNT (Nickel sulphate hexahydrate): (a) a bundle of Ni filled MWCNTs, (b) a single Ni filled MWCNT over a silicon substrate, (c) EDS of Ni filled MWCNTs.

EDS of Ni filled MWCNT indicates the presence of elemental Ni. AFM and MFM studies are carried out on this single Ni filled MWCNT and is shown in Figure 4.6.

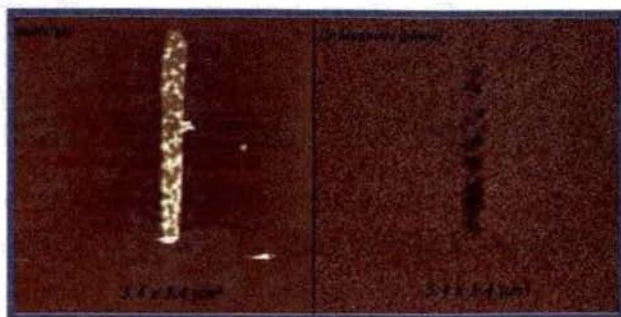


Figure 4.6: AFM, MFM images of a Ni filled MWCNT over a silicon substrate (Nickel sulphate hexahydrate).

The MFM phase contrast image is shown in Figure 4.6.b. The phase contrast clearly reveals the presence of 'magnetic' Ni particles inside the MWCNTs. Particle size of the filled Ni particles calculated from MFM image correlates well with the FESEM image (Figure 4.5) that they have an average size of ~ 70 nm. Room temperature $M(H)$ characteristics of Ni filled MWCNTs have been plotted using a SQUID magnetometer and is shown in Figure 4.7. Magnetic field has been applied parallel to the nanotube.

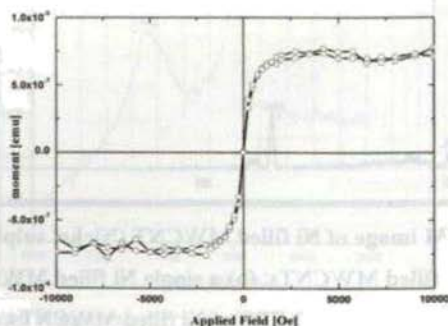


Figure 4.7: Room temperature $M(H)$ curve for Ni filled MWCNTs.

Though the particle size inferred from MFM and FESEM are higher than the critical particle size of nickel (~ 20 nm), the $M(H)$ curve exhibit a superparamagnetic behaviour for Ni filled MWCNTs ($H_c \sim 0$ Oe, $M_r \sim 0$ emu). This may be due to the agglomeration of nickel nanoparticles and the actual particle size can be less than that inferred from FESEM and MFM. Micro-Raman studies have been carried out on Ni filled MWCNTs after each hour of electrodeposition and is plotted in Figure 4.8.

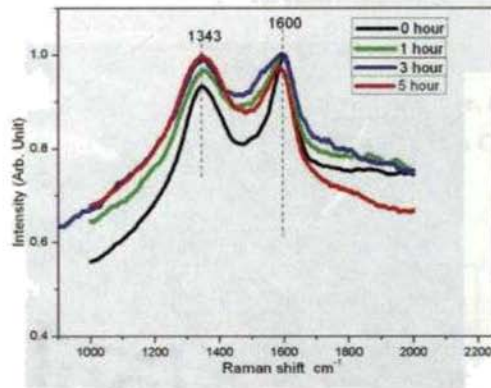


Figure 4.8: Micro-Raman studies on Ni filled MWCNTs (Nickel sulphate hexahydrate).

It is noted that the intensity of the D peak is getting enhanced after each hour electrodeposition and the ratio I_G/I_D was decreased to a value of ~ 0.6 after 5 hour electrodeposition from $I_G/I_D=1.2$ for pristine one. Moreover, the D peak getting broadened with electrodeposition and G peak slightly shifted to lower frequencies. This is thought to be because of the strain developed due to the introduction of metal particles and hence the number of defects also gets enhanced.^[57]

4.3.2. Co filled MWCNTs

Cobalt is electrodeposited inside MWCNTs using cobalt acetate and Cobalt sulphate heptahydrate. The morphology is different in this case and is shown in Figure 4.9 and Figure 4.12. As in the case of Co NTs (discussed in Chapter 3), Cobalt acetate after electrodeposition inside MWCNTs give rise to Co-axial nanotubular structure with MWCNTs. The bright open ended FESEM image indicate the formation co-axial structure and is named after this as Co-in-Carbon nanotube. EDS indicates the presence of elemental cobalt. This is further verified using TEM elemental mapping and is shown in Figure 4.10.

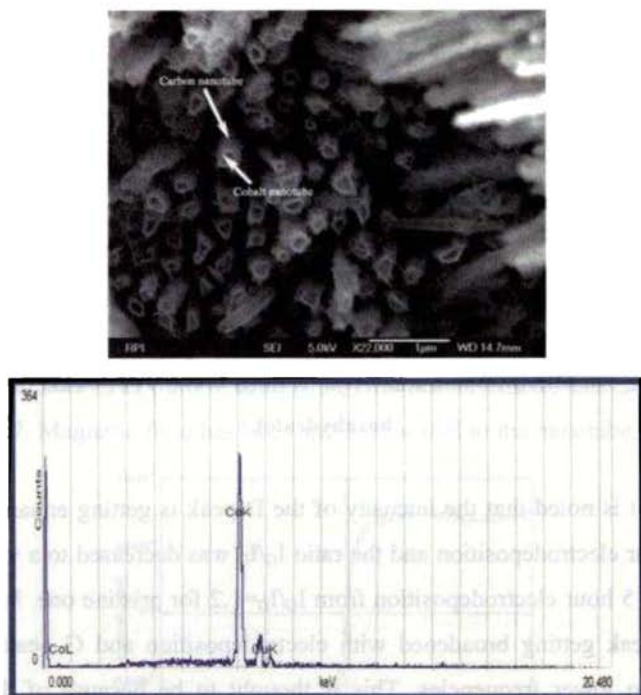


Figure 4.9: (a) FESEM image, (b) EDS of Co filled MWCNT (using Cobalt acetate).

The uniform mixing of green (carbon) and red (cobalt) indicates the co-axial structure of the resultant nanostructure after electrodeposition.

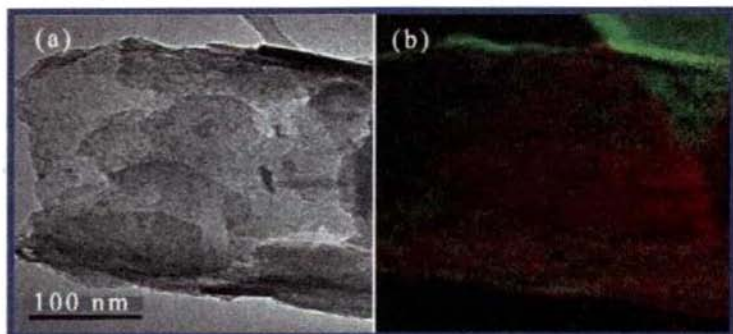


Figure 4.10: (a) TEM image Cobalt-in-Carbon nanotube, (b) elemental mapping of Cobalt-in-Carbon nanotube (red color indicates Cobalt and Green color indicates Carbon).

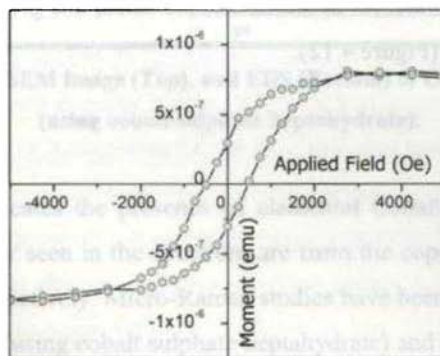


Figure 4.11: The room temperature $M(H)$ behaviour of the cobalt-in-carbon nanotubes for field parallel to the nanotube.

Figure 4.11 depicts the room temperature magnetic hysteresis for Co-in-Carbon nanotubes. The very high value of the coercivity (H_c , ~ 550 Oe) indicates that the easy axis of magnetisation is parallel to the tube axis and is

arising out of the very high shape anisotropy due to the very high aspect ratio of these tubular structures (aspect ratio~330).^[58-59] Since the coercivity value for bulk cobalt is only 10 Oe, the very high value obtained here can arise only from the uniaxial shape anisotropy, in the nanowire or nanotube form of cobalt.

The FESEM image shows the open ends of the nanostructure, which confirm the nanotube structure of the prepared sample. This further verifies the general mobility assisted growth mechanism that was discussed in chapter 3, in that the hydration layer in the cation and mobility of the cation determine the resultant morphology of one dimensional nanostructures after electrodeposition. The mobility assisted growth mechanism during electrodeposition seems to be valid in other nanopores such as carbon nanotubes too.

This is further tested by the electrodeposition of Cobalt using cobalt sulphate heptahydrate. As in the case of Co NWs, this gives in to a nanowire inside MWCNTs (Figure 4.12).

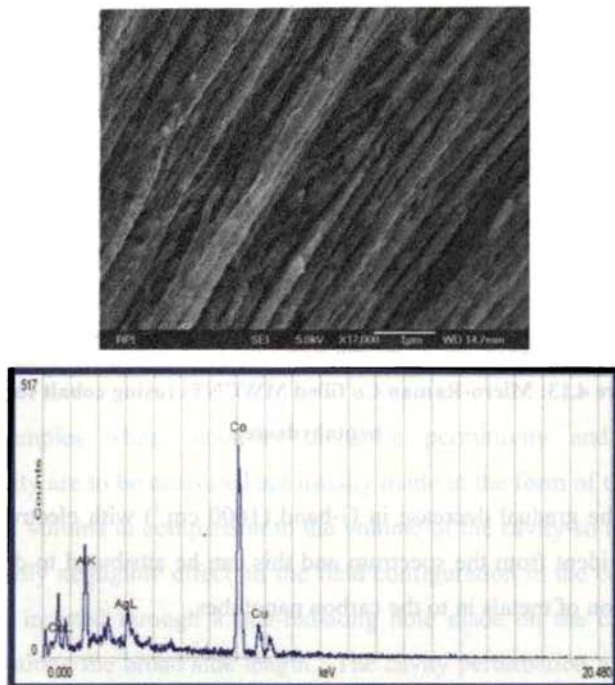


Figure 4.12: FESEM image (Top), and EDS (Bottom) of Co filled MWCNT (using cobalt sulphate heptahydrate).

EDS indicates the presence of elemental Cobalt. The presence of Copper and Silver seen in the spectrum are from the copper tape and silver back coating respectively. Micro-Raman studies have been carried out on Co filled MWCNTs (using cobalt sulphate heptahydrate) and is shown in Figure 4.13.

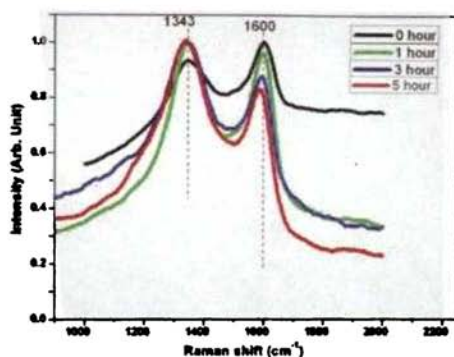


Figure 4.13: Micro-Raman Co filled MWCNTs (using cobalt sulphate heptahydrate).

The gradual decrease in G-band (1600 cm^{-1}) with electrodeposition time is evident from the spectrum and this can be attributed to defects with introduction of metals in to the carbon nanotubes.

4.4 Microwave absorption studies using cavity perturbation method

Cavity perturbation method is widely used to measure the complex dielectric permittivity and magnetic permeability of materials. Cavity is a rectangular box made of a non-magnetic metal with dimensions appropriately chosen to have resonance of electromagnetic waves in the frequency range of interest and connected to a vector network analyser through coaxial cables. The length (l), breadth (a), and height (b) of a cavity are so chosen to have a pre-determined TE mode to sustain in the cavity. The schematic of a cavity resonator is shown in figure 4.14.

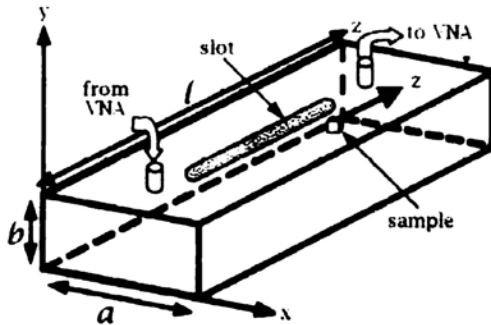


Figure 4.14: Schematic of a cavity resonator.

Samples whose complex dielectric permittivity and magnetic permeability are to be measured are usually made in the form of thin rods of very small volume in comparison to the volume of the cavity so that it must produce only negligible effect on the field configuration in the cavity. The sample is inserted through a non-radiating hole made on the cavity wall, generally along the broad side length. The cavity perturbation technique is based on the change in the resonant frequency and quality factor of the cavity due to the insertion of a sample in to it at the position of electric field maximum or magnetic field maximum, depending upon the nature of the parameter to be studied.

Complex dielectric permittivity and permeability measurements of MWCNTs, Ni NWs and Ni filled MWCNTs were carried out using a vector network analyzer (Rohde & Schwaz ZVB4). 0.01wt% solutions of MWCNT, Ni NW and Ni filled MWCNTs were prepared using a mixture of toluene and ethyl alcohol (1:2) after extensive sonication. These solutions were carefully filled in a capillary tube of known dimensions (measured using a travelling microscope) and inserted in to a rectangular cavity (waveguide-WR284) with a narrow line slot having dimension 3mm x180mm for permittivity measurements, (figure 4.15).

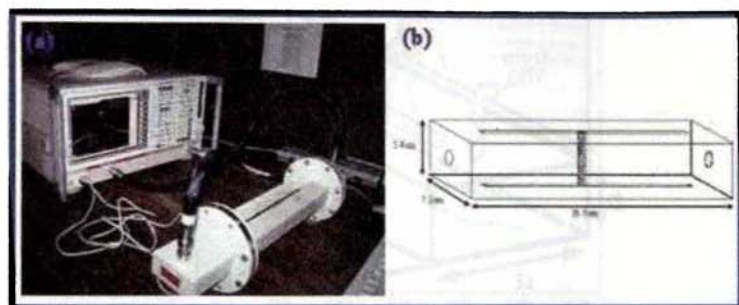


Figure 4.15: (a) Rohde & Schwaz ZVB4 network analyser, (b) schematic of WR284 waveguide.

The cavity was perturbed for different TE_{10n} modes. During the insertion of the sample, the resonant frequency and the quality factor changes and from this change in resonant frequency and quality factor the dielectric permittivity and dielectric loss of the material were evaluated using the formulae,^[60]

$$\epsilon_1 = \frac{V_c (f_c - f_s)}{2V_s f_s} + 1 \quad 4.1$$

$$\epsilon_2 = \frac{V_s}{4V_c} \left(\frac{1}{Q_s} - \frac{1}{Q_c} \right) \quad 4.2$$

where V_s and V_c are the volume of the material and cavity respectively, f_s and f_c are the resonance frequencies with and without the material while Q_s and Q_c are the corresponding quality factors of the sample and cavity, given by

$$Q_s = \frac{f_s}{f_c - f_s}, \quad Q_c = \frac{f_c}{f_c - f_s} \quad 4.3$$

Figure 4.16.a and 4.16.b show the variation of ϵ_1 and ϵ_2 with frequency. The real part of dielectric permittivity is found to be 11 and 14

for MWCNT and Ni nanowire respectively. There is a large increase in the permittivity (ϵ) for Ni filled MWCNT when compared to pristine MWCNT and Ni NW. Ni filled MWCNTs exhibited an enhanced permittivity (ϵ_r of 33.7 at 3.6GHz. The real part of dielectric permittivity decreased from 39 to 33.7 for Ni filled MWCNT in the frequency range of 2.4-3.6GHz.

The Ni filled MWCNTs also exhibited an increase in dielectric loss with an increase from 0.3 to 19.7 compared to that of pure MWCNTs.

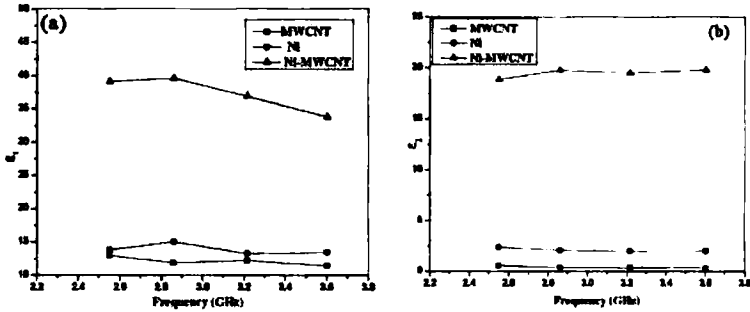


Figure 4.16: Variation of (a) ϵ_1 and (b) ϵ_2 with frequency.

The cavity perturbation technique which was employed for the evaluation of complex dielectric permittivity can also be used for determining the complex magnetic permeability of magnetic materials.^[61] When the material is introduced at the position of minimum electric field in a rectangular cavity (TE_{10n} mode), the real (μ_1) and the imaginary (μ_2) parts of the permeability are given by,^[62]

$$\mu_1 = 1 + K \frac{(f_c - f_s)}{f_s} \frac{V_c}{V_s} \quad 4.4$$

$$\mu_2 = \frac{K}{2} \left(\frac{1}{Q_s} - \frac{1}{Q_c} \right) \frac{V_c}{V_s} \quad 4.5$$

where K, the geometrical factor dependent on the guided wave length (λ_g) and width of the cavity (a) by the relation,

$$K = \frac{(\lambda_g^2 + 4a^2)}{8a^2} \quad 4.6$$

For the TE_{10n} mode, $\lambda_g = 2L/n$, where L is the length of the cavity and n=1,2,3,4.

Figure 4.17.a and 4.17.b depict the variation of μ_1 and μ_2 with frequency in the S band. The permeability of both the samples, Ni NWs and Ni filled MWCNTs, decreases with increase in frequency and is in agreement with other reports.^[63] Unfilled MWCNTs exhibited negligibly small complex permeability values.

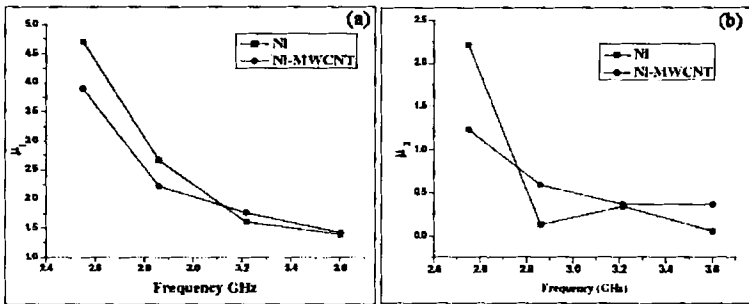


Figure 4.17: Variation of (a) μ_1 and (b) μ_2 with frequency.

In pure MWCNTs, the energy loss of the electromagnetic waves can be attributed to their dielectric loss,^[64] which arises out of their semi metallic nature and in turn their conductivity. When EM radiation is incident on metallic surfaces, the electric field will induce two types of electrical currents within the material. They are the conduction current induced due to the presence of free electrons in the metal and the displacement current due to bound charges. The conduction current will contribute to the imaginary

part of the permittivity (dielectric loss), whereas the displacement current will contribute to the real part of the permittivity. The later is due to polarization effect, which mainly involves the unpaired point defects. So the increase in the real part of the complex permittivity can be mainly ascribed to the dielectric relaxation and space charge polarization effects. The increase in the imaginary part of the complex permittivity can be attributed to the increase in electrical conductivity. They are governed by the relation $\sigma'(\omega) = \omega \epsilon_2(\omega)$ where $\sigma'(\omega)$ is the real part of the conductivity, ω is the angular frequency and $\epsilon_2(\omega)$ is the imaginary part of the permittivity.^[65]

In metal filled MWCNTs, the presence of a larger number of MWCNT – metal interfaces gives rise to enhanced interfacial electric polarization. Interfacial polarization aids the microwave absorption due to the interaction of microwave radiation with charge multipoles at the interfaces.^[66-67] In ferromagnetic metals, an additional effect known as magnetic resonance will also contribute to the microwave absorption. This magnetic resonance absorption occurs due to the coupling of microwave field to the internal magnetic moments. Moreover, if the impregnated metals are in the nanometric regime, quantum size effects will also play a major role leading to an increase in their energy level spacing and they increase the microwave absorption. From FESEM (Figure 4.5) and MFM (Figure 4.6.b) studies it is evident that there is a larger number of Ni – MWCNT interfaces in Ni filled MWCNT sample. Besides, the magnetic contrast in the MFM (Figure 4.6.b) proclaims that filled Ni nanoparticles are magnetic. The permeability values, μ_1 and μ_2 (Figure 3a and 3b) of Ni NWs and Ni filled MWCNTs are comparable with that of Fe filled MWCNTs^[41] and other reported values of magnetic nanowires such as $\text{Co}_{94}\text{Fe}_5\text{B}_2$.^[62] This indicates that the magnetic loss can also contribute to the microwave absorption in Ni NWs and Ni filled MWCNTs. So, both the interfacial polarization and

magnetic loss are contributing to the enhanced microwave absorption in the Ni filled MWCNTs. The average particle size of Ni particles inside MWCNTs is ~ 70 nm. Since the skin-depth of Ni at 1GHz is $\sim 0.5 \mu\text{m}$ (500 nm),^[68] there will be suppression of eddy currents in filled Ni nanoparticles. This also contributes to the enhanced microwave absorption of these composites. Defects in MWCNTs can also modify the dielectric permittivity due to multiple scattering and interfacial electric polarizations, which provides an additional impetus to the absorption mechanism.^[44] So Micro-Raman studies were conducted (at 514.5 nm) to identify the presence of defects in Ni filled MWCNTs and the result is shown in Figure.4.18.

Comparatively higher value of the relative intensity ratio of order (G) and disorder (D) peaks (I_G/I_D) ~ 1.2 indicates the extend of graphitization in pure MWCNT.^[56] But, the I_G/I_D is much lower (~ 0.7) for Ni filled MWCNTs. The reduction in the value of I_G/I_D along with a broad D peak (at $\sim 1340 \text{ cm}^{-1}$) in Ni filled MWCNT reveal the presence of defects in filled MWCNTs.^[57]

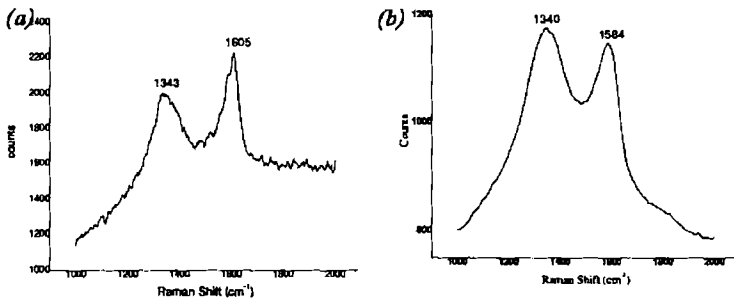


Figure 4.18: Micro-Raman spectrum of (a) pure MWCNT, (b) Ni filled MWCNT.

This is further confirmed by the shifting of G peaks to a lower value in Ni filled MWCNT (1584 cm^{-1}) compared to that of pure (1605 cm^{-1}). This

is thought to be due to strain and uneven curving of the graphite layers in the presence of metals.^[43] Though these defects do not alter the bandgap of MWCNTs, and so is the conductivity, however, they can act as polarization centers and thereby increase the ϵ_1 value.^[48] This gives credence to the belief that addition of defects in MWCNTs by filling of metals can significantly contribute to better microwave absorption characterizations.

4.5 MWCNT-SPION nanocomposites

4.5.1. Synthesis of Aqueous FF (AFF)

AFFs were synthesized by a controlled co-precipitation technique. Initially, nanosized iron oxide particles were prepared by chemical co-precipitation method with ferric chloride (FeCl_3) and ferrous sulphate ($\text{FeSO}_4 \cdot 7\text{H}_2\text{O}$) in the molar ratio 2:1. Aqueous ammonia was added to this solution aided by constant stirring at room temperature by maintaining the pH at 10. The resultant blackish Iron Oxide precipitate was collected and dispersed in a 3 molar citric acid solution. The resultant mixture was maintained at 90°C for half an hour and the residue was collected and dispersed in water by extensive sonication. By this technique, highly viscous ferrofluids with high shelf life and high thermal stability could be prepared.

4.5.2. Synthesis of MWCNT-SPION composite

For this, one drop of AFF ($\sim 3\mu\text{L}$) was placed over MWCNT. The fluid infiltrated in to the nanotubes instantaneously. A magnetic field ($\mu_0\text{H}\sim 1\text{T}$) was applied along the tube axis to enhance the infiltration process.

The carrier fluid was evaporated off at room temperature. Subsequently, the surface of CNT was etched by sonicating with ethanol in order to remove the surface layer. Alumina template was removed (for certain studies like SEM,

TEM, EDS) by dissolving the template in a 3molar sodium hydroxide (NaOH) solution and the residue was magnetically separated.

AFF prepared by co-precipitation exhibits high thermal stability and offered high shelf life. The fluid spiked even under small applied magnetic fields and this is an indicator of the fact that the FF synthesized by this method yielded high quality FF. Figure 4.19 shows the schematic of the infiltration processes.

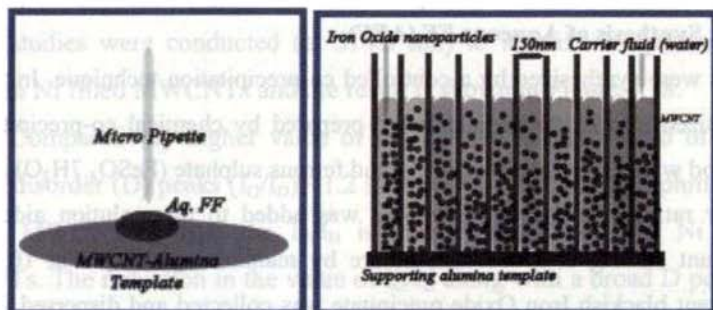


Figure 4.19: Schematic illustration of MWCNT filling by AFF.(a) Infiltration, (b) AFF filled MWCNT.

Figure 4.20.a and 4.20.b depict the FESEM images of AFF filled MWCNTs after the removal of the alumina template. The energy dispersive spectrum (EDS) of the MWCNT-SPION composite is displayed in Figure 4.20.c. Evidence for the presence of element iron emanating from iron oxide can be clearly seen in the spectrum.

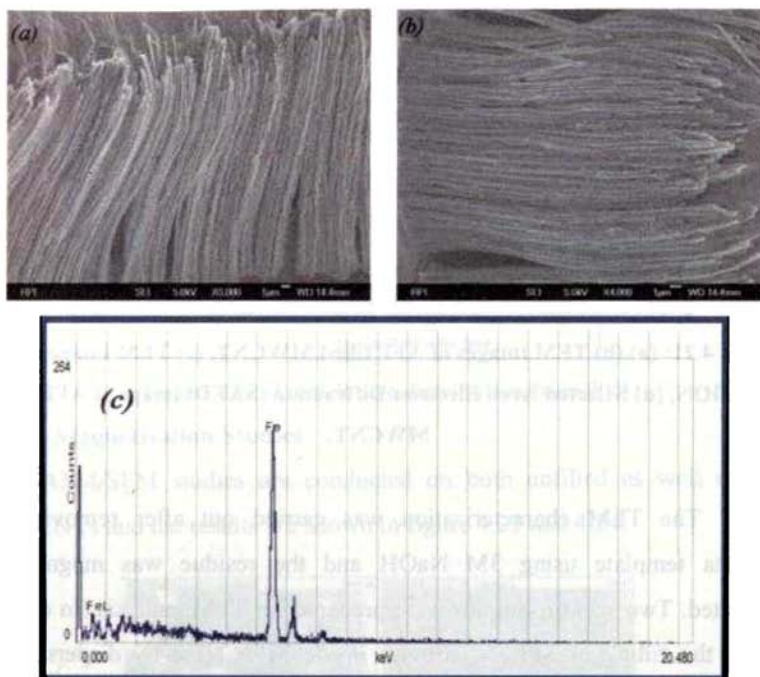
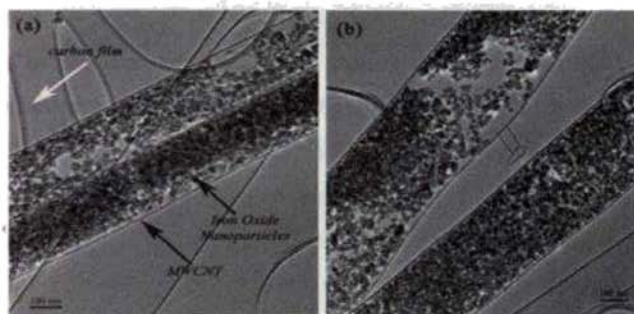


Figure 4.20 (a), (b) FESEM, (c) EDS images of AFF filled MWCNT.



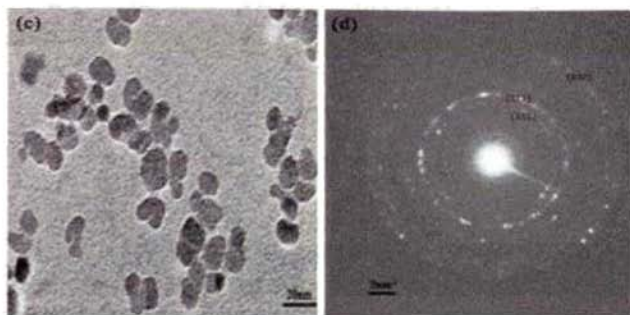


Figure 4.21: (a),(b) TEM images of AFF filled MWCNT, (c) TEM image of AFF of SPION, (d) Selected Area Electron Diffraction (SAED) image of AFF filled MWCNT.

The TEM characterization was carried out after removing the alumina template using 3M NaOH and the residue was magnetically separated. Two sets of samples were prepared for TEM analysis (in order to verify the filling of SPION particles inside MWCNTs) by dispersing the residue in ethanol and sonicating the residue for few minutes. This solution was drop casted over TEM copper grid. TEM images derived from two different parts (Figure 4.21.a. and Figure 4.21.b.) of the sample reveal filling of CNTs with FF. The average size of the SPIONs is found to be ~12nm (Figure 4.21.c). The SAED images (Figure 4.21.d) are indicative of superimposition of several planes. They correspond to polycrystalline planes of graphite, (110) and (112), and nanocrystalline planes from iron oxide, (440). The size distribution of SPIONs is depicted in figure 4.22. The distribution is Gaussian and centred at ~11.7 nm.

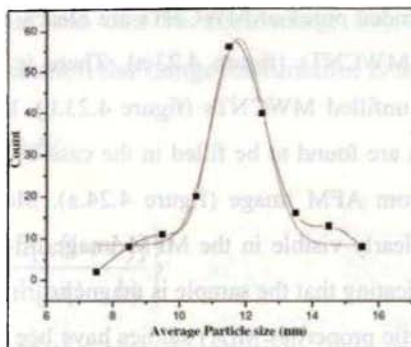


Figure 4.22: Particle size distribution from TEM.

4.5.3. Magnetisation Studies

The AFM/SFM studies are conducted on both unfilled as well as filled MWCNTs and the results are shown in figure 4.23 and 4.24.

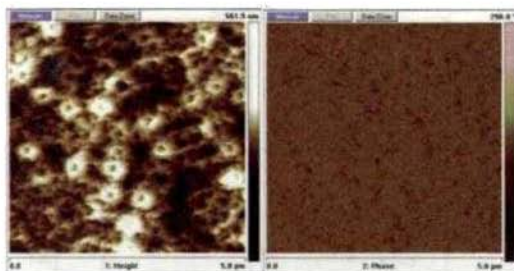


Figure 4.23: (a) AFM image of open ended MWCNTs (Left), (b) MFM image (Right).

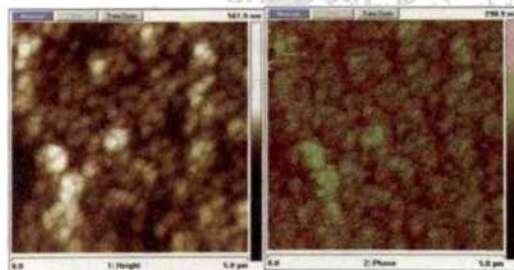


Figure 4.24: (a) AFM image of FF filled MWCNT (Left), (b) MFM image (Right).

The open ended pores of MWCNTs are clearly seen from the AFM image of unfilled MWCNTs (figure 4.23.a). There is no magnetic phase contrast visible in unfilled MWCNTs (figure 4.23.b). But, the open ended pores of MWCNTs are found to be filled in the case of FF filled MWCNTs as it is inferred from AFM image (figure 4.24.a). Moreover, a magnetic phase contrast is clearly visible in the MFM image of FF filled MWCNTs (figure 4.24.b), indicating that the sample is magnetic.

The magnetic properties $M(H)$ studies have been carried out using a SQUID magnetometer. Room temperature hysteresis loop of the composite is shown in Figure 4.25. Hysteresis loop is typical of a superparamagnetic material with near zero coercivity (H_c) and negligible remnance (M_r).

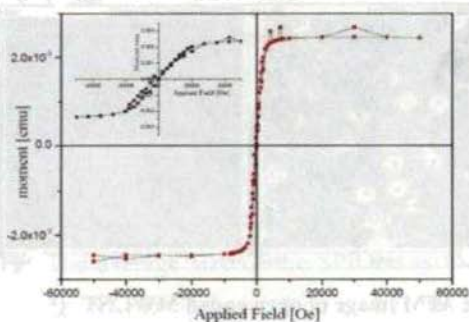


Figure 4.25: $M(H)$ curve for MWCNT-SPION composite at room temperature.

Fitting the Langevin function with the experimentally observed $M-H$ curve is considered as a sure test for superparamagnetism (SPM).

The Langevin function can be written as

$$L(x) = \coth x - \frac{1}{x} \quad 4.7$$

However, if due weightage is not given to the size distribution, this fitting can be erroneous and can be misleading. So, after providing due weightage for size distribution the Langevin function is modified as^[69]

$$L(x) = \frac{1}{2bx} \int_{x(1-b)}^{x(1+b)} L(x') dx' \quad 4.8$$

$$= \frac{1}{2bx} \ln \left\{ \frac{(1-b) \sinh[x(1+b)]}{(1+b) \sinh[x(1-b)]} \right\} \quad 4.9$$

where b is the width of the size distribution. This modified function in Equation 8 is used to simulate the magnetisation curve and is shown in Figure 4.26.

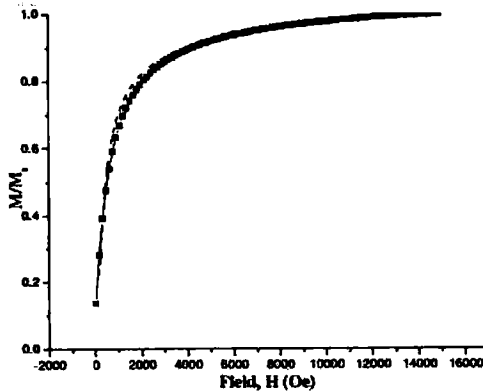


Figure 4.26: Langevin function fit (dotted line) to the experimental curve.

The function fit is in agreement and it reaffirms the fact that the MWCNT-SPION composite exhibits SPM. It is to be noted here that the magnetic response of AFF filled MWCNT originates from the SPIONs.

A better understanding of these spatially constrained SPION particles can be arrived at by a temperature dependent magnetisation study. The magnetisation of CNT-SPION composite is recorded at 6K and is

depicted in Figure 4.27. It is noteworthy that they exhibited enhanced coercivity (~150 Oe) and nonzero remanence.

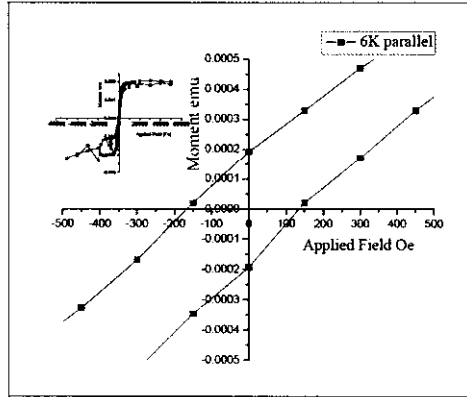


Figure 4.27: M(H) curve for MWCNT-SPION composite at 6K.

In order to probe the magnetic phase transitions emerging at low temperatures, Zero field cooling-Field cooling (ZFC-FC) measurements were carried out under an applied magnetic field of 300 Oe. The results are shown in Figure 4.28.a

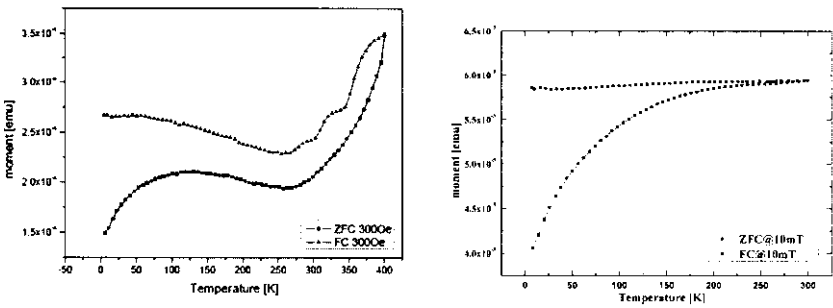


Figure 4.28: ZFC-FC curves for (a) MWCNT-SPION composite, (b) bare (CA coated) SPION.

ZFC curve shows a blocking behaviour^[70] at $\sim 110\text{K}$. The blocking temperature T_B is related to the size of the superparamagnetic particle by the relation,^[71]

$$KV=25k_B T$$

$$4.10$$

where $k_B T$ is the thermal energy, K anisotropy constant (for magnetite $1.35 \times 10^4 \text{Jm}^{-3}$) and V the volume of the particle. The blocking temperature T_B calculated for 12nm magnetite particles is $\sim 40\text{K}$. The deviation can be attributed to the clustering of SPION particles.^[72] TEM pictures also provide proof for clustering of SPION particles within MWCNT.

This implies that magnetic properties of an ensemble of single domain particles follows that of single particles and particle-particle interaction is not strong enough to prevent collective behaviour of the system at these temperatures.

It is to be noted here that FC and ZFC measurements carried out on these samples exhibit anomaly near room temperature. Above room temperature they show a ferromagnetic like behavior up to 400K. Here ZFC measurements were carried out by cooling the sample in zero field up to 6K and then moment is measured while warming in a field of 300 Oe. In FC measurements, the sample is cooled in a field of 300 Oe up to 6K and the moment is evaluated while warming upto a temperature $\sim 400\text{K}$. ZFC and FC possess different ground states and similar variation in ZFC and FC above room temperature indicates that the transition is reversible and intrinsic. This observation points to the fact that there is a ferromagnetic like moment ordering due to possible exchange interaction taking place between constrained superparamagnetic particles. Figure 4.28.b depicts the ZFC-FC curves for bare SPION at a lower field (100 Oe). Though there is a

bifurcation temperature higher than that of MWCNT-SPION (it is expected since the present experiment is carried out at lower magnetic field and hence the blocking will be shifted to higher temperatures^[73]), there is no increase in magnetisation at elevated temperatures. It is known that magnetic relaxation and blocking play a major role in fine particle system when they are randomly oriented.^[67] Once the temperature is increased above room temperature, thermal energy wins over the electrostatic polar repulsive energy between each nanoparticle, which keeps the particles away from agglomeration in the case of a ferrofluid. However, when the nanoparticles are constrained to small volumes, the role of interparticle interaction cannot be ignored and this may initiate an exchange interaction between the nanoparticles.

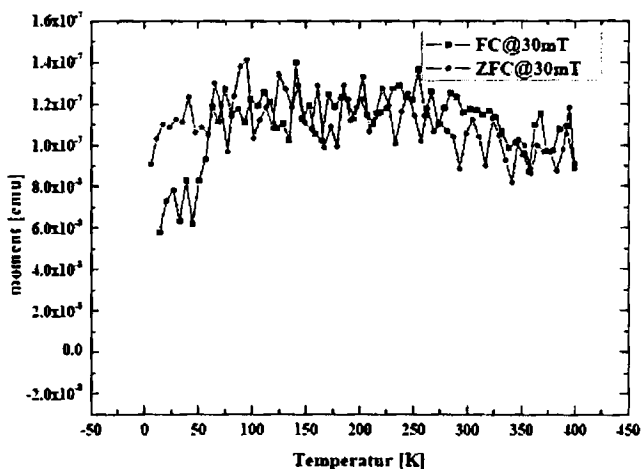


Figure 4.29: ZFC-FC curves for MWCNT.

Recently, immense interest has been shown on organic magnetism and induced magnetism in carbon nanotubes and lot of work, both in theoretical and experimental, are underway all around the world.^[74] In order to investigate any magnetic ordering in synthesised MWCNT's, ZFC-FC

measurements on bare MWCNTs are conducted. Figure 4.29 shows the ZFC-FC curve for bare MWCNT. ZFC-FC curves do not exhibit any magnetic phase transition indicating that the anomalous transition undergone in the case MWCNT-SPION composite is not emanated from MWCNT. In order to probe the origin of enhancement in magnetisation with temperature for MWCNT-SPION composite a detailed thermomagnetisation and field dependent studies are needed and will be carried out later.

Conclusion

MWCNT based various hybrid magnetic nanostructures of Nickel and Cobalt were fabricated using electrodeposition. The mobility assisted growth mechanism suggested for the growth of 1-D nanostructures inside AAO template is verified in the case of MWCNTs. A novel and high coercivity nanostructure called Co-in-Carbon nanotube has been synthesized using cobalt acetate as precursor for electrodeposition. Introduction of defects in MWCNTs by the addition of metals is studied using micro-Raman studies.

Microwave absorption properties of Ni filled MWCNTs are studied using cavity perturbation technique. Ni filled MWCNTs are found to be acting as a good electromagnetic absorber in the S band. They exhibited enhanced microwave absorption than bare MWCNTs and Ni NWs. Moreover, Ni filled MWCNTs exhibited better microwave absorption characteristics than that reported for Fe filled MWCNTs and they find applications as magnetodielectrics for microwave devices such as phase shifters, modulators and power absorbing terminals.

MWCNT-SPION composite was prepared by employing nanocapillarity of ferrofluids. Magnetisation studies of MWCNT-SPION conducted at room temperature and low temperature suggest that the embedded iron oxide nanoparticles exclusively contribute to the magnetic properties of the composite. Anomalous ZFC-FC curves exhibited by this

Synthesis and properties of...

system above room temperature are probably due to the enhanced interparticle exchange interaction. This kind of MWCNT-SPION composite can be envisaged as good agents for drug delivery and can be easily navigated through blood stream with augmented heating for hyperthermia.

References

1. Iijima, S. *Nature* (1991) 354 56.
2. Ebbesen, T. W.; Ajayan, P. M. *Nature* (1992) 358 220.
3. Baughman, R. H.; Zakhidov, A. A. de Heer, W. A. *Science* (2002) 297 787.
4. Rossi, M. P.; Ye, H. H.; Gogotsi, Y.; Babu, S.; Ndunga, P.; Bradley, J. C. *Nano Lett.* (2004) 4 989.
5. Tolles, W. M.; Rath, B. B. *Curr. Sci.* (2003) 85 1746.
6. Gogotsi, Y. *Mater. Res. Innovations* (2003) 7 192.
7. Lin, Y.; Taylor, S.; Li, H. P.; Fernando, K. A. S.; Qu, L. W.; Wang, W.; Gu, L, Zhou, B.; Sun, Y. P. *J. Mater. Chem.* (2004) 14 527.
8. Dresselhaus, M. S.; Dresselhaus, G.; Jorio, A. *Annu. Rev. Mater. Res.* (2004) 34 247.
9. Liu, Y.; Jiang, W.; Wang, Y.; Zhang, X. J.; Song, D.; Li, F. S. J. *Magn. Magn. Mater.* (2009) 321 408 412.
10. Ajayan, P. M.; Otto, Z. Z. *Applications of Carbon nanotubes* (2001) Dresselhaus, M. S.; Dresselhaus, G. Ph. Avouris (Eds.): *Carbon Nanotubes, Topics Appl. Phys.* 80 391.
11. Tyagi, P. K.; Singh M. K.; Misra, A.; Palntkar, U.; Misra, D. S.; Titus, E.; Ali, N.; Cbral, G.; Gracio, J.; Roy, M.; Kulshreshtha, S. K. *Thin Solid Films* (2004) 469 127.
12. Che, R. C.; Zhi, C. Y. ; Liang, C. Y.; Zhou, X. G. *Appl. Phys. Lett.*,(2006) 88 033105.
13. Wei, B. Q.; Shima, M.; Pati, R.; Nayak, S. K.; Singh, D. J.; Ma, R. Z.; Li, Y. B.; Bando, Y.; Nasu, S.; Ajayan, P. M. *Small*, (2001) 2 804.
14. Grobert, N.; Hsu, W. K.; Zhu, Y. Q.; Hare, J. P.; Krozo, H. W.; Walton, D. R. M. M. Terrones and H. Terrones, *Appl. Phys. Lett.*, (1999) 75 3363.
15. Govindaraj, A.; Satishkumar, B. C.; Nath, M.; Rao, C. N. R. *Chem. Mater.*, (2000) 12 202.
16. Ugarte, D.; Chatelain, A.; De Heer, W. A.; *Science* (1996) 274 1897.
17. Okuyama, F.; Hayashi, T.; Fujimoto, Y.; *J. Appl. Phys.* (1998) 84 1626.
18. Ajayan, P. M.; Colliex, C.; Lambert, J. M.; Bernier, P.; Tence. M.; Stephan, O. *Phys. Rev. Lett.* (1994) 72 1722.

19. Kiang, C-H. *Carbon* (2000) 38 1699.
20. Che, R. C.; Liang, C. G.; Shi, H. L.; Zhou, X. G.; Yang, X. A. *Nanotechnology* (2007) 18 355705.
21. Y. Lin, H. G. Zhou, H. F. Guo and L. F. Yu, *Materials Letters* (2007) 61.
22. Zhao, D-L; Li, X.; Shen, Z. M.; *Mater. Sci.and Eng. B* (2008) 150 105.
23. Terrones, M.; Grobert, N.; Hsu, W. K.; Zhu, Y. Q.; Hou, W. B.; Terrones, H; Hare, J. P.; Kroto, H. W.; Walton, D. R. M. *Mater. Res. Soc. Bull.* (1999) 24 43.
24. Monthioux, M. *Carbon* (2002) 40 1809.
25. Ajayan, P. M. *Prog.Crystal. Growth. Characterisation Mater.* (1997) 34 37.
26. Rao, C. N. R.; Sen, R.; Govindaraj, A. *Solid State Mater. Sci.* (1996) 1 279.
27. Ajayan, P. M.; Stephan, O.; Redlich, Ph.; Colliex, C. *Nature* (1995) 375 564.
28. Ajayan, P. M.; Iijima, S. *Nature* (1993) 361 333.
29. Seifu, D.; Hijji, Y.; Hirsch, G.; Karna, S. P. *J. Mag. Mag. Mat.* (2008) 320 312.
30. Tyagi, P. K.; Singh, M. K.; Misra, D. S. *Encyclopedia of Nanoscience and Nanotechnology*(2002) Nalwa, H. S. American Scientific Publishers: New York 3 417.
31. Tsang, S. C.; Chen, Y. K.; Harris, P. J. F.; Green, M. L. *Nature* (1994) 372 159.
32. Vasilios, G.; Vasilios, T.; Dimitrios, G.; Dimitrios, P. *Chem. Mater.* (2005) 17 1613.
33. Pederson, M. R.; Broughton, J. Q. *Phys. Rev. Lett.* (1992) 69 2689.
34. Korneva, G.; Ye, H.; Gogotsi, Y.; Halverson, D.; Friedman, G.; Bradley, J. C.; Konstantin, G. K. *Nano Lett.* (2005) 5 879.
35. Shaijumon, M. M.; Ou, F. S.; Ci, L.; Ajayan, P. M. *Chem. Commun.* (2008) 27 73.
36. Liu, Y. Q.; Gao; Sun, J. *Carbon* (2007) 45 1476.
37. Zhang, X. F.; Dong, X. L.; Huang, H.; Liu, Y. Y.; Wang, W. N.; Zhu, X. G.; Lv, B.; Lie, J. P. *Appl. Phys. Lett.* (2006) 89 053115.
38. Snoek, J. L. *Physica* (1948) 14 207.
39. Breger, V. B. *IEEE Trans. Magn.* (2004) 40 1679.

40. Zhang, X. F.; Dong, X. L.; Huang, H.; Lv, B.; Lie, J. P.; Choi, C. J. *J. Phys. D: Appl. Phys.* (2007) 40 5383.
41. Che, R. C.; Peng, L. M.; Duan, X. F.; Chen, Q. G.; Liang, X. L. *Adv. Mater.* (2004) 16 401.
42. Zheng, Z. G.; Xu, B.; Huang, L.; He, L.; Ni, X. M.; *Solid state sciences* (2008) 10 316.
43. Wadhawan, A.; Garrett, D.; Perez, J. M. *Appl. Phys. Lett.* (2003) 83 2683.
44. Watts, P. C. P.; Hsu, W-K.; Barnes, A. ; Chambers, B. *Adv. Mater.* (2003) 15 600.
45. Chen, X. D.; Wang, G. Q.; Duan, Y. P.; Liu, S. H. *J. Phys. D: Appl. Phys.* (2007) 40 1827 .
46. Wen, F. S.; Yi, H. B.; Qiao, L. G.; Zheng, H.G.; Zhou, D. G.; Li, F. *S. Appl. Phys. Lett.*(2008) 92 042507.
47. Choi Y C, Shin Y M, Lee B S, Park G S, Choi W B, Lee N S and Kim J M. *Appl. Phys. Lett.* (2000) 76 2367.
48. Werder, T.; Walther, J. H.; Jaffe, R. L.; Halicioglu, T.; Noca, F.; Koumoutsakos, P. *Nano Lett.* (2001) 1 697.
49. Kim, B. M.; Sinha, S.; Babu, H. H. *Nano Lett.* (2004) 4 2203.
50. Rosenweig, R. E. *Ferrohydrodynamics* (1985) Cambridge University Press: Cambridge pp 33.
51. Popplewell, J. *Phys. Technol.* (1984) 15 150.
52. Nair, S. S.; Thomas, J.; Sandeep, C. S. S.; Anantharaman, M. R.; Philip, R. *Appl. Phys.Lett.* (2008) 92 171908.
53. Bryant, H. C.; Sergatskov, D. A.; Debbie Lovato, Natalie L Adolpji, Richar, S.; Larson; Edward R Flynn. *Phys Med Biol.* (2007) 52 4009.
54. Gao, X. P.; Zhang, Y.; Chen, X.; Pan, G. L.; Yan, J.; Wu, F.; Yuan, H. T.; Song, D.Y. *Carbon* (2004) 42 47.
55. Ajayan, P. M. *Chem Rev.* (1999) 99 1787.
56. Singh, C.; Shaffer, M.; Kozoil, K.; Kinloch, I.; Wndle, A. *Chem. Phys. Lett.* (2003) 372 860.
57. Geng, J.; Singh, C.; Shephard, D.; Shaffer, M.; Johnson, B.; Windle, A. *Chem. Commun.* (2002) 22 2666.
58. Nielsch, K.; Castano, F. J.; Matthias, S.; Zee, W.; Ross, C. A. *Adv. Eng. Mater.* (2005) 7 217.
59. Fert, A.; Piraux, L. *J. Magn. Magn. Mater.* (1999) 200 338.

60. Dube, D. C.; Lanagan, M. T.; Kim, J. H.; Jang, S. J. *J. Appl. Phys.* (1988) 63 2466.
61. Ye, Y.; Sklyuyev, A.; Akyel, C.; Ciureanu, P. *IEEE Trans. Instrum. Meas.* (2007) 128.
62. Sklyuyev, A.; Ciureanu, M.; Akyel, C.; Ciureanu, P.; Menard, D.; Yelon, A. *IEEE CCECE* (2006) 1486.
63. Lucyszyn, S. *PIERS Online* (2008) 4 686.
64. Shi, S. L.; Liang, J. *Nanotechnology* (2008) 19 255707.
65. Chon, E. M.; Coloumb, P. *J. Mater. Sci.* (1996) 31 323.
66. C. G. Koops, *Phys. Rev.* (1951) 83 121.
67. Miles, P. A.; Westphal, W. B.; von Hippel, A. *Rev. Mod. Phys.* (1957) 29 279.
68. Chung, D. D. L. *Composite Materials: Science and Applications, Functional Materials for Modern Technologies*, (2003) Springer New York p. 93.
69. Chikazumi, S. *Physics of Magnetism* (1964) John Wiley & Sons Inc.: New York p.411.
70. Battle, X.; Labarta J. *Phys. D: Appl. Phys.* (2002) 35 R15.
71. Cullity B D *Introduction to Magnetic Materials* (1972) Addison-Wesley series in Metallurgy and Materials: Massachusetts p. 410.
72. Poddar, P.; Wilson, J. L.; Srikanth, H.; Morrison, S. A.; Carpenter, E. E. *Nanotechnology* (2004) 15 S570.
73. Anil Kumar, P. S.; Joy, P. A.; Date, S. K. *J. Phys.: Condens. Matter.* (1998) 10 L487.
74. Zhang, Y.; Talapatra, S.; Kar, S.; Vajtaj, R.; Nayak, S. K.; Ajayan, P. M. *Phys. Rev. Lett.* (2007) 99 107201.

Chapter 5

Evaluation of Non-linear Optical Properties of Magnetic Nanostructures and Carbon Nanotube based Hybrid Structures

This chapter discusses the salient results obtained from the open aperture z-scan studies conducted on magnetic nanowires, nanotubes and their hybrid structures with MWCNTs. In the beginning, a brief introduction to nonlinear optics has been provided with special emphasis on nonlinear absorption properties. Optical limiters are one class of the nonlinear optical materials, which have potential applications in the protection of sensitive optical detectors and human eyes from accidental exposure to intense light beams. Non-linear transmission properties of Ni and Co NWs/NTs and that of MWCNTs are carried out. Non-linear transmission behavior of MWCNTs and MWCNT based magnetic composites of Ni and Co are also subjected to investigations using z-scan technique and their results are compared. In comparison to the benchmark carbon nanotubes, these composite materials show an enhanced nonlinear optical absorption. Cobalt-in-carbon nanotubes are found to exhibit an interesting transmission behavior, where effective two-photon and three-photon absorption nonlinearities are present simultaneously. The experimental results are in good agreement with theory when fitted numerically to the appropriate expressions for nonlinear transmission. Nonlinear parameters namely order of nonlinearity and nonlinear absorption coefficient are calculated from the data show that these materials are efficient optical limiters. To our knowledge this is the first discussion where the optical limiting properties of metal nanotubes are compared to those of carbon nanotubes.

**A part of the work discussed in this chapter has been published in "Nanotechnology"(2009, 20, 285702).*

5.1 Introduction

In 1960s, 'Laser' was a 'solution looking a problem' but nowadays it is an inseparable part of various fields such as medicine, research, supermarkets, entertainment, industry, military, communication, art and information technology. The intense laser beam can easily damage the sensitive optical instruments, particularly human eye and thus protection from lasers is not only a scientific subject but also a potential public safety issue.^[1] The field of non-linear optics (NLO) addresses this issue successfully and the emergence of this field happened shortly after the first demonstration of second harmonic generation by Peter Franken et al. in 1961.^[2] Since then, NLO has burgeoned in to a mature field of science and engineering.

An alternating electric field applied to an atom will result in the oscillation of the electrons with the same frequency. If the electric field vector of the exciting radiation is weak, the electron oscillation is simple harmonic and the induced polarization of the materials has a linear dependence on the field amplitude, $P = \chi^1 E$. Here, χ^1 is the linear susceptibility and E is the amplitude of the electric field vector of the exciting electromagnetic radiation. χ^1 is a second rank tensor and is responsible for the usually observed optical properties like the linear refractive index (n_0) and absorption coefficient (α_0) of the medium. The refractive index, dielectric constant and linear susceptibility of the medium are related by, $\epsilon = n_0^2 = 1 + \chi^{(1)}$.

When the intensity of the incident light to a material increases, the response of the system is no-longer linear. This is due to the fact that electron response of the system becomes anharmonic to the applied light field. The magnitude of the nonlinearity will depend up on the applied field intensity and the nonlinear susceptibility coefficient χ . In this case, polarization will depend on higher powers of electric field as,

$P = \chi^1 E + \chi^2 EE + \chi^3 EEE$ (nonlinearities of still higher order are not significant since the corresponding susceptibility coefficients progressively drop in their values rapidly), where χ^2 and χ^3 are second order (third rank tensor) and third order (fourth rank tensor) nonlinear susceptibilities respectively. It is possible to show from symmetry considerations that media with inversion symmetry (isotropic media like solutions) lack nonlinearities of even order while those lacking inversion symmetry (like anisotropic crystals) can display both even and odd order nonlinearities.^[3]

In linear optics, the optical properties of the medium are independent of light intensity, while in the nonlinear optics the optical properties like refractive index and absorption coefficient change with light intensity. Various nonlinear optical effects will see in a material depending upon the order of nonlinearity present. Moreover, all the allowed nonlinear phenomena will not occur simultaneously in any given nonlinear medium and by a careful choice of the experimental conditions, it is possible to maximize any given nonlinearity of interest, while minimizing or nullifying the other nonlinearities.

In the present study, all the 1-D nanostructures investigated for their optical nonlinearity were taken in the form of isotropic dispersions in appropriate solvents and hence the nonlinearity of third order is needed to be investigated. Before going to the details of the present investigation, optical nonlinearities in nanostructured materials and different mechanisms contributing to the optical nonlinearity are discussed with a special emphasis to third order nonlinearity.

5.2 Third order nonlinearity

In a third order nonlinear medium (example: isotropic solutions), the real and imaginary part of the χ^3 are related to the nonlinear refraction and nonlinear absorption respectively by the relations,

$$\text{Real part of } \chi^3 = 10^{-6} c n_0^2 n_2 / 480 \pi^2 \quad 5.1$$

$$\text{Imaginary part of } \chi^3 = 10^{-7} c^2 n_0^2 \beta / 96 \pi^2 \omega \quad 5.2$$

where c is the velocity of light (in cm s^{-1}), n_0 is the linear refractive index, ω is the laser radiation frequency in Hz, β is the nonlinear absorption coefficient (in cm W^{-1}), and n_2 is the nonlinear refractive index in $\text{cm}^2 \text{W}^{-1}$.

The refractive index of the medium is given by the relation,

$$n = n_0 + n_2 I \quad 5.3$$

where I is the laser intensity. The absorption coefficient is given by

$$\alpha = \alpha_0 + \beta I \quad 5.4$$

where α_0 is the linear absorption coefficient, and β is the nonlinear absorption coefficient.

The propagation equation for light travelling in the z direction through a third order nonlinear medium can be written as,

$$dI/dz = -(\alpha_0 + \beta I)I \quad 5.5$$

Depending on the sign of n_2 and β , the modification of the refractive index will give rise to self-focussing or defocusing effects and modification in the absorption coefficient will lead to induced transmission or absorption.^[4-5]

5.3 Measurement of optical nonlinearity

The absolute measurement of the optical nonlinearity is not easy since the experimental parameters have to be measured with very high precision. The relative measurements of optical nonlinearity using a reference material of known optical nonlinearity are the usual method which simplifies the experiment considerably. The 'Kurtz powder technique' is the common method adopted for the measurement of second order nonlinearities in crystals. Ammonium dihydrogen phosphate and potassium dihydrogen phosphate are two standards used as reference to determine second order nonlinearities.

The usual methods adopted for third order nonlinearities are z-scan technique and Degenerate Four Wave Mixing (DFWM). DFWM is a relative measurement and usually carried out using standard reference like CS₂. Z-scan is an absolute measurement and can be used to measure both nonlinear refractive index and nonlinear absorption.

In a z-scan measurement, a gaussian laser beam is focused by a convex lens to a narrow waist (Figure 5.1). The sample to be measured is then moved along the beam propagation direction (z-axis) using a translation stage. At each z position, the sample transmission is measured using a detector and at each position, the beam size will be different, and hence the laser intensity. The laser intensity will be maximum at the focal point and will reduce to either direction.

In a z-scan measurement, the nonlinear absorption and nonlinear refraction of a medium are separately measured. There are two types of z-scan measurements depending up on the experimental set up; open aperture z-scan and closed aperture z-scan. In a closed aperture z-scan an aperture is placed in front of the detector (PD1 in the figure 5.1) while in an open aperture z-scan no aperture is used (figure 5.1). A plot of the transmission as

a function of sample position is then made. If the sample has no measurable nonlinearity, a flat line will be obtained, otherwise the transmission as a function of sample position will not be linear. Results from closed aperture configuration will provide information about the real part of the nonlinearity, that is nonlinear refractive index and from open aperture configuration information on the imaginary part (nonlinear absorption) will be obtained.

5.4 Optical nonlinearity in nanostructured materials

The successful fabrication and use of photonic devices depends upon the availability of good nonlinear optical materials. Over the years various materials such as inorganics, organics, organometallics and semiconductors have been studied for their nonlinear optical properties.^[6-11] Recently, interest in the field of photonic devices has surged due to the advent of nano particles and nano structures. Nanotubes and nanowires are attractive in this regard, as they possess a unique one-dimensional physical geometry.^[12-13] These one-dimensional nano materials are found to have a characteristic behavior in the optical as well as in the electrical regimes, arising from their peculiar geometry.^[14-15] For instance, a number of authors have reported optical nonlinearities in carbon nanotubes.^[12-13, 16-21] The expertise gained in the bulk production of carbon nanotubes^[22] attracted the attention of scientific community for fabricating nanotubes and nanowires of various other inorganic materials, which are also found to possess many features similar to those of the CNTs. Nanotubes in general have high thermal and chemical stability, along with high electrical conductivity and a fast optical nonlinearity.

Carbon nanotubes can be suitably functionalised to serve as versatile one-dimensional nanostructures for various optical limiting applications. This is abundantly evident from the vast literature reports available on this topic of research. Wang and Blau highlighted the optical limiting properties

of various hybrid nanostructures and CNT based composites in a recent review article.^[1] In the recent past strong optical limiting has been observed in metal nanowires synthesized from cobalt, manganese, silver, gold and nickel,^[23-24] and their optical limiting was compared to those of single walled and multiwalled carbon nanotubes (SWCNT and MWCNT respectively). In the present investigation, all the samples are synthesized and measured in the nanotube/nanowire forms, and to the best of our knowledge this is the first study where optical limiting properties of metal nanotubes are compared to those of carbon nanotubes. Such a comparison is more appropriate, as these tubular structures will induce similar kind of geometrical field distortion in the incident electromagnetic radiation.

Mechanisms such as nonlinear scattering, two photon or three photon absorption, and reverse saturable absorption phenomena including free carrier and excited state absorption are thought to be responsible for optical limiting. Moreover, possibility for the simultaneous occurrence of different mechanisms in the same system giving rise to strong optical limiting properties cannot be ruled out.

5.4.1 Mechanisms

The physical and photophysical properties of a material system such as absorption band, particle size, geometry, aggregation state and the properties of the host matrix have a strong influence on its optical limiting performance. Various nanomaterials exhibit distinct nonlinear responses for laser sources with different parameters, including wavelength, pulse duration, and repetition rate.^[1] Different mechanisms for optical limiting, associated with the effects of the material and laser parameters are discussed below.

5.4.1.1 Nonlinear scattering

Nonlinear scattering (NLS) is the most common nonlinear phenomenon for nanomaterials. The scattering process can disperse the highly intense beam in to a larger spatial dimension and hence reduce the intensity of the direct incident beam. According to Mie scattering theory, nanoparticles alone can not scatter a light beam effectively. The effective scattering arises from the formation of scattering centres, initiating from nanoparticles, has three possible origins.

The first possibility is the formation of solvent bubbles due to the absorption of incident photon energy by the nanoparticles and subsequent transfer of thermal energy to the surrounding solvent. This will cause the evaporation of solvent and resulting in the formation of bubbles. Due to the refractive index discontinuity at the vapour-solvent interface, the vapour bubbles can scatter effectively. This is prominent in nanosecond laser excitation, because evaporation time is also of the order of nanosecond.

The second origin of the scattering centres in the case of nanoparticles is from the evaporation of nanoparticles itself. In the case of metal nanoparticles, if the wavelength of the incident beam is in the surface plasmon absorption band of metal particles, where strong photon absorption will take place. This process can form microplasma states in the solution, and hence serve as scattering centres. Also in some nanomaterials systems the two mechanisms can coexist, giving rise to strong optical limiting.

The third type of scattering centre formation can take place due to the variation of the refractive index of the surrounding solvents or the interface between the particles and the surrounding liquid. Such a dielectric with a refractive index discontinuity or mismatch, forming in the nanosecond region can act also as scattering centres.

5.4.1.2 Multiphoton absorption

A multi-photon absorption is a process in which simultaneous absorption of two or more photons occur via virtual states in a medium. The two photon absorption (TPA) can be described by a propagation equation with 'Beer-Lambert' format as $\frac{\partial I}{\partial z} = -(\alpha + \beta I)I$. Provided that the linear absorption is very small at lower intensity, the solution for transmission intensity is given by $I(L) = \frac{I_0}{(1 + I_0 \beta L)}$. This solution indicates that the transmission intensity decreases as the incident intensity increases, resulting in to an optical limiting phenomenon. The ability of TPA induced optical limiting strongly depend upon the TPA coefficient, incident intensity and propagation length. The optical limiting characteristics of TPA materials is more effective for shorter pulses (femto second). The three photon process also exhibits very similar characteristics.

Multiphoton process can not easily be identified from z-scan technique. One has to utilise the photophysical properties of a materials such as linear absorption, TPA cross section, etc. to determine the contribution of multiphoton absorption.

5.4.1.3 Free-carrier absorption

In semiconductors, carriers can be generated by one-photon or two-photon excitation. These electron/hole pairs, by absorbing additional photons, can be excited to states higher/lower in the conduction/valence band. This process is known as 'Free carrier absorption' (FCA). Semiconductors with large FCA cross section can exhibit significant optical limiting effects. The FCA induced NLO response is independent of the incident pulse duration, provided that the duration is shorter than the diffusion and recombination process of free carriers. FCA is also insensitive to the particle geometry and

size. In many nanomaterials, FCA can coexist with NLS and TPA since the generation of free carriers can arise from a TPA process.

5.4.1.4 Reverse saturable absorption

In a molecular system, reverse saturable absorption (RSA) occurs when the excited state absorption cross section is greater than that of the ground state, resulting in a improved absorption capability to incident fluence. For inorganic nanomaterials, the term RSA is accepted to describe the situation where the excited state absorption (ESA) outperforms the ground state absorption, leading to a decrease in the transmission with increase in incident intensity.

5.5 Experiment

In the z-scan technique, the laser beam is focused using a lens, and the sample is moved along the beam axis (z-axis) from one side of the focus to the other, through the focal point (which is taken as $z = 0$). In this scheme each z position corresponds to an input fluence of $4\sqrt{\ln 2}E_{in}/\pi^{3/2}\omega_{(z)}^2$, where E_{in} is the input laser pulse energy, $\omega(z)$ is the beam radius given by $\omega_0\sqrt{1+(z/z_0)^2}$ where $\omega(0)$ is the beam radius at the focus, and $z_0 = \pi\omega_0^2/\lambda$ is the Rayleigh range (diffraction length). The z-scan^[23] measurements using a frequency doubled Q-Switched Nd:YAG laser (Quanta Ray, Spectra Physics) having a nominal pulse width of 7 ns at 532 nm wavelength.

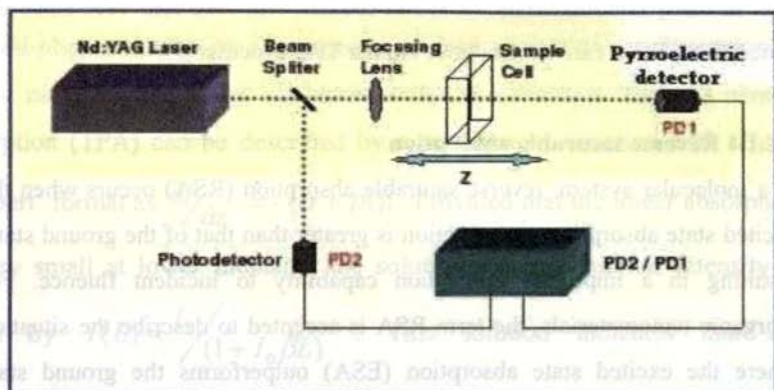


Figure 5.1: Schematic of open aperture z-scan technique.

The laser is focused using a plano-convex lens of 20 cm focal length, and the focal spot radius (ω_0) is 18 microns. The laser pulse energy is 25 microjoules. The peak optical intensity seen by the sample at the beam focus is of the order of 10^{12} Wm^{-2} . The nanotube/nanowire samples are dissolved in a mixture of toluene and ethanol (in the ratio 2:1) and then sonicated for 10 minutes for uniform dispersion. They are then taken in a 1 mm glass cuvette which is mounted on a stepper motor controlled linear translation stage. All samples are prepared at low concentrations such that their linear transmission was 85% at 532 nm, when taken in the 1 mm pathlength cuvette. The sample thickness is lesser than the Rayleigh range (1.9 mm). The sample was translated in the z direction in small steps, and the transmitted energy was measured for each position z using a pyroelectric laser energy detector (Laser Probe Inc.). The experiment is automated such that laser pulses could be generated on demand. The interval between two successive laser pulses is always kept sufficiently large (typically more than 1 s), to enable the complete thermal relaxation of the sample before the arrival of the following pulse.

5.5 Result and discussion

5.5.1 z-scan studies on MWCNTs, Co NTs and cobalt-in-carbon nanotube hybrid structures

Initially, the z-scan studies are carried out on the solvent (mixture of toluene and ethanol in 2:1 ratio) and z-scan curve is plotted in figure 5.2.

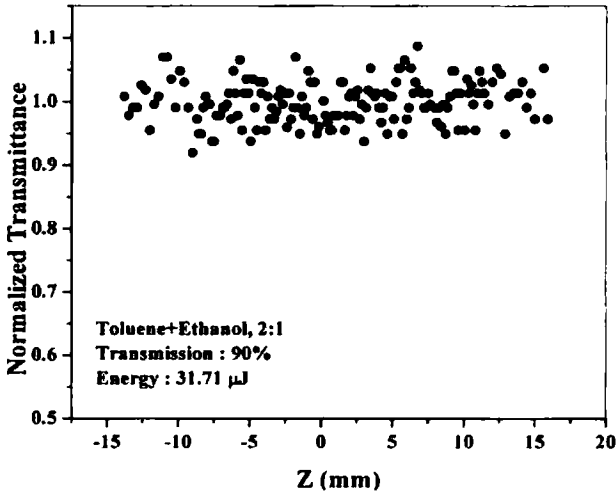


Figure 5.2: z-scan curve for the mixture solution of toluene and ethanol (2:1 ratio).

It is to be concluded from the figure 5.2 that there is no considerable optical nonlinearity in the mixture solution (as mentioned before, a flat z-scan curve denote the absence of any nonlinearity).

Z-scan studies were conducted on high aspect ratio MWCNTs after removing them from alumina template (Figure 5.3). The z-scan curve is depicted in figure 5.3 (inset). It represents a strong optical limiting behaviour. The curves are best fitted using a 2PA process using the equation,

$$T = \left(\frac{(1-R)^2 \exp(-\alpha_0 L)}{\sqrt{\pi q_0}} \right) \int_{-\infty}^{+\infty} \ln[\sqrt{1 + q_0 \exp(-t^2)}] dt \quad 5.6$$

where L and R are the sample length and surface reflectivity respectively, and α_0 is the linear absorption coefficient. q_0 is given by $\beta(1-R)I_z L_{eff}$, where β is the two photon absorption coefficient, and I_z is the intensity of the laser beam at position z . L_{eff} is given by $[1 - \exp(-\alpha_0 L)] / \alpha_0$. Here we are assuming that $R=0$ for simplicity, $I = \text{Fluence} / \text{time} = \text{Energy} / \text{Area} / \text{time}$. Fluence, $F = \text{Energy} / \text{Area} = 2E / \pi r^2$, and for a Gaussian wave, $r = \omega_z$.

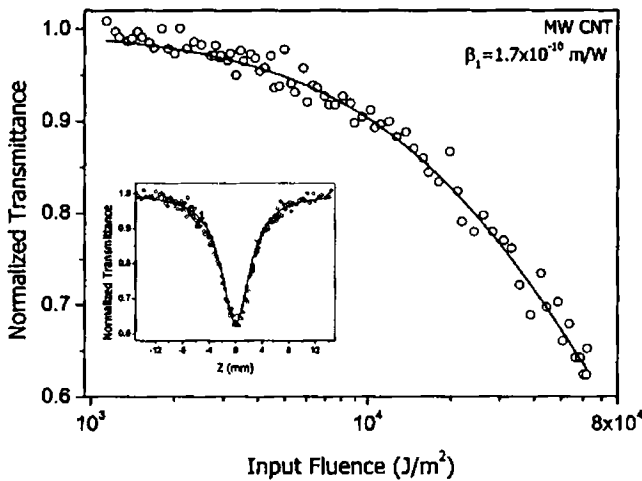


Figure 5.3: Nonlinear transmission in MWCNTs under 532 nm, 7 ns laser irradiation. (The inset gives the open aperture z-scan curve. Hollow circles are experimental data points and solid line is a numerical fit to the data for an effective 2PA process).

Figure 5.3 indicates that the observed limiting properties are well fitted to a 2PA. This is further confirmed by plotting the log-log plot of $\langle \Delta \alpha \rangle$ versus input fluence for MWCNTs and is depicted in figure 5.4.

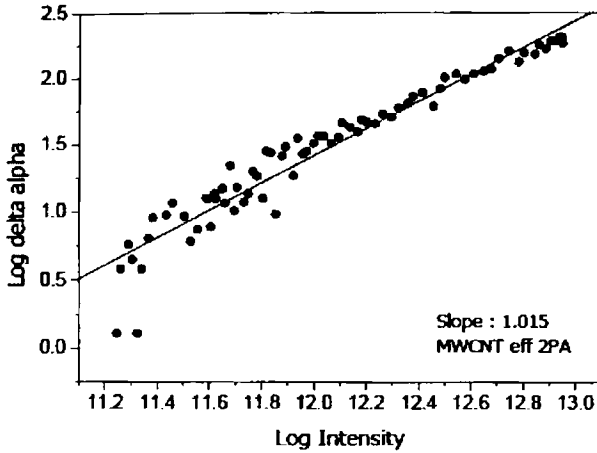


Figure 5.4: log-log plot of $\langle \delta \alpha \rangle$ vs input fluence for MWCNTs.

The plot has a slope of 1.01, which is close to that of 2PA and for which it is expected to be 1. z-scan plot for Co NTs (FESEM image: Figure 3.12) is conducted and is shown in figure 5.5.

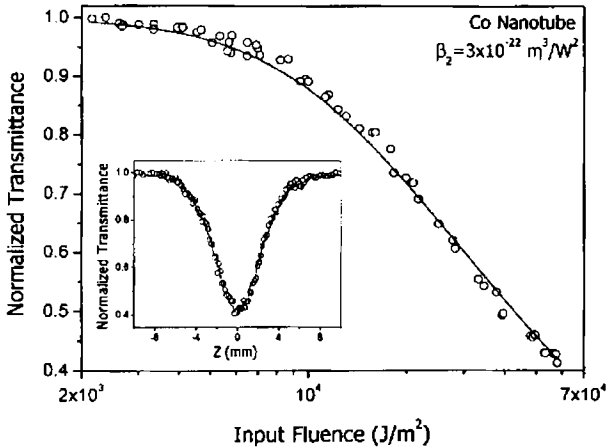


Figure 5.5: Nonlinear transmission in Co NTs under 532 nm, 7 ns laser irradiation. (The inset gives the open aperture z-scan curve. Hollow circles are experimental data points and solid line is a numerical fit to the data for an effective 3PA process).

The z-scan curve is depicted in figure 5.4 (inset). It represents a strong optical limiting behaviour. The curves are best fitted using a 3PA process using the equation,

$$T = \frac{(1-R)^2 \exp(-\alpha_0 L)}{\sqrt{\pi} p_0} \int_{-\infty}^{\infty} (\ln[\sqrt{1 + p_0^2 \exp(-2t^2)}] + p_0 \exp(-t^2)) dt$$

5.7

p_0 is given by $[2\gamma(1-R)^2 I_c^2 L_{eff}]^{1/2}$, where γ is the three photon absorption coefficient, and $L_{eff} = [1 - \exp(-2\alpha_0 L)] / 2\alpha_0$.

Figure 5.5 indicates that the observed limiting properties are well fitted to a 3PA. As done in the case of MWCNTs, this is further confirmed by plotting the log-log plot of $\langle \Delta \alpha \rangle$ versus input fluence for Co NTs and is depicted in figure 5.6.

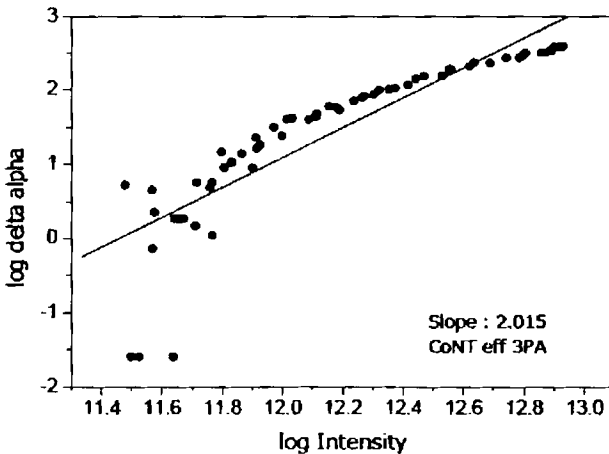


Figure 5.6: log-log plot of $\langle \Delta \alpha \rangle$ vs input fluence for Co NTs.

The plot has a slope of 2.015, which is close that for a 3PA and it is expected to be 2.

In the case of carbon nanotube samples optical limiting is reported to have contributions from two-photon absorption (2PA) and nonlinear scattering.^[18] In metal nanoparticle systems contributions from interband transitions and free carrier absorption have been noticed, and the net nonlinearity sometimes appears in the form of an “effective” three-photon absorption (3PA) phenomenon.^[26] In a pure 2PA process two photons will be simultaneously absorbed while in a pure 3PA process three photons will be simultaneously absorbed, and both these are instantaneous nonlinear optical phenomena. Compared to the usual one-photon absorption process the cross sections of these phenomena are generally low, but they become significant when the samples are irradiated with intense laser pulses of picoseconds or shorter duration. With nanosecond pulse excitation accumulative nonlinear optical phenomena like excited state absorption and free carrier absorption become more prominent. Depending on the material system under study, excitation wavelength and applied laser fluence, a combination of the instantaneous and accumulative nonlinear effects may take place. These, however, will appear like pure 2PA or pure 3PA in a simple transmission measurement like the z-scan. These combined nonlinearities can hence be termed as “effective 2PA” and “effective 3PA” processes to distinguish them from pure 2PA and 3PA processes. Time-resolved pump-probed experiments are required to distinguish between instantaneous and accumulative nonlinearities, and the conventional z-scan can throw light only on the order and magnitude of the nonlinearity.

Z-scan studies are also carried out on cobalt-in-carbon nanotube hybrid structures. But, in the Cobalt-in-carbon nanotube samples the data does not fit well either to an effective 2PA or an effective 3PA process: rather, it fits to an intermediate order of nonlinearity (figure 5.7).

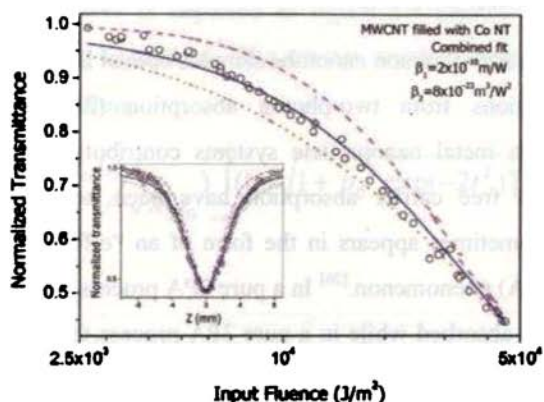


Figure 5.7: Nonlinear transmission in cobalt-in-carbon nanotube under 532 nm, 7 ns laser irradiation. (The inset gives the open aperture z-scan curve. Hollow circles are experimental data points. The dotted curve is the best 2PA fit and the dashed curve is the best 3PA fit. The solid curve (blue) shows the best fit data obtained by assuming the simultaneous occurrence of effective 2PA and effective 3PA phenomena).

The intermediate behaviour is further verified by plotting log-log plot of $\langle \Delta \alpha \rangle$ versus input fluence (figure 5.8).

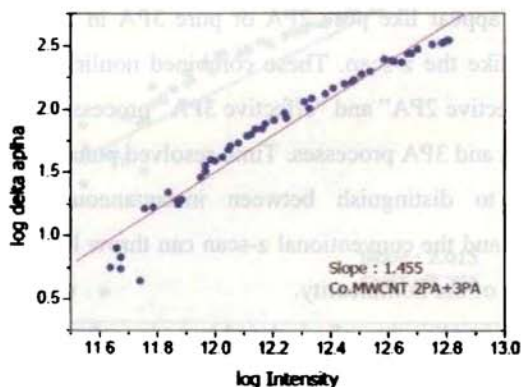


Figure 5.8: log-log plot of $\langle \Delta \alpha \rangle$ vs input fluence for cobalt-in-carbon nanotubes.

The plot has a slope of 1.45, while the expected slope for an intermediate behaviour is in between 1 and 2. For calculating these fits numerically the generalized z-scan equations given by Bing Gu et al. are used.^[27] The intensity of a focused gaussian beam travelling along +z direction (assuming $z = 0$ to be the focal point) can be written as,

$$I(r, x) = I_0 \frac{1}{1+x^2} \exp\left(\frac{-2r^2}{\omega^2(x)}\right) \quad 5.8$$

where I_0 is the on-axis peak intensity and $x = z/z_0$ is the relative position with respect to the beam focus, where z_0 is the diffraction length (Rayleigh range). $\omega(x) = \sqrt{\omega_0^2(1+x^2)}$ is the beam radius. If this gaussian beam passes through a thin sample of length L ($L \ll z_0$), having linear absorption coefficient α_0 and $(n+1)$ photon absorption coefficient β_n ($n \geq 1$ where n is an integer), then the propagation equation can be written as

$$\frac{dI}{dz'} = -(\alpha_0 + \beta_n I^n) I \quad 5.9$$

where z' is the propagation length inside the sample. The transmitted intensity is given by

$$I(L, x) = I(r, x) \exp(-\alpha_0 L) / (1 + n\beta_n I^n(r, x) L_{eff}^{(n)})^{1/n} \quad 5.10$$

where $L_{eff}^{(n)} = [1 - \exp(-n\alpha_0 L)] / n\alpha_0$ is the effective sample length for the $(n+1)^{th}$ photon absorption process. The normalized transmittance of the sample from an open aperture z scan, for an $(n+1)$ photon absorption process, can then be written as

$$T_{n+1}(x, \Psi_n) = \frac{\int_0^{\infty} 2\pi I(L, x) r dr}{\exp(-\alpha_0 L) \int_0^{\infty} 2\pi I(r, x) r dr} \quad 5.11$$

Here $\Psi_n = (n\beta_n I_0^n L_{\text{eff}}^{(n)})^{1/n}$. For 2PA the normalized transmittance simplifies to

$$T_2(x, \Psi_1) = \frac{\ln(1 + \psi_1)}{\psi_1} \quad 5.12$$

and for 3PA it becomes

$$T_3(x, \Psi_2) = \frac{\sinh^{-1}(\psi_2)}{\psi_2} \quad 5.13$$

where $\psi_n = \frac{\Psi_n}{1+x^2}$. The normalized open aperture z-scan transmittance of a nonlinear medium with simultaneous 2PA and 3PA can then be written as

$$T(x, \Psi_1, \Psi_2) = T_2(x, \Psi_1) T_3(x, \Psi_2) f(x, \Psi_1, \Psi_2) \quad 5.14$$

where $f(x, \Psi_1, \Psi_2)$ is a coupling function between the 2PA and 3PA coefficients. From numerical calculations, it is found to be approximately given by²⁴

$$f(x, \Psi_1, \Psi_2) = 1 + \frac{\psi_1 [0.339 \sin(0.498\psi_2) - 0.029]}{1 + 0.966\psi_1\psi_2^{-0.718}} \quad 5.15$$

The calculated 2PA coefficient (β_1) is 1.7×10^{-10} m/W for the MWCNT samples, while the 3PA coefficient (β_2) is 3×10^{-22} m³/W² for the

cobalt nanotubes. Cobalt-in-carbon nanotubes show a mixed behavior, and the calculated β_1 is 2×10^{-10} m/W and β_2 is 8×10^{-23} m³/W² respectively. The origin of the observed nonlinear absorption can be explained from the absorption spectra of the samples given in Figure 5.9. The UV-Vis absorption spectra of the samples are measured by dispersing these samples in a mixture of toluene:ethanol (in 2:1 ratio) using a Perkin-Elmer Lambda 35 spectrophotometer. 1 mm quartz cuvette is used for holding the solution. The solvent absorption is not subtracted from the spectra.

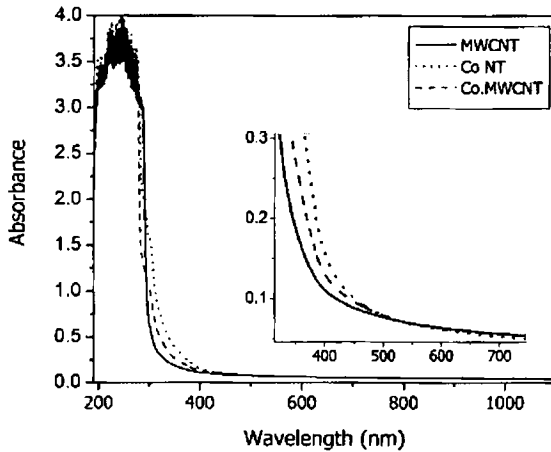


Figure 5.9: UV-VIS absorption spectra of the MWCNT, Cobalt nanotube and the Cobalt nanotube filled MWCNT samples.

From the inset we see that there is some absorption at 532 nm, complementing the linear transmission of 83% of the samples. The absorption is much stronger at the two-photon wavelength of 266 nm. Obviously this absorption spectrum allows one-photon, two-photon, and two-step absorptions to take place at 532 nm (since the spectrophotometer has a lower wavelength limit of 190 nm we could not measure the absorption

at the three-photon wavelength of 177 nm). As the samples are metallic in nature, there is a high probability of additional photon absorption from the terminal level reached by the two-photon and two-step transitions. It may also be noted that the photoelectric work function of Co is 5 eV, and this energy will be given and exceeded by three 532 nm photons ($3 \times 2.33 \text{ eV} = 6.99 \text{ eV}$). The nature of the absorption spectra thus explains the observation of effective 2PA, effective 3PA like, and the intermediary type nonlinear absorption exhibited by the samples.

In general, the optical limiting mechanism in MWCNTs can be expected to have a contribution from induced thermal scattering (also known as nonlinear scattering), due to the similarities in optical limiting with the well known carbon black suspensions.^[28] The general model for the fluence based limiting in carbon nanotubes due to nonlinear scattering can be summarized as follows: the thermal energy from laser absorption is transferred to the surrounding solvent medium resulting in the formation of micro plasmas at lower fluence levels. An increase in the fluence results in the desorption of oxygen and amorphous carbon, and increasing the fluence further leads to localized heating and eventually the ionization of MWCNTs, forming rapidly expanding microsized plasmas.²⁶ Since more heat is transferred to the solvents at this stage, more micro bubbles are also created. These micro bubbles and the micro plasmas formed at the focal regions will strongly scatter the input radiation from its normal transmission path, thereby resulting in a nonlinear decrease in the measured transmitted light. However, the highly transparent samples absorb only a small fraction of the input light in the present case, and the effects of induced thermal scattering have to be minimal. Nevertheless, we found that the absorption is still sufficient to cause some beam scattering when the samples are at or near the focal point during the z-scan. A third detector is used - a sensitive

photodiode - to gather a part of this scattered radiation. The photodiode was mounted on the translation stage itself facing the sample, at an angle of 40 degrees to the forward laser beam direction. The results are shown in Figure 5.10.

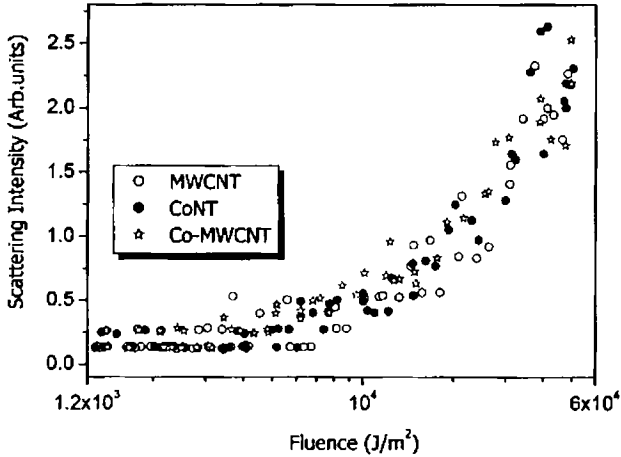


Figure 5.10: Nonlinear scattering from the samples measured using a photodiode.

Scattering increases as the sample reaches the focus, but this does not affect the cross-sectional quality of the central bright spot, when observed on a white screen (observed using a CCD camera). This indicates that the effect of nonlinear scattering is not significant compared to that of nonlinear absorption, at the present sample concentrations used.

5.5.1.2 Theory of log-log plot

It is well known that in any sample, under normal condition, transmission of a sample is given by Beer-Lambert's law,

$$T = \exp(-\alpha_0 L) \quad 5.16$$

Here α_0 is the linear absorption coefficient. For a 2PA case,

$$\frac{dI}{dz} = \alpha_0 I - \beta I^2 \quad 5.17$$

Or in other words we can write the transmission in terms of a new α_1 , which is equivalent to $\alpha_0 + \beta I$. Hence for a 2PA case,

$$T = \exp(-\alpha_1 L) \quad 5.18$$

Since we know the Transmission and length of the sample, α_1 can be calculated from the above equation. Now since we know $\alpha_1 = \alpha_0 + \beta I$, $\alpha_1 - \alpha_0 = \beta I$. taking logarithm on both sides,

$$\ln(\alpha_1 - \alpha_0) = \ln \beta + \ln I \quad 5.19$$

here $\log \beta$ is a constant, and this is the equation of a straight line ($y=mx+c$). Hence a plot between $\log(\alpha_1 - \alpha_0)$ and $\log I$ will give a straight line with slope equal to 1.

Similarly, in the case of 3PA,

$$\frac{dI}{dz} = \alpha_0 I - \gamma I^3 \quad 5.20$$

In this case we can write the transmission in terms of a new α_2 which is equivalent to

$$\alpha_2 = \alpha_0 + \gamma I_2 \quad 5.21$$

Here also α_2 can be calculated from the transmission values ($\alpha_2 = -(\log T)/L$).

And since $\alpha_2 = \alpha_0 + \gamma I_2$, $\alpha_2 - \alpha_0 = \gamma I_2$. Taking logarithm on both sides,

$$\ln(\alpha_2 - \alpha_0) = \ln \gamma + 2 \ln I \quad 5.22$$

where $\log \gamma$ is a constant, and hence this is the equation of a straight line ($y=mx+c$). Hence a plot between $\log(\alpha_2 - \alpha_0)$ and $\log I$, will give a straight line with slope =2. If we have a case where both 2PA and 3PA are present, we will get a line with slope value in between 1 and 2. So a plot between $\log(\alpha_x - \alpha_0)$ and $\log I$ has been taken and then fit a straight line this plot. The value of the slope will tell the process that's happening in the sample.

5.5.2 z-scan studies other magnetic nanostructures

The z-scan studies were extended to other magnetic nanostructures such as Ni NWs (FESEM: figure 3.4), Ni @ Co nanorods (FESEM: 3.36), Co NW filled MWCNT (FESEM: figure 4.12), and Ni filled MWCNTs (FESEM: figure 4.5). All the samples were prepared as discussed in the above case of Co NWs. Initially the alumina template is removed using alkaline treatment and then the nanowires are dispersed in the mixture solution of toluene and ethanol in the ratio 2:1. Figure 5.11 depicts the z-scan curve obtained for Ni NWs. Ni NWs found to exhibit a strong optical limiting property. The blue bubbles indicate the experimental data. The red star indicates the best fit for 3PA and magenta Square indicates the best fit for 2PA.

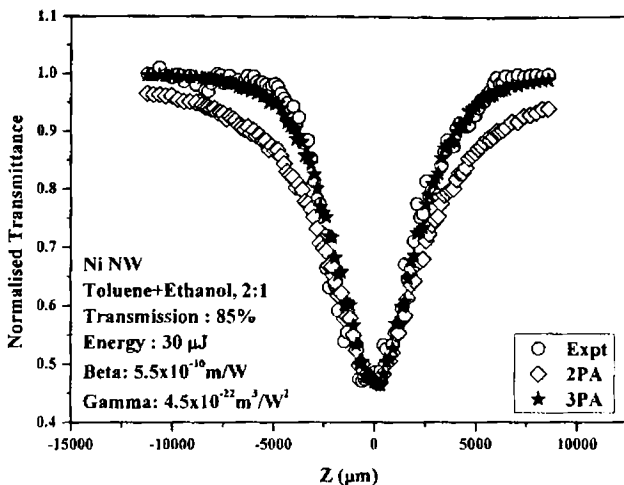


Figure 5.11: z-scan curve for Ni NWs.

It is evident from the theoretical fitting that the experimental data fits well with 3PA. It is a typical metallic character as discussed in the case of Co NTs. The 3PA coefficient (β_2 or Gamma) calculated is found to have a value of $4.5 \times 10^{-22} \text{ m}^3/\text{W}^2$.

Z-scan studies on Ni @ Co core-shell are conducted and they are also found to exhibit strong optical limiting properties. Optical limiting properties shown by these hybrid nanostructures are depicted in figure 5.12.

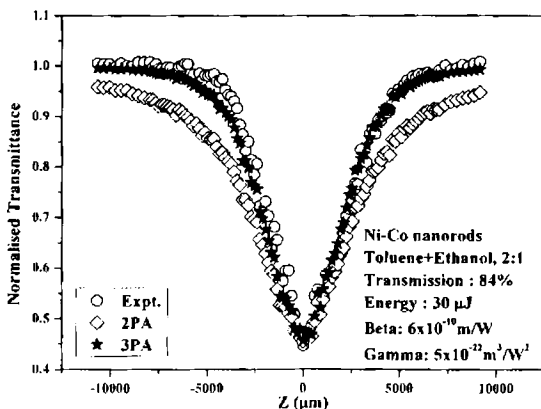


Figure 5.12: z-scan curve for Ni @ Co nanorods.

Similar to Ni NWs and Co NTs, Ni @ Co nanorods also exhibited 3PA behaviour (the experimental data (blue circles) is best fitted to simulated 3PA curve (red stars)). The calculated value of 3PA coefficient is $5 \times 10^{-22} \text{ m}^3/\text{W}^2$.

Z-scan studies conducted on Ni filled MWCNTs and Co NW filled MWCNTs are depicted in Figure 5.13. Both of them were found to be exhibiting a strong optical limiting behaviour.

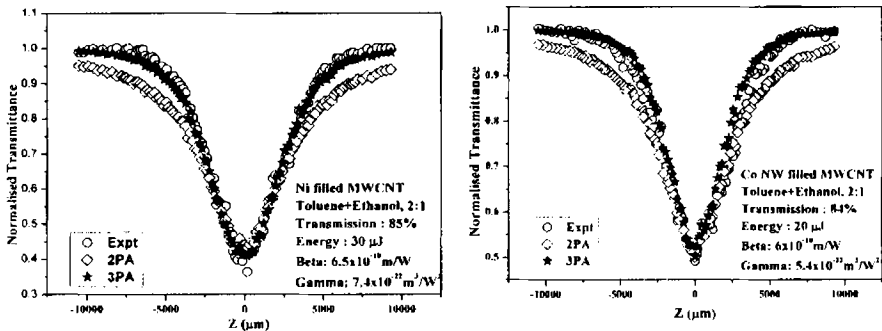


Figure 5.13: z-scan curve for (a) Ni filled MWCNTs, (b) Co NW filled MWCNTs.

But, unlike cobalt-in-carbon nanotubes, Ni filled MWCNTs and Co NW filled MWCNTs exhibited 3PA behaviour instead of an inbetween one. This may be due to the higher optical limiting contribution of metals compared to MWCNTs in to the cumulative optical nonlinearity of the composite material. Ni filled MWCNTs have a 3PA coefficient value, β_2 (Gamma) of $7.4 \times 10^{-22} \text{ m}^3/\text{W}^2$ and Co NW filled MWCNTs have a β_2 value of $5.4 \times 10^{-22} \text{ m}^3/\text{W}^2$ indicating that they can act as good optical limiters.

Conclusion

Optical limiting properties of various magnetic nanostructures are studied using z-scan measurement. In comparison to the benchmark multiwall carbon nanotubes, cobalt and cobalt-in-carbon nanotubes are found to show a higher nonlinear absorption. To our knowledge this is the first study where the optical limiting properties of a metal nanotube are compared to those of carbon nanotubes. The cobalt-in-carbon nanotubes exhibit an interesting transmission behavior, where an effective two-photon and effective three-photon absorption nonlinearities are present simultaneously. z-scan studies conducted on Ni NWs, Ni @ Co nanorods also revealed that they can act as efficient optical limiters. Ni filled MWCNTs and Co NW filled MWCNTs also exhibited strong optical limiting properties. The nonlinear parameters numerically calculated from these measurements show that these materials are efficient optical limiters. In addition to potential applications in safety devices for sensitive optical detectors and human eyes, this type of multifunctional materials can find use in various other fields also, such as high power super capacitor electrodes, sensors, and catalysis.

References

1. Wang, J.; Blau, W. J. *J. Opt. A: Pure Appl. Opt.* (2009) 11 024001.
2. Franken, P. A.; Hill, A. E.; Peters, C. W.; Weinreich, G. *Phys. Rev. Lett.* (1961) 7 118.
3. Griffith, D. J. *Introduction to Electrodynamics* (2000) Prentice-Hall of India pvt. (3rd edition).
4. Sutherland, R. L. *Hand book of nonlinear optics* (2003) 2nd Eddition, Marcel Dekker, Inc. New York, USA.
5. Boyd, R. W. *Nonlinear Optics* (1992) Academic Press, New York.
6. Rath, H.; Sankar, J.; Prabhu Raja, V.; Chandrashekar, T. K.; Nag, A.; Goswami, D. *J Am Chem Soc.* (2006) 127 11608.
7. Albota, M.; Beljonne, D.; Brédas, J.; Ehrlich, J. E.; Fu, J.; Heikal, A. A.; Hess, S. E.; Kogej, T.; Levin, M. I. D.; Marder, S. R.; McCord-Maughon, D.; Perry, J. W.; Röckel, H.; Rumi, M.; Subramaniam, G.; Webb, W. W.; Wu, X.; Xu, C. *Science* (1998) 281 1653.
8. Perry, J. W.; Mansour, K.; Lee, I. Y. S.; Wu, X. L.; Bedworth, P. V.; Chen, C. T.; Ng, D.; Marder, S. R.; Miles, P.; Wada, T.; Tian, M.; Sasabe, H. *Science* (1996) 273 1533.
9. Vincent, D.; Petit, S.; Chin, S. L. *Appl. Opt.* (2002) 41 2944.
10. Philip, R.; Kumar, G. R.; Sandhyarani, N.; Pradeep, T. *Phys.Rev.B.* (2000) 62 13160.
11. Kumar, G. R.; Rajgara, F. A.; Rangwala, S. A. *Chem. Phys. Lett.* (1995) 245 287.
12. Riggs, J. E.; Walker, D. B.; Carroll, D. L.; Sun, Y. J. *Phys. Chem. B.* (2000) 104 7071.
13. Sun, X.; Yu, R. Q.; Xu, G. Q.; Hor, T. S. A.; Ji, W. *Appl. Phys. Lett.* (1998) 73 3632.
14. Ebbesen, T. W.; *Carbon Nanotubes: Preperation and Properties* (1997) CRC Press: Boca Raton, Fla.
15. Maeng, I.; Kang, C.; Oh, S. J.; Son, J.; An, K. H.; Lee, Y. H. *Appl. Phys. Lett.* (2007) 90 051914.
16. Chen, P.; Wu, X.; Sun, X.; Lin, J.; Ji, W.; Tan, K. L. *Phys.Rev.Lett.* (1999) 82 2548.
17. Maeda, A.; Matsumoto, S.; Kishida, H.; Takenobu, T.; Iwasa, Y.; Shiraishi, M.; Ata, M.; Okamoto, H. *Phys.Rev.Lett.* (2005) 94 047404.

18. ÓFlaherty, S. M.; Murphy, R.; Hold, S. V.; Cadek, M.; Coleman, J. N.; Blau, W. J. *J. Phys. Chem. B.* (2003) 107 958.
19. Vivien, L.; Anglaret, E.; Riehl, D.; Bacou, F.; Journet, C.; Goze, C.; Andrieux, M.; Brunet, M.; Lafonta, F.; Bernier, P.; Hache, F. *Chem. Phys. Lett.* (1999) 307 317.
20. O'Flaherty, S. M.; Hold, S. V.; Brennan, M. E.; Cadek, M.; Drury, A.; Coleman, J. N.; Blau, W. J. *JOSA B* (2003) 20 49.
21. Liu, X.; Si, J.; Chang, B.; Xu, G.; Yang, Q.; Pan, Z.; Xie, S.; Ye, P. *Appl. Phys. Lett.* (1999) 74 164.
22. Ebbesen, T. W.; Ajayan, P. M. *Nature* (1992) 358 220.
23. Pan, H.; Chen, W.; Feng, Y. P.; Ji, W.; Lin, J. *Appl. Phys. Lett.* (2006) 88 223106.
24. Wang, Q. Q.; Han, J. B.; Gong, H. M.; Chen, D. J.; Zhao, X. J.; Feng, J. Y.; Ren, J. J. *Adv. Funct. Mater.* (2006) 16 2405.
25. Sheik-Bahae, M.; Said, A. A.; Wei, T. H.; Hagan, D. J.; Van Stryland, E. W. *IEEE J. Quantum Electron.* (1990) 26 760.
26. Couris, S.; Koudoumas, E.; Ruth, A. A.; Leach, S. J. *Phys. B* (1995) 28 4537.
27. Gu, B.; Wang, J.; Chen, J.; Fan, Y.; Ding, J.; Wang, H. *Optics Express* (2005) 13 9230.
28. Sun, X.; Xiong, Y.; Chen, P.; Lin, J.; Ji, W.; Lim, J. H.; Yang, S. S.; Hagan, D. J.; Van Stryland, E. W. *Applied Optics* (2000) 39 1998.

Chapter 6

Synthesis and Characterisation of Magnetic Iron Oxide Nanostructures

Nano magnetic oxides are promising candidates for high density magnetic storage and bio-medical applications. This chapter discusses the synthesis and studies on spherical and non-spherical (acicular) Iron Oxide ($\gamma\text{Fe}_2\text{O}_3$) nanoparticles using complexing media such as starch. Non-spherical mesoscopic iron oxides are also candidate materials for studying the shape, size, and strain induced modifications of various physical properties viz. optical, magnetic, and structural. Magnetic and optical properties of spherical as well as non-spherical iron oxide nanoparticles are subjected to detailed investigations. The role of a complexing medium like starch in aiding the directional growth of $\gamma\text{Fe}_2\text{O}_3$ is studied. Thermo-gravimetric and Fourier Transform Infrared spectroscopic studies are conducted to identify the impurity phases present.

**A part of the work discussed in this chapter has been published in "Bull. Mater. Sci." (2008, 31, 5, 759).*

6.1 Introduction

Mesoscopic magnetic iron oxides have attracted the attention of scientists for a variety of reasons. Magnetic iron oxides are candidate materials for audio, video and compact memories.^[1] Recently efforts are underway to find new applications of these materials - as drug delivery agents, as superparamagnetic iron oxide (SPION) particles for hyperthermia, contrast enhancing agents in magnetic resonance imaging (MRI)^[2] and also as biosensors.^[3] They are biocompatible and inexpensive. From a fundamental point of view, magnetic iron oxides are ideal templates for studying ferrimagnetism at the nano level since they possess an ideal two sub lattice with magnetic ions on either sites.

Magnetic iron oxides belong to the class of inverse spinels having their cation distributed on the octahedral sites (B) and tetrahedral sites (A). Maghemite or gamma ferric oxide also crystallizes in the inverse spinel structure. The structure of maghemite is said to possess a vacancy ordered spinel structure with vacancies situated exclusively on the octahedral sites.^[4] The preparation of gamma iron oxide from precursors is tricky because the material turns easily in to its nonmagnetic phase during synthesis if adequate precautions are not taken.

Nonsphericity is an essential criterion for enhancing signal to noise ratio during recording.^[5-6] But γFe_2O_3 is a cubic crystal and does not easily crystallizes in to elongated ellipsoidal particles. Earlier, workers have attempted to synthesize nonspherical precursors using complexing medium.^[7] Nucleation will be greatly influenced by external conditions, like pH, temperature and constant stirring. Complexing agents like starch retard the growth of the precursors in the crystallographic a-directions, so that growth proceeds in the c-directions, leading to needles.^[8] However, with the advent of nanoscience and nanotechnology, shape and size induced

modifications of various properties like optical, magnetic, structural properties is a rich area of physics where quantum mechanical phenomenon like quantum size effects can be investigated on candidate materials like gamma iron oxide.^[9] It is also known that size dependent magnetic properties manifest itself in to superparamagnetism and single domain characteristics. Reduction of size results in large red shift in Fe_3O_4 nanoparticles.^[10]

Most of earlier studies on nonspherical particles are limited to the synthesis of nonspherical γFe_2O_3 particles. Most of the particles lie well above the nanometer dimension.^[7] However, size, shape and strain dependent optical and magnetic properties are a virgin area where the effect of size and shape can be studied in a single shot if nanosize particles can be synthesized. Such a study assumes importance because of the resulting magneto optical properties of the nanocrystals.

In this chapter spherical and elongated mesoscopic gamma iron oxide particles are synthesized employing a novel technique and using starch/water/ethylene glycol as Complexing agents. Their structural, magnetic, optical properties are evaluated. Emphasis is laid in studying the shape induced optical properties of gamma iron oxide nanoparticles. Thermo Gravimetric (TG) and FTIR analysis are carried out to probe the retention of organic residues in the sample. Attempts are made to correlate the optical, magnetic properties with size and shape.

6.2. Experimental

6.2.1 Preparation of spherical γFe_2O_3 nanoparticles

In order to prepare spherical γFe_2O_3 particles, 20% of starch solution is prepared by adding 20 g of soluble starch in to 100cc of hot water. The resultant solution is heated with constant magnetic stirring to $50^{\circ}C$ till it became transparent. 25g of anhydrous ferrous sulphate is dissolved in 75 cc

starch solution. This solution was heated to 70°C. To this solution 0.2 molar ethylene glycol is added. It is presumed that ethylene glycol inhibits the growth of the particles along one particular direction. Addition of ethylene glycol must be drop wise with constant stirring in order to ensure the formation of spherical particles. These particles are filtered off and dried in a furnace at 370°C dried in ambient atmosphere to ensure the formation of $\gamma\text{Fe}_2\text{O}_3$.^[11] This leads to a brown magnetic powder confirming the formation of $\gamma\text{Fe}_2\text{O}_3$ nanoparticles.^[12] These samples are hereafter named N-1.

6.2.2 Preparation of ellipsoidal $\gamma\text{Fe}_2\text{O}_3$

The above procedure for the synthesis of spherical iron oxide particles is modified to prepare ellipsoidal gamma iron oxide (here after named N-2) in the sense, that instead of ethylene glycol and starch, water and starch are the employed as the complexing for this medium. 25g of anhydrous ferrous sulphate was dissolved in 75 cc starch solution. This solution was heated to 70°C. To this solution 0.2 molar solution of oxalic acid is added to precipitate nonspherical ferrous oxalate precursors from the medium. It is found that as the concentration of starch increases aspect ratio also increases.

6.2.3 Characterization

The structural analysis and the identification of the phase are conducted using an X-ray diffractometer (Rigaku Dmax-C) using Cu K α radiation ($\lambda = 1.5418 \text{ \AA}$). A scanning rate of 5° min⁻¹ is applied in the 2 θ range of 10° - 70°. The grain size is estimated by employing Debye-Scherrer's formula

$$D = 0.9\lambda / \beta \cos\theta \quad 6.1$$

where λ is the wavelength of X ray used, β is the FWHM of the XRD peak with maximum intensity and θ is the angle of diffraction. A JOEL JEM 2200 FS electron microscope using an accelerating voltage of 200 kV is used to deduce the particle size distribution of nanoparticles. The Transmission Electron Microscope (TEM) images, High Resolution Transmission Electron Microscope (HRTEM) images and Energy Dispersed Spectra (EDS) are recorded for morphological and compositional studies. Room temperature magnetic properties are obtained from the hysteresis loop recorded in a Vibrating Sample Magnetometer (VSM) model EG&G Par 4500. A Thermo Nicolet Avatar 370 DTGS model spectrophotometer using the KBr method was used to record the FTIR spectrum of the samples. A Jasco V 530 UV – Visible spectrophotometer was used to determine the diffused reflectance studies. DTG studies are conducted using Perkin Elmer Thermal Analysis in the Nitrogen atmosphere in the temperature range 30 – 550 °C.

6.3 Results and Discussion

6.3.1 Structural and Morphological Studies using XRD and TEM

The x ray powder diffraction pattern of the spherical (N-1) and the nonspherical (N-2) Iron Oxide nanoparticles are depicted in Figure 6.1. and they represent a spectrum typical of an inverse spinel. The planes are identified and listed. The peaks (111), (220), (311), (400), (511) and (440) correspond to that of $\gamma\text{Fe}_2\text{O}_3$ (ICDD: 39-1346).

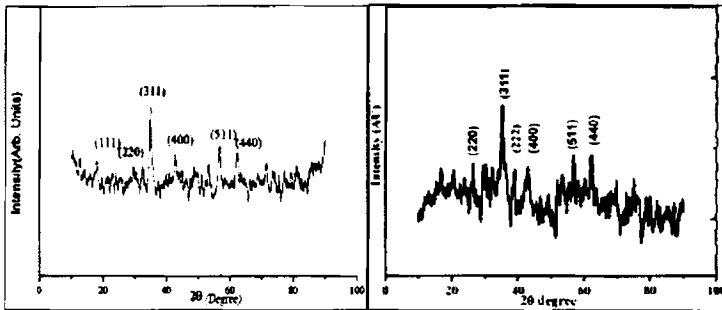


Figure 6.1: XRD patterns of $\gamma\text{Fe}_2\text{O}_3$, N-1 (left), (b) N-2(right).

There are no indications for the existence of any impurity phase, corresponding to $\alpha\text{Fe}_2\text{O}_3$. However, the base line is found to be shifted due to the presence of amorphous phase probably due to the organic inclusion of the samples. The average particle size was determined from line broadening and the spherical particles have an average size of 10 nm. TEM images of N-2 indicate that the formations of nonspherical particles (Figure 6.3), while particles coded N-1 are spherical in shape (Figure 6.2). The spherical particles have an average size of 10 nm. Nonspherical particles have an average length of 19 nm and breadth 9 nm with an average aspect ratio of 2.

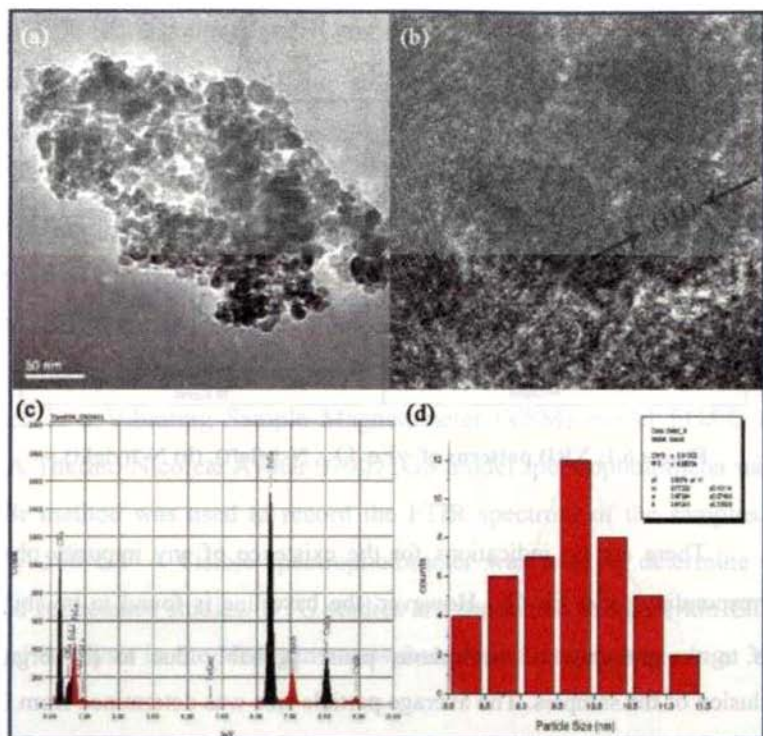


Figure 6.2: (a) TEM image, (b) HRTEM, (c) EDS, (d) size distribution histogram of N-1.

It is evident from Figure 6.2.b that the particles are highly crystalline and well separated by grain boundaries. Diffusion of lattice planes in to the grain boundary is also noted. The EDS indicates the presence of Iron from Iron Oxide nanoparticles. The particle size distribution for spherical particles is determined for spherical particles and a histogram depicting the size distribution is shown in Figure 6.2.d.

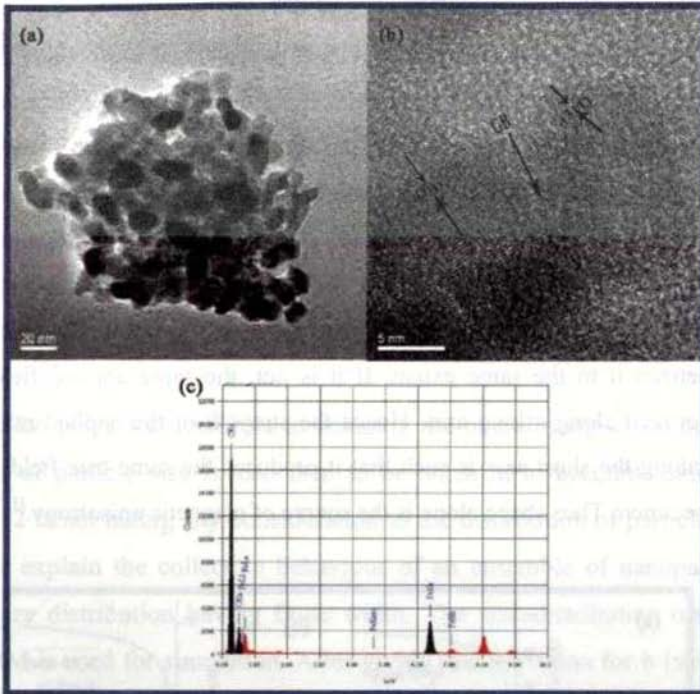


Figure 6.3: (a) TEM image, (b) HRTEM image, (c) EDS of N-2.

Figure 6.3 depicts the TEM, HRTEM, and EDS images of non-spherical iron oxide particles. The discrepancy in particle size as determined by XRD and TEM could be because of the fact that only large crystallites contribute to the Bragg peak.^[13] It can be seen from Figure 6.3.b that although the crystal lattice of particles are well defined, the Miller indices are interlocked (buckled) and lattices planes have a small bending in the grain boundary. These are evidence for the occurrence of high internal strain with in the lattice.^[14]

6.3.2 Magnetization studies using VSM

The hysteresis loop for spherical (N-1) and nonspherical iron oxide particles (N-2) are shown in figure 6.4. Nonspherical particles exhibit a saturation magnetization of 30 emu/g while spherical particles display a saturation magnetization of 37 emu/g and a coercivity of 105 Oe. Enhancement of coercivity for sample N-2 and decrease in its saturation magnetization with respect to N-1 are other evidences for the deviation from sphericity of sample N-2. If the particles are spherical, the same applied field would have magnetized it to the same extent. If it is not, the same applied field will magnetize it along a long axis. Hence the strength of the applied magnetic field along the short axis is such that it produces the same true field inside the specimen. Thus shape alone is the source of magnetic anisotropy.^[15]

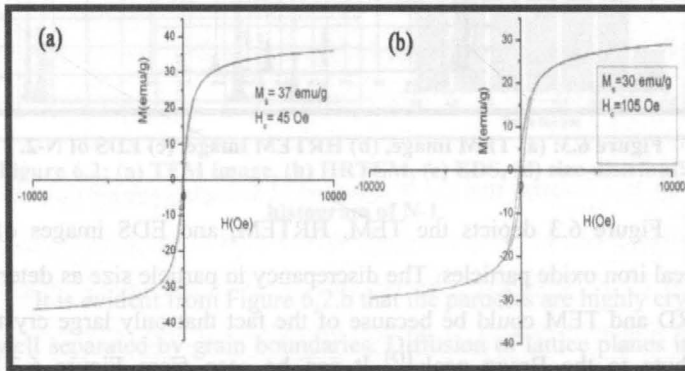


Figure 6.4: Room temperature $M(H)$ curves for (a)N-1, (b)N-2.

Thus it can be inferred from the magnetization curves of N-1 and N-2 that increase in coercivity in the case of N-2 is mainly due to the elongation of grains. These ellipsoidal particles may cause a small amount of spin freezing in random directions. This is one of the reasons attributed to the decrease in saturation magnetization value for N-2. The magnetization

curve of N-1 shows almost negligible remanence and small coercivity showing their superparamagnetic nature.

Additional evidence for superparamagnetism exhibited by N-1 can be obtained by simulating the magnetization curve using the Langevin function $L(x)$. Here it is assumed that the individual grains are single crystals with the number of crystals equal to the number of domains. We have Langevin function represented by

$$L(x) = \coth x - \frac{1}{x} \quad 6.2$$

Size plays a crucial role in deciding the overall magnetization. The variation of particle size is also then to be taken in to account. Since the equation 2 is not taking any consideration to the distribution of particle size, it cannot explain the collective behaviour of an ensemble of nanoparticles with a size distribution having finite width. The size distribution obtained from TEM is used for simulation. After giving due provision for b (width of the size distribution histogram) the Langevin function can be modified as,^[16]

$$L(x) = \frac{1}{2bx} \int_{x(1-b)}^{x(1+b)} L(x') dx' \quad 6.3$$

$$= \frac{1}{2bx} \ln \left\{ \frac{(1-b) \sinh[x(1+b)]}{(1+b) \sinh[x(1-b)]} \right\} \quad 6.4$$

The simulated Langevin function using Eq.(4) is carried out and is shown in Figure 6.

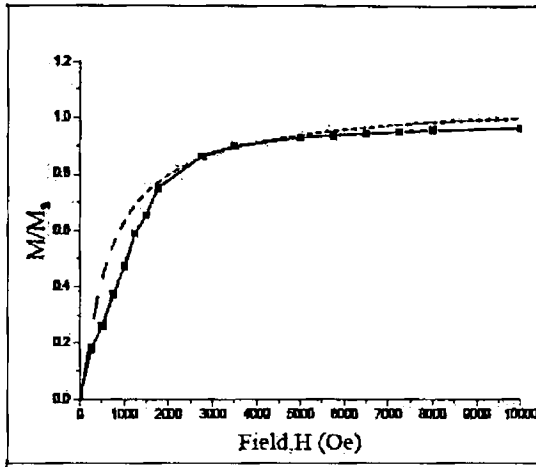


Figure 6.5: Modified Langevin function fit for N-1.

The fitting (Figure 6.5) is carried out after giving due weightage for particle size distribution. Thus simulated curve (linear) fits very well (particularly at average sizes) with experimental curve (dotted).

6.3.3 TG-DTG Studies

Bulk maghemite in the micron regime possess a saturation magnetization of ~ 74 emu/g ^[15] and coercivity of 250 Oe, ^[11] and they are generally multidomain in character. However, as particle size reduces they became single domain and exhibit superparamagnetic characteristics. Although we have procured evidence for superparamagnetism by Langevin fitting, the reduction in magnetization is to be probed by supplementary techniques. For this TG DTG studies are carried. The TG-DTG curves are shown in Figure 6.6.

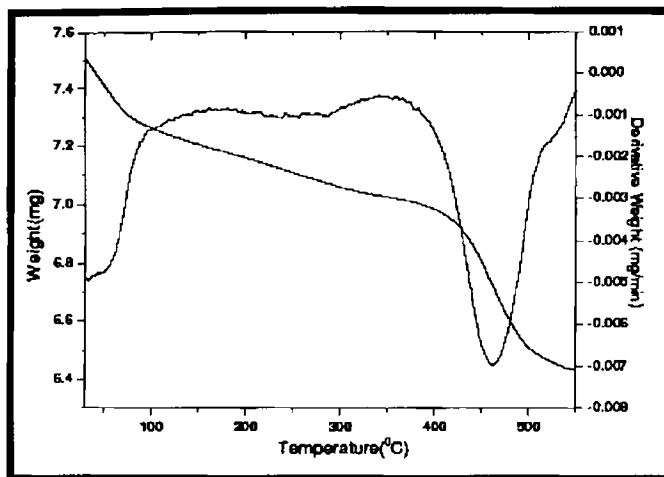


Figure 6.6: TG-DTG curve for N-1.

TG curve shows a continuous weight loss on heating. A substantial weight loss corresponding to 8% at 450 °C is observed. The net weight loss is around 14% when the temperature reaches 550 °C. There is a possibility of a small fraction of the polymer (particularly starch which can remain there till 1000 °C) being retained in the sample which normally does not decompose at these temperatures. If due weightage is provided to the retention of polymeric residues, in the final gamma ferric oxide the observed saturation magnetization can be accounted for.

6.3.4 FT- IR Studies

FT-IR studies are carried out on N-1 and N-2 samples in order to ascertain the presence of starch. The spectrum is charted in Figure 6.7.

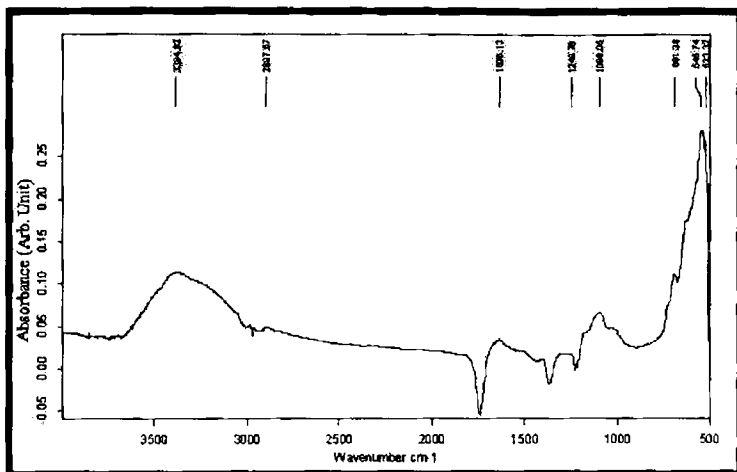


Figure 6.7: FT-IR spectrum of N-1.

The peak at 3384.82 corresponds to -OH group and the broadening shows the presence of hydrogen bonding. This strengthens the evidence for the presence of starch in the samples.^[17] This -OH group with hydrogen bonding is coming from starch. Peaks between 500 and 700 cm^{-1} correspond to Fe-O bonds.^[18]

6.3.5 Energy band gap calculation

Band gap calculation plays an important role in characterising the materials at nano level. In the case of nanoparticles, various factors like lattice strain, plasmonic confinements, surface and shape effects and quantum confinement effects can alter and engineer the band gap and hence, the determination of band gap plays a seminal role in nanoparticle characterisation. Diffused Reflectance Spectroscopic (DRS) studies of samples N-1 and N-2 are conducted using UV-Visible NIR Spectrophotometer. Energy band calculations are carried out using the relation,^[19]

$$\alpha = \sum \alpha_i = \sum \frac{A_i (h\nu - E_{gi})^{m_i}}{h\nu} \quad 6.5$$

where the value of E_{gi} and m_i correspond to the energy and the nature of the particular optical transition with absorption coefficient α_i . For allowed direct, allowed indirect, forbidden direct and forbidden indirect transitions, the value of m_i corresponds to $1/2$, 2 , $3/2$ and 3 , respectively.^[20] Since the particles are nanocrystalline, the values of E_{gi} and m_i are determined without presuming the nature of electronic transition.^[21] Eq.5. can be rewritten in the following form

$$\frac{d(\ln(\alpha h\nu))}{d(h\nu)} = \frac{m}{(h\nu - E)} \quad 6.6$$

The plot of $\frac{d(\ln(\alpha h\nu))}{d(h\nu)}$ versus $h\nu$ will produce discontinuity at a particular value of $h\nu = E$ where a possible electronic transition can occur corresponding to the bandgap $E = E_{gi}$. Figure 6.8 (a) and (b) show the above plots for samples N-1 and N-2 respectively.

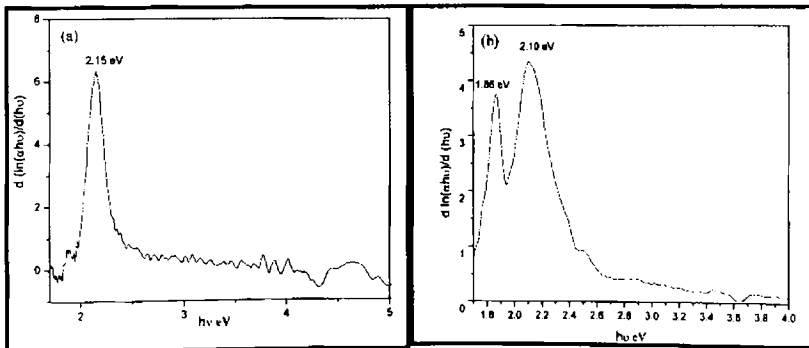


Figure 6.8: Bandgap calculation from differential plot; (a) for N-1, (b) for N-2.

The red shifted electronic band (~ 0.24 eV) is due to the presence of ellipsoidal particles which are under very high stress. This is further supported by HRTEM (Figure 3.b.). This shows that, although the crystal lattice of particles is well defined, the Miller indices are buckled (Figure 3.b.). The nature of electronic transition is found using $\ln(\alpha_1 h\nu - E)$ vs $\ln(\alpha_1 h\nu)$ curves (figure 6.9) and it is found that the slope of the curves is ~ 0.5 . This indicates that the electronic transition involved is 'allowed direct'.

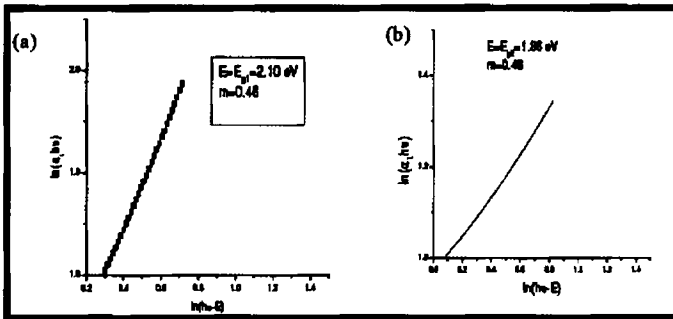


Figure 6.9: $\ln(h\nu - E)$ vs $\ln(\alpha_1 h\nu)$ curves for; (a) N-1, (b) N-2.

From the lattice constants for spherical and nonspherical $\gamma\text{Fe}_2\text{O}_3$ particles unit cell compression of $(\Delta V/V) \sim 10\%$ was observed in the case of nonspherical particles. Stress increases as the size is reduced. The reduction in bandgap is governed by the narrowing of the direct bandgap due to the enhanced pressure from the surface tension, where pressure $P = 2\gamma/r$, γ is the surface tension and r is the size of the grain. So the strain induced modification of band gap provides a phenomenological explanation for the anomalous red shift observed in mesoscopic iron oxide particles. The effect of matrix or any other impurities in the red shift has been removed, since the entire measured band gaps are well above the red shifted value.

Conclusion

The employment of a complexing medium like starch for the synthesis of nonspherical iron oxide particles can be modified to tailor the aspect ratio of nonspherical nanoparticles of gamma ferric oxide, since shape controlled particles are of interest both from a fundamental and application point of view. The observed reduction in saturation magnetization with respect to the saturation magnetization of bulk maghemite is due to the presence of superparamagnetism and residual organic impurities in the final product.

Strain induced modification of band gap is possible by carefully controlling the acicularity of these particles. Shape control can also induce anisotropy and thus modify the coercivity of these particles. A simple phenomenological explanation was provided to explain the red shift found in the optical band gap of nonspherical maghemite particles.

References

1. Taeghwan, H. *Chem. Commun.* (2003) 927.
2. Sabino, V.-verdager; Maria, del P.; Morales; Oscar, Bomati-M.; Carmen, B.; Xinquing, Z.; Pierre, B.; Rigoberto, Perez de A.; Jesus, Ruiz-cabello; Martin, S.; Fransisco, J. Tendillo-Cortijo; Joaquin, F. *J. Phys. D: Appl. Phys.* (2004) 37 2054.
3. Panagiotis, D.; Nicolas, M.; Eamonn, D.; Dimitrios, N.; Dimitros, P. *Nanotechnology* (2006) 17 5019.
4. Viswanathan, B. *Ferrite materials: Science and Technology* (1990) Narosa Publishing House, New Delhi.
5. Deng, M. C.; Hsu, S. L.; Chin, T. S. *IEEE Trans. Magn.* (1992) 28 2385.
6. Bate, G. J. *Magn. Mater.* (1991) 100 413.
7. Anantharaman, M. R.; Joseph, K. V.; Keer, H. V. *Bull. Mater. Sci.* (1997) 20 7 975.
8. Arndt, V.; BASH, A. G.; Ludwigshafer. *Magnetics, IEEE Transactions* (1998) 24 2 1796.
9. Kachkachi, H.; Ezzir, A.; Nogues, M.; Tronc, E. *Eur. Phys. J. B* (2000) 14 681.
10. Swapna, S. Nair; Mercy Mathews; Anantharaman, M. R. *Chem. Phys. Lett.* (2005) 406 398.
11. Venkatesh Rao; Shashimohan, A. L.; Biswas, A. B. *Journal of Material Science* (1974) 9 430.
12. Abbas, A.; Khaleel. *Chem. Eur. J.* (2004) 10 925.
13. Cohen, J. B. *Ultramicroscopy* (1990) 34 41.
14. John, K.; Vassiliou; Vivek Mehrotra.; Michal. W. Russell; McMichael, R. D.; Shull, R. D.; Ronald F. Ziolo. *J. Appl. Phys.* (1993) 73 10.
15. Cullity, B. D. *Introduction to magnetic materials* (1972) Addison-Wesley Publishing company Philippines.
16. Chikazumi. *Physics of Magnetism* (1964) John Wiley & Sons, New York, USA.
17. Robert, M. Silverstein; Francis, X. Webster; *Spectroscopic identification of organic compounds* (1964) John Wiley & Sons, New York, USA.
18. Raksha Sharma; Subhalakshmi Lamba; Annapoorni, S. *J. Phys. D: Appl. Phys.* (2005) 38 3354.

19. Pankov, J. J. *Optical Processes in Semiconductors* (1971) Printice-Hall, New Jersey, USA.
20. Bhattacharyya, D.; Chaudhuri, S.; Pal, A. K. *Vacuum* (1992) 43 313.
21. Chakrabarti, S.; Ganguli, D.; Chaudhuri, S. *Physica E* (2004) 24 333.

Chapter 7

Conclusion

Major highlights of the present investigation are summarized in this chapter, outlining the potential utility of magnetic nanowires/nanotubes and hybrid magnetic nanostructures with MWCNTs. Several advantages of template-assisted approach over other available routes along with some of their limitations are also dealt with in this chapter. Moreover, the prospective applications of such high aspect ratio magnetic nanostructures formed in the absence of chemical modifications of porous nano structure or surface passivation agents in various fields are also reviewed. The method of synthesis of multifunctional magnetic nanostructures has been extended to the fabrication of a multiferroic material using template assisted deposition. The initial results of this work are also briefly discussed in this chapter.

Investigating magnetic properties of matter on the nanoscale is a very active area in modern solid state physics. Exciting phenomena, like inter layer exchange coupling or the giant magneto resistance occurs in low dimensional systems where characteristic length scales such as magnetic exchange lengths, become relevant. Nanomagnetism is of utmost importance to current technological developments. The dramatic increase in magnetic storage density over the last decade, various applications of miniaturized magnetic sensor devices based on the giant magneto resistance effect, and the development of spintronics, a new generation of computing technology, require a thorough understanding of magnetism at the nano meter scale.

Spintronics considers spin of an electron as additional degrees of freedom, which can be manipulated to obtain particular functionalities. Recent concepts for Spintronic logical elements discuss domain walls, which are intermediate region of spin inhomogeneity between two domains with opposite magnetization directions, in nano wired elements. Other magnetic nano scale systems that exhibit the large scale activities, both in fundamental and applied research are multilayers, oxides, nanoparticles, nanostructures, magnetic semiconductors, magneto caloric materials (MCE materials) and multiferroic materials. Several key questions in these systems depend on the dynamics of magnetization and the associated magnetic structures.

The fabrication and characterisation of 1-D magnetic nanostructures of uniform size and shape have importance in the current scenario of advanced research to design multifunctional nanostructures and various nanoelectronic devices. Nanowires and nanotubes of Ni and Co having high aspect ratio, high crystallinity and texturing were fabricated. They also exhibited high magnetic response and interesting temperature dependent magnetic properties. A very high magnetic dipolar interaction was identified among these magnetic nanowires and nanotubes and it can suitably tuned by

Conclusion

controlling the separation between them and it is very important in device fabrication and magnetic data storage. A very high coercivity Co NTs were fabricated for the first time using cobalt acetate as precursor. The elucidation of a general growth mechanism during template assisted potentiostatic electrodeposition was another milestone of the present thesis.

A mobility assisted growth mechanism was proposed for the growth of 1-D nanostructures during potentiostatic electrodeposition inside porous templates and its veracity has been tested using various porous templates and precursors. This growth mechanism has been utilised to design a novel multisegmented bi-metallic magnetic nanostructure, called Ni @ Co nanorods and this again opens the possibility designing other hybrid structures using template assisted electrodeposition. Moreover, tuning of magnetic properties can be successfully attained using these types of hybrid magnetic materials and it is an added advantage over other nanofabrication techniques, where the tunability is not as handy as it here.

Alumina templates are beneficial for shape controlled synthesis of not only high aspect nanostructures but also other non-spherical shapes without the assistance of any capping molecules/surfactants or any other foreign species. In perpendicular geometry of nanowires and nanotubes, GMR can be significantly larger than when current is in the film plane. Heterogeneous alloy films, which are of interest for their GMR, which is a promising property of high density storage media, have also been successfully prepared by electrodeposition. Extremely high aspect ratio (ratio of length to diameter), will make the demagnetizing field highly anisotropic; which is one of the desirable criteria for the achievement of perpendicular recording. Various magnetic alloys and heterostructures can be tested for their GMR and MCE performance and is reserved as a future prospective.

Hybrid magnetic materials with carbon nanotubes represent a novel class of smart materials where they can find immense technological and fundamental interest. Metal filling inside CNTs and the subsequent dragging of the metals is one of the active and cutting edge research area where we can fabricate more interesting carbon structures such as graphene. MWCNTs filled various magnetic nanostructures were synthesized and they also exhibited interesting magnetic properties. Ni and Co were electrodeposited inside MWCNTs using various precursors and interesting structures are obtained under different precursors. The mobility assisted growth mechanism has been successfully verified in the case of MWCNTs too.

An interesting co-axial nanostructure of MWCNTs with Co nanotubes has been fabricated using cobalt acetate as precursor for electrodeposition. This co-axial structure also found to exhibit very high longitudinal coercivity indicating the structure perfection and shape anisotropy of the nanostructure. Interesting applications of these nanostructures are also attempted to probe. Ni filled MWCNTs found to exhibit an enhanced microwave absorption capability when compared to Ni NWs and MWCNTs. This can be due to the increased metal-MWCNT interfaces and nanosized particle size of the Ni particles. MWCNTs were almost completely impregnated with aqueous ferrofluids of Iron Oxide using the principle of nanocapillarity.

The successful, complete filling of MWCNTs with magnetic materials like ferrofluid is being reported for the first time. The resulting nanostructure also found to exhibit interesting magnetic properties. Confined existence of superparamagnetic Iron Oxide nanoparticles inside MWCNTs leads to an anomalous enhancement in magnetisation with temperature. Origin of this anomalous magnetic property is supposed to be due to the increased magnetic interactions due to the confined existence and warrant

Conclusion

detailed investigations. The MWCNT-Superparamagnetic Iron Oxide system is identified as an excellent system for various bio-medical applications such as augmented drug delivery, cell separation, contrast enhancement agents in MRI, drug targeting and hyperthermia. Studies on the drug attachment and delivery, and therapeutical applications are highly promising and are proposed as future perspective.

Non-linear optics is another mature field of science and engineering and the synergy of non-linear optics with magnetism is thought to be a novel idea for the fabrication of various multifunctional nanostructures. The fabricated nanowires and nanotubes of Ni, Co and Ni @ Co nanorods and their hybrid structures with MWCNTs found to exhibit interesting non-linear optical properties. All these 1-D nanostructures were found to act as excellent non-linear optical limiters. Particularly, cobalt-in-carbon nanotube found to exhibit non-linear transmission behaviour where they exhibited inbetween behaviour of effective 3PA and effective 2PA. Moreover, optical limiting properties of MWCNTs were compared with that of metal nanotubes for the first time and such a comparison is more appropriate as both kind of system induce similar kind of geometrical distortion when an electromagnetic radiation falls on them.

The emulsions/dispersions of these one-dimensional structures can be made using various organic solutions and can be coated over sensitive optical devices and goggles to protect them from high intense lasers. Tunable non-linear optical limiter is one of the novel ideas in non-linear optics and not cherished yet. This kind of magnetic nanostructures in proper dispersion may fruitful this concept and much studies are needed on this topic. This also extends as a future prospective.

The importance of magnetic iron oxide is persists as high for a long time due to their extensive applications in particulate media and

biocompatibility. The concept of acicular iron oxide was emerged with their applications in storage media to reduce the signal to noise ratio. Acicular iron oxide nanoparticles were synthesized using starch as a complexing medium. Their magnetic and optical properties were compared with those of synthesized spherical nanoparticles. Interesting optical properties were identified and a strain induced band gap shift is observed in the case of acicular particles. The tuning of the aspect ratio can be achieved by controlling the processing parameters like concentration, pH, temperature, stirring speed etc and it opens a wide scope for future work. The acicularity dependent magnetic properties are highly intriguing and can find potential uses in various fields such as in particulate media. Role of complexing media such as starch/glycerol in controlling and tuning the aspect ratio is need to be subjected in to detailed investigation in order to synthesis complex nanostructures of magnetic as well as non-magnetic materials.

The expertise gained in the fabrication of magnetic nanostructures can be extended for the designing and the synthesis of other useful nanosystems. Multiferrocity is one of the emerging trend in material science research, where the same system exhibit ferromagnetic ordering as well as ferroelectric properties. Hybrid materials represent a novel class of materials where desirable properties of the individual systems are expected to dominate giving a multifunctional system. An attempt towards the realisation of hybrid materials based multiferroics is not taken anywhere and such a step will surely impact the future research and technology to a great extend. An initial step has been taken towards the realisation of a multiferroic material based on ferromagnetic nanotubes and ferroelectric nanotubes. The FESEM pictures of this hybrid structure are depicted in figure 7.1.

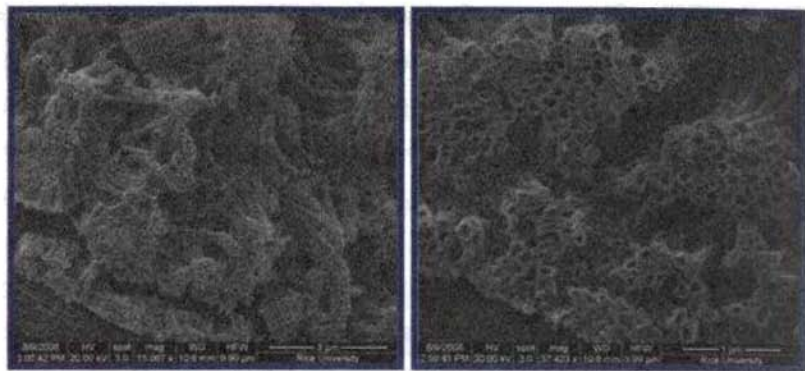


Figure 7.1: FESEM images of a hybrid nanotube system of ferromagnetic and ferroelectric materials.

Studies on these hybrid nano structures are in the initial stages and have a very high scope in the fundamental understanding of physics of multiferroic materials and increasing application demands due to their application potential.

Though template assisted synthesis is an ingenious technique comparing to other fabrication techniques, this technique also faces some drawbacks which need to be pointed out. Since the template is usually a thin membrane, it is difficult to scale-up the nanostructure and grow through this route to macroscopic quantities, although efforts in that direction are underway. Another lacuna of this technique is that the nanostructures synthesized through this template are often polycrystalline. Despite these shortcomings, template assisted electrodeposition is identified as a versatile technique and it will be worthwhile to employ this technique to fabricate other nanostructures resembling Ni @ Co and Co-in-MWCNTs nanostructures.

Research is an eternal journey to unravel the mysteries of nature and every researcher contributes his might to the vast comity of

research. This contribution, though infinitesimally small, fits the old adage “Tiny drops of water makes a mighty ocean”. This investigation must also be viewed from such a backdrop and this study and the subsequent contribution to the vast knowledge base will only form a nanocomponent in the mega canvass of Science.

However, this must be seen as yet another attempt to investigate the truth and the search for absolute truth goes on and on. It is often said that what remains constant in the universe is ‘change’. Physicists are always looking for these ‘changes’ which would help modify their understanding of the nature and mould new concepts.

Finally, as the eastern philosophy goes, even if you have infinity as denominator the net ‘result’ is nothingness but it is ancient India which gave a definite value to this ‘nothingness’. So nothingness is also something and very significant.

Publications

Peer Reviewed Journals

1. Evidence for intergranular tunneling in polyaniline passivated α -Fe nanoparticles; Vijutha Sunny, **T N Narayanan**, U S Sajeev, P A Joy, D Sakthi Kumar, Yasuhiko Yoshida and M R Anantharaman: **Nanotechnology**, 17(2006) 4765-4772.
2. Strain induced anomalous red shift in the band gap of mesoscopic nonspherical superparamagnetic iron oxide prepared by a novel technique; **T N Narayanan**, D Sakthi Kumar, Yasuhiko Yoshida and M R Anantharaman. **Bull. Mater. Sci.**, 31 (2008), 759-766.
3. Synthesis of high coercivity cobalt nanotubes and elucidation of their mechanism of growth; **T N Narayanan**, M M Shaijumon, P M Ajayan and M R Anantharaman. **J. Phys. Chem. C.**, 112(2008), 14281-14285.*
4. On the synthesis of nickel and cobalt nanowires and comparison of their magnetic properties; **T N Narayanan**, M M Shaijumon, Lijie Ci, P M Ajayan and M R Anantharaman, **Nano Research**, (2008) 1(6): 465-473.
5. On the synthesis and magnetic properties of multiwall carbon nanotube-superparamagnetic iron oxide nanoparticle Nanocomposites; **T N Narayanan**, A P Reena Mary, M M Shaijumon, Lijie Ci, P M Ajayan and M R Anantharaman, **Nanotechnology**, 20 (2009) 055607(7pp).
6. Enhanced microwave absorption in nickel filled multiwall carbon nanotubes in the S band, **T N Narayanan**, Vijutha Sunny, M M Shaijumon, P M Ajayan, and M R Anantharaman, **Electrochem. Solid State Lett.**, (2009), 12, 4, K21- K24.**
7. The Synthesis of High Coercivity Cobalt-in-Carbon Nanotube Heterostructures and Their Optical Limiting Properties, **T N Narayanan**, C S Suchand Sandeep, M M Shaijumon, P M Ajayan, Reji Philip and M R Anantharaman, **Nanotechnology** (2009), 20, 285702.***
8. Fabrication of a quantum well heterostructure based on plasma polymerised aniline and its characterization using STM/STS, **T N Narayanan**, Soumya Jose, Senoy Thomas, Salim H Al-Harti, and M R Anantharaman, **J. Phys. D: Appl. Phys.** (2009), 42 165309 (7pp).
9. Synthesis of high coercivity core-shell nanorods based on nickel and cobalt and their magnetic properties, **T N Narayanan**, M M Shaijumon, P M Ajayan and M R Anantharaman, **Nanoscale Res. Lett.** (2009) 1 0.1007/s11671-009-9459-7.

10. Template assisted synthesis and characterization of passivated nickel nanoparticles, E Veena Gopalan, K A Malini, G Santhoshkumar, **T N Narayanan**, P A Joy, D Sakthikumar, Yasuhiko Yoshida, I A Al-Omani, and M R Anantharaman, **Nanotechnology** (Submitted).
11. Non-interacting superparamagnetic iron oxide and silica based core-shell ferrofluids for biomedical applications, **T N Narayanan**, P K Anas Swalih, A P Reena Mary, D Sakthi Kumar, Denys Makarov, Manfred Albrecht and M R Anantharaman. **Nanotechnology** (submitted).
12. On the magnetic and magneto-optical properties of aqueous ferrofluids of noninteracting SPIONs for magnetic hyperthermia, A P Reena Mary, **T N Narayanan**, Vijutha Sunny, D Sakthi Kumar and M R Anantharaman. **J. Magn. Magn. Mater.** (Submitted).
13. Optical power limiting in Ni and Co nanowires and comparison of their optical limiting properties with carbon nanotubes, **T N Narayanan**, C S Suchand Sandeep, M M Shaijumon, P M Ajayan, Reji Philip and M R Anantharaman. **J. Appl. Phys.** (Manuscript under preparation).

* Also cited by Nano Highlights from ACS Publications (20080826) (zz).

** Also cited by Virtual Journal of Nanoscience and Technology, (2009)19, 4.

**** Also Cited by Nanotechweb.iop.org.

Conference Proceedings

1. Optical Power Limiting In Cobalt Nanotubes and Carbon Nanotubes, **T N Narayanan** , Suchand Sandeep C S, Shaijumon M M, Ajayan P M, Reji Philip and M R Anantharaman; 7th International conference on Materials Processing for Properties and Performance (MP³), Singapore, 5-7 November 2008. (*Oral Presentation*)
2. MWCNT-SPION Nanocomposites using aqueous ferrofluid by nanocapillarity, **T N Narayanan**, A P Reena Mary, M M Shaijumon, Lijie Ci, P M Ajayan and M R Anantharaman, in International Conference on Magnetic Materials & their Applications for 21st Century (MMA 21) held at National Physical Laboratory (NPL), New Delhi, India, 21st -23rd October, 2008. (*Oral Presentation*)
3. Evidence for the occurrence of inter granular tunneling in passivated ultrafine Fe particles with polyaniline. Vijutha Sunny, **T.N Narayanan**, U.S.Sajeev, P.A Joy, M.R.Anantharaman, International Seminar on Optoelectronic materials and thin films (OMTAT), 2005, Kochi, Kerala.
4. A Novel Technique for the Synthesize of Shape Controlled $\gamma\text{Fe}_2\text{O}_3$ nanoparticles, **T N Narayanan**, D Sakthi Kumar, Yasuhiko Yoshida, and M R Anantharaman, Indian National Science Academy & Hungarian Academy of Sciences sponsored Workshop on Condensed Matter Research: *Magnetic Materials*. 4 December 2006, School of Physics, University of Hyderabad.
5. Shape induced effects on the Optical and magnetic properties of $\gamma\text{-Fe}_2\text{O}_3$ Nanoparticles. **T N Narayanan**, Vijutha Sunny and M R Anantharaman. International Conference on Nanomaterial and its Applications, NIT Trichy, February 05-06, 2007.
6. Model Dielectric Function Analysis for band gap calculations on Bulk ZnO particles & Spin coated ZnO films, **T. N. Narayanan**, A. P. Reena Mary and M. R. Anantharaman, in the National Conference on Current Trends in Materials Science (CTMS 07) conducted by Chengannur Christian College, 26th March 2007. (*Oral Presentation*)
7. Smart Magneto Rheological Materials based on Iron and Natural Rubber, M P Vasudevan namboothiri, **T N Narayanan**, Vijutha Sunny, M R Anantharaman. National Conference on New Horizons in Theoretical and

Experimental Physics, Department of Physics, Cochin University of Science & Technology, Kochi, Kerala, India. October 8-10, 2007.

8. On the preparation and properties of CNT-SPION nanocomposites, **T N Narayanan**, A P Reena Mary, M M Shaijumon, P M Ajayan, and M R Anantharaman, 6th International Symposium on Bioscience & Nanotechnology, 6 November 2008, Toyo University, Japan.
9. General mobility assisted growth mechanism for the formation of one dimensional nanostructures during electrodeposition, **T N Narayanan**, M M Shaijumon, P M Ajayan, and M R Anantharaman, Second International Conference on Frontiers in Nanoscience and Technology, Cochin Nano-2009, January 3-6, 2009.